



NAVAL POSTGRADUATE SCHOOL

MONTEREY, CALIFORNIA

DISSERTATION

**TERAHERTZ FREE ELECTRON LASER: DESIGN,
SIMULATION AND ANALYSIS**

by

Conor M. Pogue

December 2014

Dissertation Supervisor

William B. Colson

Approved for public release; distribution is unlimited

THIS PAGE INTENTIONALLY LEFT BLANK

REPORT DOCUMENTATION PAGE			Form Approved OMB No. 0704-0188	
Public reporting burden for this collection of information is estimated to average 1 hour per response, including the time for reviewing instruction, searching existing data sources, gathering and maintaining the data needed, and completing and reviewing the collection of information. Send comments regarding this burden estimate or any other aspect of this collection of information, including suggestions for reducing this burden, to Washington headquarters Services, Directorate for Information Operations and Reports, 1215 Jefferson Davis Highway, Suite 1204, Arlington, VA 22202-4302, and to the Office of Management and Budget, Paperwork Reduction Project (0704-0188) Washington DC 20503.				
1. AGENCY USE ONLY (Leave blank)		2. REPORT DATE December 2014	3. REPORT TYPE AND DATES COVERED Dissertation	
4. TITLE AND SUBTITLE TERAHERTZ FREE ELECTRON LASER: DESIGN, SIMULATION AND ANALYSIS			5. FUNDING NUMBERS	
6. AUTHOR(S) Conor M. Pogue				
7. PERFORMING ORGANIZATION NAME(S) AND ADDRESS(ES) Naval Postgraduate School Monterey, CA 93943-5000			8. PERFORMING ORGANIZATION REPORT NUMBER	
9. SPONSORING /MONITORING AGENCY NAME(S) AND ADDRESS(ES) N/A			10. SPONSORING/MONITORING AGENCY REPORT NUMBER	
11. SUPPLEMENTARY NOTES The views expressed in this dissertation are those of the author and do not reflect the official policy or position of the Department of Defense or the U.S. Government. IRB protocol number ____N/A____.				
12a. DISTRIBUTION / AVAILABILITY STATEMENT Approved for public release; distribution is unlimited			12b. DISTRIBUTION CODE A	
13. ABSTRACT (maximum 200 words) Terahertz (THz) radiation is a portion of the electromagnetic spectrum with many potential uses but without a wide availability of powerful sources. The free electron laser (FEL) has been demonstrated to produce intense, coherent THz radiation. This dissertation explores a novel THz FEL oscillator design that is tunable within a wavelength range of ~60 micrometers to ~130 micrometers and could produce up to ~2 kW average output power. It utilizes superconducting spoke cavities for the accelerating structures to generate an 8 MeV electron beam with ~8.75mA average current. The variable gap undulator has only ten periods; this design choice enhances the extraction and therefore output power, but also reduces single pass gain. To overcome the reduced gain, the optical cavity is designed to minimize round trip losses. This design is relatively compact and could be installed on a ship to test technologies that are relevant for future scaling to weapons class output powers.				
14. SUBJECT TERMS Terahertz, THz, free electron laser, FEL, oscillator, high power, kW			15. NUMBER OF PAGES 125	
			16. PRICE CODE	
17. SECURITY CLASSIFICATION OF REPORT Unclassified	18. SECURITY CLASSIFICATION OF THIS PAGE Unclassified	19. SECURITY CLASSIFICATION OF ABSTRACT Unclassified	20. LIMITATION OF ABSTRACT UU	

NSN 7540-01-280-5500

Standard Form 298 (Rev. 2-89)
Prescribed by ANSI Std. Z39-18

THIS PAGE INTENTIONALLY LEFT BLANK

Approved for public release; distribution is unlimited

**TERAHERTZ FREE ELECTRON LASER: DESIGN, SIMULATION AND
ANALYSIS**

Conor M. Pogue
Civilian, Niowave, Inc.
B.S., University of California Santa Barbara, 2010
M.S., Naval Postgraduate School, 2012
M.S., Naval Postgraduate School, 2013

Submitted in partial fulfillment of the
requirements for the degree of

DOCTOR OF PHILOSOPHY IN APPLIED PHYSICS

from the

**NAVAL POSTGRADUATE SCHOOL
December 2014**

Author: Conor M. Pogue

Approved by: William B. Colson
Professor of Physics
Dissertation Supervisor

Keith Cohn
Professor of Physics

Joseph Blau
Professor of Physics

Gamani Karunasiri
Professor of Physics

James Newman
Professor of Space Systems

Approved by: Andrés Larraza, Chair, Department of Physics

Approved by: Douglas Moses, Vice Provost for Academic Affairs

THIS PAGE INTENTIONALLY LEFT BLANK

ABSTRACT

Terahertz (THz) radiation is a portion of the electromagnetic spectrum with many potential uses but without a wide availability of powerful sources. The free electron laser (FEL) has been demonstrated to produce intense, coherent THz radiation. This dissertation explores a novel THz FEL oscillator design that is tunable within a wavelength range of ~ 60 micrometers to ~ 130 micrometers and could produce up to ~ 2 kW average output power. It utilizes superconducting spoke cavities for the accelerating structures to generate an 8 MeV electron beam with ~ 8.75 mA average current. The variable gap undulator has only 10 periods; this design choice enhances the extraction and therefore output power, but also reduces single pass gain. To overcome the reduced gain, the optical cavity is designed to minimize round trip losses. This design is relatively compact and could be installed on a ship to test technologies that are relevant for future scaling to weapons class output powers.

THIS PAGE INTENTIONALLY LEFT BLANK

TABLE OF CONTENTS

I.	INTRODUCTION.....	1
A.	MOTIVATION	1
B.	USES FOR THZ RADIATION	1
1.	Academic / Scientific Applications	1
a.	THz Spectroscopy.....	1
b.	Pump-probe Experiments	2
2.	Homeland Defense Applications.....	2
C.	TERAHERTZ SOURCES.....	4
1.	Advantage of THz FELs.....	5
D.	TERAHERTZ FEL DESCRIPTION	5
E.	NIOWAVE, INC.	6
F.	FEL ON A TEST SHIP	6
II.	BASIC FEL THEORY	9
A.	FREE ELECTRON LASER COMPONENTS	9
1.	Injector.....	9
a.	Cathode.....	9
b.	Accelerating Cavity	10
2.	Linear Accelerator	11
3.	Undulator.....	13
4.	Electron Beam Control.....	13
5.	Optical Cavity.....	14
B.	FEL THEORY	14
1.	Electron Equations of Motion.....	15
2.	Electron Motion in the Undulator Field	15
3.	Resonance Condition	16
4.	FEL Pendulum Equation	17
5.	Optical Field Evolution.....	22
a.	Spontaneous Emission.....	22
b.	Weak Field Gain	22
c.	Coherence Development	24
d.	Wave Equation	25
e.	Short Pulse Effects.....	27
f.	Electron Beam Quality.....	29
III.	FEL SIMULATIONS	33
A.	NOMINAL FEL PARAMETERS	33
B.	CODE DESCRIPTIONS.....	34
1.	GINGER	35
2.	4DPULSEN.....	35
3.	1D FEL Code.....	35
C.	GAIN SPECTRUM.....	36
D.	WEAK FIELD GAIN VS. ENERGY SPREAD	40

E.	VARYING UNDULATOR GAP HEIGHT	43
F.	ELECTRON BEAM RADIUS.....	45
G.	OPTICAL MODE SHAPE.....	48
H.	AVERAGE OUTPUT POWER.....	50
I.	OPTICAL CAVITY ALIGNMENT TOLERANCES.....	50
IV.	ELECTRON BEAM PHYSICS.....	55
A.	ELECTRON BEAM QUALITY	55
1.	Transverse Emittance.....	55
2.	Energy Spread.....	57
3.	Desired Electron Beam Quality	58
B.	FOCUSING: QUADRUPOLE MAGNETS	58
C.	BENDING: DIPOLE MAGNET DESIGN.....	60
1.	Dipole Design.....	61
2.	Simple Dipole Physics	61
3.	Fringe Fields.....	63
4.	Energy Spread.....	63
D.	COMBINED FUNCTION MAGNETS	64
1.	Tilted End Faces.....	65
2.	Canted Pole Faces	65
E.	NIOWAVE BEAMLINE GEOMETRY	66
F.	BEAMLINE MODELING: GENERAL PARTICLE TRACER	67
1.	Code Description.....	67
2.	Optimization with Only Quadrupoles.....	68
3.	Combining Quadrupoles and Rectangular Dipole Magnets.....	70
4.	Quadrupoles and Combination Magnets.....	72
a.	<i>GINGER Results</i>	75
V.	HARDWARE DESIGN	79
A.	LINAC COMPONENTS.....	79
B.	TRANSPORT BEAMLINE COMPONENTS	80
1.	Beam Pipes.....	80
2.	Quadrupoles	81
3.	Dipoles.....	81
C.	OPTICAL CAVITY BEAMLINE.....	82
1.	Transverse Cavity Dimensions	82
a.	<i>Mirror Size</i>	83
b.	<i>Beam Pipe Sizes</i>	84
2.	Mirror Mount Assemblies.....	84
a.	<i>Mirror Mount Housing Chamber</i>	84
b.	<i>Mirrors</i>	86
c.	<i>Mirror Mount Assembly</i>	86
d.	<i>Output Window</i>	88
e.	<i>Miscellaneous</i>	90
D.	EXIT BEAMLINE	91
E.	ALIGNMENT TECHNIQUES.....	92
1.	Transverse and Angular Mirror Alignment.....	92

2.	Longitudinal Alignment	94
F.	FINAL DESIGN IN 3D	94
VI.	CONCLUSION	97
	LIST OF REFERENCES	99
	INITIAL DISTRIBUTION LIST	105

THIS PAGE INTENTIONALLY LEFT BLANK

LIST OF FIGURES

Figure 1.	Atmospheric absorption bands created using LEEDR atmospheric absorption code.	3
Figure 2.	Schematic of an FEL oscillator, from [23].	9
Figure 3.	Cross section of five cell superconducting elliptical cavity accelerator, from [25].	12
Figure 4.	Schematic of single spoke cavity, from [26].	12
Figure 5.	Permanent magnetic undulator schematic with electron beam, from [29].	13
Figure 6.	Pendulum phase space plot.	19
Figure 7.	The phase space procession of the electrons during the FEL interaction about $\nu_o=0$	20
Figure 8.	The phase space procession of the electrons during the FEL interaction about $\nu_o=6$	21
Figure 9.	Weak field gain as a function of ν_o	24
Figure 10.	Coherence development over 2500 passes, from [31].	25
Figure 11.	Depiction of optical lethargy of the light pulse transiting the undulator.	28
Figure 12.	Comparison of energy spread of initial electron bunches, strong fields.	30
Figure 13.	Comparison of energy spread of initial electron bunches, weak fields.	31
Figure 14.	1D simulation results (blue) and analytic solution (red) of gain spectrum of Niowave THz FEL for 0% energy spread.	37
Figure 15.	Gain spectrum (blue) with energy spread overlay (red).	38
Figure 16.	Gain spectrum of Niowave THz FEL: $\Delta\gamma/\gamma=1.66\%$	39
Figure 17.	Scan of weak field gain vs. wavelength using <i>GINGER</i> FEL code for the Niowave FEL parameters.	40
Figure 18.	Gain degradation from energy spread using 1D code.	41
Figure 19.	<i>GINGER</i> (red) and <i>4DPULSEN</i> (blue) code results of gain against initial electron energy spread for the Niowave THz FEL.	42
Figure 20.	<i>4DPULSEN</i> results showing gain vs. dimensionless desynchronism (d) for an energy spread of 0% (blue), 1.2% (red), and 2.4% (black).	43
Figure 21.	Diffraction of the optical mode compared with undulator gap width.	44
Figure 22.	<i>GINGER</i> simulations of electron beam (blue) and optical mode (red) transverse profiles for 2 mm, 1 mm, and 0.55 mm initial electron beam radius. The horizontal axis is the distance z along the undulator, the vertical axis is the transverse rms dimension.	46
Figure 23.	<i>GINGER</i> gain as a function of pass number for 2 mm initial electron beam radius.	47
Figure 24.	<i>GINGER</i> gain as a function of pass number for 1 mm initial electron beam radius.	47
Figure 25.	<i>GINGER</i> simulation results for transverse electric field at undulator exit for increasing hole radii.	49
Figure 26.	<i>4DPULSEN</i> simulation results for weak field gain as a function of shift of one of the cavity mirrors.	51

Figure 27.	<i>4DPULSEN</i> simulations of weak field gain as a function of tilt of one of the cavity mirrors.	52
Figure 28.	The desynchronism curves for different mirror shifts (on left) and mirror tilts (on right).	53
Figure 29.	Typical phase space diagram of electron bunch where x is the particles transverse position x' is the particles momentum in that direction, from [36].	55
Figure 30.	Electron beam phase space evolution as it passes through a beam waist, from [36].	56
Figure 31.	Depiction of magnetic field of quadrupole magnet, after [38].	59
Figure 32.	Quadrupole triplet for transverse beam focusing, from [23].	60
Figure 33.	Cross-sectional view of dipole magnets, from [41].	61
Figure 34.	Depiction of electrons motion through a uniform magnetic field, after [42]. ..	62
Figure 35.	Electron beam dispersion from a dipole magnet due to energy spread.	64
Figure 36.	Dipole magnet with rotated pole faces.	65
Figure 37.	End view of canted dipole, from [43].	66
Figure 38.	Side and top profile view of Niowave beamline.	67
Figure 39.	Electron beam radius (rms) through beamline.	69
Figure 40.	Electron beam trajectory in x (top) and y (bottom) plane.	71
Figure 41.	Transverse electron beam size along beam path.	72
Figure 42.	Geometry of combination magnet, from [44].	73
Figure 43.	Electron beam trajectories in x (top) and y (bottom) plane using combination magnets.	74
Figure 44.	Trajectories of electrons from middle of undulator through last dipole.	75
Figure 45.	Electron beam (red) and optical mode (blue) transverse profiles for <i>GINGER</i> simulations using the electron beam parameters from GPT.	76
Figure 46.	Ginger simulations for gain for the Niowave THz FEL using electron beam properties from GPT.	77
Figure 47.	CAD drawing of linac for Niowave THz FEL.	79
Figure 48.	Niowave THz FEL transfer beamline highlighted in red.	80
Figure 49.	Diagram of necessary custom beam pipe with 14 degree bends.	81
Figure 50.	Optical cavity beamline highlighted in blue.	82
Figure 51.	Mirror mount housing chamber, from [49].	85
Figure 52.	Measured transmittance spectrum for crystal quartz window, from [51].	88
Figure 53.	Final design for mirror housing and control assembly.	89
Figure 54.	Example of conflat flange mounted electrical feed through (left) and necessary connection (right), from [52] and [53].	90
Figure 55.	The exit beamline highlighted in green	92
Figure 56.	Schematic of optical cavity alignment system for Niowave THz FEL	93
Figure 57.	Final design of optical cavity beam vacuum structures	95

LIST OF TABLES

Table 1.	Current THz FELs, from [14]–[20].	5
Table 2.	Electron beam parameters being simulated.	33
Table 3.	Undulator parameters being simulated.	33
Table 4.	Optical cavity parameters being simulated.	34
Table 5.	GPT simulation parameters.	68
Table 6.	Optimized quadrupole parameters with the distances measured from the end of the linac.	69
Table 7.	GPT derived Twiss parameters of electron beam at undulator entrance.	76
Table 8.	Calculated round trip power loss due to clipping for each considered mirror size and wavelength.	83
Table 9.	Mirror housing chamber pricing information.	85
Table 10.	Gold mirror pricing information.	86
Table 11.	Mirror mount pricing information.	87
Table 12.	Translation stage pricing information.	87
Table 13.	Picomotor actuator pricing information.	87
Table 14.	Picomotor actuator controller pricing information.	88
Table 15.	Crystalline quartz window pricing information.	89
Table 16.	Electrical feedthrough pricing information.	90
Table 17.	Electrical feed-through connection pricing information.	91
Table 18.	Mechanical linear feedthrough pricing information.	91

THIS PAGE INTENTIONALLY LEFT BLANK

LIST OF ACRONYMS AND ABBREVIATIONS

C-4	composition 4 (explosive)
CW	continuous wave
DC	direct current
EM	electromagnetic
FEL	free electron laser
FTIR	Fourier transform infrared spectrometer
GHz	gigahertz
GPT	General Particle Tracer
HMX	high melting explosive
RDX	research department explosive
RF	radio frequency
SVEA	slowly varying envelope approximation
THz	terahertz
TNT	trinitrotoluene (explosive)
USN	United States Navy

THIS PAGE INTENTIONALLY LEFT BLANK

ACKNOWLEDGMENTS

I would like to take this time to thank everyone who has helped me with this accomplishment. This has truly been a large undertaking that would not have been completed without the tireless effort from everyone in the research group at NPS and all the support I've received from friends and family. My journey here has not been without its trials and tribulations, but the people around me have made it an enjoyable one.

The first person I'd like to thank is Professor Colson and the effort he had to put forth to battle all the hurdles that were thrown in my path here at NPS. It has been Professor Colson's constant encouragement that has helped me get here today. Not only has he guided me in my academic research, but also he's always been there to offer life advice along the way. While I've probably been one of the more stressful of his PhD students I am grateful for everything he has done.

Prof. Blau and Cohn have been extremely helpful to my research in their explanation of topics, their aid in getting different simulations to work, or just telling me where I'm going wrong in what I've written or are trying to present. I'm sure sometimes when they heard me knock on their doors they were less than excited, but they never hesitated to give a helping hand, and for that I am truly grateful.

Raquel, where can I start? She has always been there to see if I need anything, make sure I'm doing well, and lastly, supply chocolate. The time when she took my suit (that I forgot in the hotel room at a conference), had it dry cleaned, carried it back on an airplane, dropped it off thirty minutes from her home, all so I could wear it at graduation the next day, was truly a shining example of the type of person she is. I'll never forget all the help she's given me.

Without my work with Niowave I would not have been able to accomplish what I've done today. I give a special thanks to Dr. Grimm and Dr. Boulware for their support of this endeavor. Their desire to transform the equipment they make into a THz free electron laser gave me the support and the reason to solve the problem.

Last (but by no means the least), I'd like to thank my friends and family. Whether it's the coffee breaks in the basement with Sam, Kirk, and Preetha, or the phone calls back home to family, it's always kept me grounded. While I'm looking forward to moving on and getting an office with a window, I'll definitely miss the basement where I spent these five years.

I. INTRODUCTION

A. MOTIVATION

Free electron lasers (FELs) are continuously tunable sources of coherent electromagnetic (EM) radiation. They can be designed for a wide range of industrial, academic, medical, and military/homeland security applications. This dissertation will touch on the applications of terahertz (THz) radiation and be centered on the design of an FEL in the THz regime. THz radiation covers a frequency range from ~ 300 Gigahertz (GHz) to 10 THz (wavelengths of ~ 1 mm to $300 \mu\text{m}$). This particular frequency band covers what is known as the “THz gap” where there are few coherent sources and detectors as compared to other widely used frequency bands both above (microwave / radio waves) and below (infrared) [1]. This gap exists in part due to the scarcity of viable conventional gain media with energy transitions that correspond to THz frequencies. This dissertation will include discussions of the uses for THz radiation, comparisons between the different sources, simulations of the gain process for a THz FEL, and a plausible physical design for a THz FEL.

B. USES FOR THZ RADIATION

THz radiation has a wide range of applications for several professional communities.

1. Academic / Scientific Applications

Scientific applications include THz spectroscopy and pump-probe experiments.

a. THz Spectroscopy

Molecular spectroscopy can utilize THz radiation to study various materials due to the strong THz absorption lines corresponding to molecular vibrational and rotational modes [2]. The most common method for these measurements uses relatively weak incoherent black body sources and Fourier transform infrared spectrometers (FTIR) as part of the detectors. New methods may be developed using THz FEL to produce

powerful, coherent sources to study and categorize specific spectral line emissions from single vibrational or rotational modes.

b. Pump-probe Experiments

Pump-probe experiments can be utilized to measure ultra-fast phenomena in materials. The general principal is that a “pump” light pulse (usually a high peak power laser) is incident upon a sample and causes an excitation. A certain time later a “probe” pulse (generally lower in power) is incident upon the sample, and the reflection or the transmission signal is then be measured. A current area of research at several national labs is to use a THz pump source along with an x-ray probe source [3]. The timing between the two pulses is altered so that the transient behavior of the relaxation can be measured [4]. The National High Magnetic Field Laboratory is interested in a THz FEL to use in conjunction with high peak magnetic fields for research into new material properties. Broadband thermal sources commonly employed in THz spectroscopy are not suitable for pump-probe experiments; however, the THz pulses produced by an FEL could be utilized for these kinds of experiments.

2. Homeland Defense Applications

A useful property of THz radiation that lends itself to many uses in security and homeland defense applications is that it passes through many materials that are opaque to radiation in the optical regime. THz can readily penetrate most non-metallic and non-polar materials [5]. These include cloth (clothing, bags), building materials (paper, cardboard, wood), and a wide range of other barriers, which may be used to conceal a potential threat. Photons in the THz regime are of low enough energy to be non-ionizing, so that the EM radiation itself is a minimal health risk to the person being scanned or the operator of the device [6]. This type of technology is already utilized in current airport security scanners.

The THz radiation tends to be highly absorbed by water and O₂ causing propagation in the atmosphere to be fairly limited (see Figure 1). However, a more powerful THz source that could be tuned to a frequency of lower atmospheric absorption

could open up the door to longer-range applications of THz radiation. An example of atmospheric attenuation of THz radiation can be seen in Figure 1.

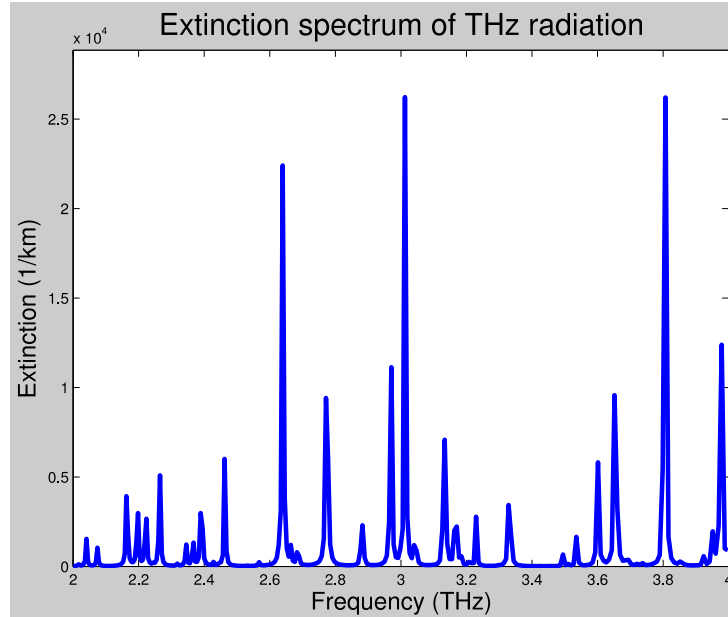


Figure 1. Atmospheric absorption bands created using LEEDR atmospheric absorption code.

For example, a ~ 1 kW THz source can transit several hundred meters and still maintain a high enough signal to be measured if tuned to a low absorption band. THz sources that are currently used tend to have many orders of magnitude less output power and are generally not tunable.

Another security application of THz radiation is to actually utilize its poor transmission properties in the atmosphere to make a secure communication system. The high attenuation of the THz radiation and the stronger directionality (over submillimeter or radio waves) could allow for a more secure connection between linked devices [7].

Furthermore, THz spectroscopy could be employed in the search for explosive or illegal substances. Many explosives (TNT, C-4, HMX, RDX, etc.) and illegal drugs (e.g., methamphetamines) have a characteristic absorption spectra in the THz region [8]. This characteristic coupled with the ability to penetrate many dielectric materials could aid in the search for concealed illegal substances.

C. TERAHERTZ SOURCES

Several different methods are used to create THz radiation of various power levels and frequencies; a few of them will be discussed in this section. One main source of THz radiation is the infrared-pumped gas laser, which produces between 1 mW – 20 mW of continuous wave (CW) power. This technology has been proven in the 500 GHz to 3 THz regime but the power spectrum depends on the gas being used as the gain medium [9].

Quantum cascade lasers are a relatively new source that is starting to become mature. These semiconductor devices can supply ~1 mW to 8 mW average power and can be pulsed at 10 kHz. They have the ability to be tuned from ~20 GHz to ~200 GHz [10].

Optical down-conversion is a method where a higher frequency signal (optical) is converted to the THz regime through certain interactions. One particular method uses two high intensity optical pulses focused onto a pair of electrodes with a gap $< \sim 1 \mu\text{m}$ printed on a semiconductor. This produces a photocurrent that is modulated at the frequency difference between the two incident laser pulses. This is tunable to produce a THz source with average power levels $\sim 0.1 \mu\text{W}$ to $1 \mu\text{W}$ [11]. Other systems use a non-linear crystal to mix frequencies of optical pulses to produce THz radiation, but often these have average power levels $\sim \text{nW}$ to μW [2].

Electron tube sources are available that generate THz radiation from the emission of bunched electrons that spiral in a strong magnetic field. These can take the shape of backward-wave electron tubes that have a wide frequency tuning range, and are fairly compact (table top), but supply only moderate (mW level) power [12]. There are larger microwave and THz sources in the form of gyrotrons that can be designed to provide higher power ($\sim 100 \text{ kW}$ to 1 MW) in either continuous wave or pulsed mode [13], though the pulses are of $\sim 1 \text{ ms}$ length and are not as desirable for pump-probe experiments. These are larger room size installations and often aren't scalable throughout the THz spectrum.

Along the lines of these sources are FELs, which also utilize beams of relativistic free electrons to generate the radiation, and can be scaled up to relatively high power (kW level) with shorter pulse lengths. A few of the current THz FELs are listed in Table 1.

FELs	Average Power	Peak Power	Wavelength Range
Novosibirsk (Russia)	~500 W	~0.5 MW	120 μ m – 230 μ m
Kaeri (Korea)	6 mW	~1 kW	100 μ m – 1200 μ m
FELIX (Netherlands)	~1 W	~100 MW	2 μ m – 250 μ m
ISIR (Japan)	~0.1 W	~0.5 MW	32 μ m – 144 μ m
FELBE (Germany)	~40 W	100 MW	18 μ m – 250 μ m
CLIO (France)	~1 W	~100 MW	3 μ m – 150 μ m

Table 1. Current THz FELs, from [14]–[20].

These FELs have high peak power and average power relative to other THz sources.

1. Advantage of THz FELs

THz FELs have many advantages compared to other THz sources. They can achieve relatively high average power (~1 kW–2 kW) compared to other THz sources, have narrow linewidths, are linearly polarized, have short pulse durations of several picoseconds, produce radiation in a fundamental transverse mode, and are tunable over a wide range of wavelengths. The short pulse length of the THz pulse along with the fundamental transverse mode shape allows for high peak brightness when the beam is focused. The short pulses and high repetition rates make FELs useful for pulse-probe experiments. For molecular spectroscopy, the ability to tune the frequency of the FEL would allow specific excitation of specific modes to be studied [21].

D. TERAHERTZ FEL DESCRIPTION

The THz FEL described in this dissertation is being developed by the U.S. Navy (USN) and Niowave, Inc. The designed spectral region is ~66 μ m–114 μ m. The FEL generates light by transferring energy from relativistic electron bunches to an optical pulse. It does this by transversely “wiggling” the electrons inside a periodic magnetic field, causing the electrons to radiate. The electron source, or injector, will supply electrons up to an energy of ~100 keV. Next, the electrons will be injected into a linear

accelerator (linac) structure that will bring the electron beam to the final design energy of 8 MeV. This relativistic electron beam will then be directed through an undulator (periodic rows of alternating permanent magnets) that generates the periodic transverse magnetic field that causes the electrons to radiate. The wavelength emitted depends on the electron beam energy, the strength of the magnetic field, and the period of the magnetic field. This FEL will be ~ 10 m– 15 m in length with a cross-sectional area of ~ 1 m²; it will operate as an oscillator, which has an optical cavity surrounding the undulator and beam line allowing the fields to build up inside the cavity over many passes.

E. NIOWAVE, INC.

Niowave, Inc., is a company in Lansing, MI, that specializes in creating superconducting electron accelerating structures and supporting technologies. These linacs accelerate electrons up to high energies (near the speed of light) so the electron's kinetic energy can be utilized in a wide a range of applications. These include the creation of medical radioisotopes; the production of light in free electron lasers, x-ray sources, and THz sources, and neutron production. Niowave also builds radio frequency (RF) guns, superconducting cavities and cryomodules, high-power RF couplers, and commercial 4K refrigerators. The Navy is particularly interested in the use of superconducting linacs to drive high average power FELs for shipboard defense [22]. The research done in this dissertation is for a proposed THz FEL built by Niowave for the USN.

F. FEL ON A TEST SHIP

This relatively small THz FEL is being designed for consideration to be put on a USN test ship, the USS *Paul F. Foster*. The USN is interested in a high average power FEL for tactical scenarios such as ship defense. The desired FEL would be ~ 1 MW output power at a wavelength with little atmospheric absorption in a maritime environment. The FEL being designed by Niowave and NPS has a much lower electron energy leading to a longer wavelength and an average power several orders of magnitude below the final design goal for ship based weapon. This project could, however, demonstrate, on a ship, many of the necessary technologies for a weapon class FEL. Things such as the liquid helium cryoplants, the cryomodules that surround the

accelerating structures, the optical cavities, and electron beamlines need to be vetted to show that the movement of the ship will not prevent the devices from working under various sea-state conditions. An FEL is sensitive to the alignment of its components, which includes the optical cavity, the electron beam and undulator axes, as well as the beam line components that guide the electron beam through the FEL. The THz FEL will use a relatively new shape for the electron beam accelerating structure, the spoke cavity design, that decreases the overall size while making it more rigid, which should be helpful in a shipboard environment. The low electron beam energy of the THz FEL decreases the amount of shielding that is required, making the whole system smaller and lighter in weight.

THIS PAGE INTENTIONALLY LEFT BLANK

II. BASIC FEL THEORY

A. FREE ELECTRON LASER COMPONENTS

An FEL oscillator is composed of four major components: an injector, which generates the electron bunches at a low beam energy; a linear accelerator, which accelerates the electron bunches up to the relativistic energies needed for the FEL interaction; an undulator, which causes the electrons to emit light; and an optical cavity, which stores the optical pulse to build up the power. A schematic of an FEL oscillator can be seen in Figure 2.

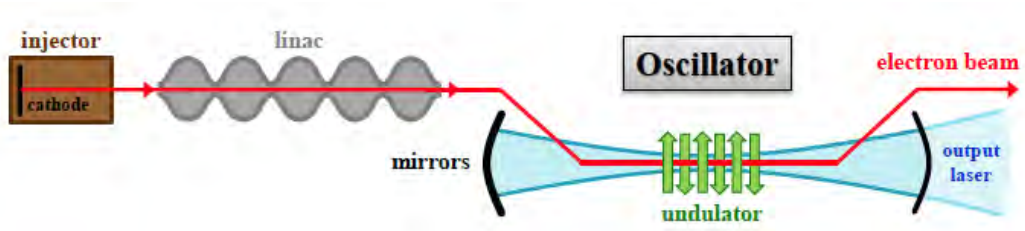


Figure 2. Schematic of an FEL oscillator, from [23].

1. Injector

The injector is made up of two key components: the cathode to generate the free electrons and a method to immediately accelerate the low energy electrons away from the cathode surface.

a. Cathode

An FEL requires an electron source (cathode) that will produce bunches of free electrons with proper beam characteristics needed for the FEL interaction. The main types of cathodes are photoelectric, field-emission, and thermionic. Which type is chosen depends on the electron beam parameters that are needed for the FEL interaction. For the proposed Niowave THz FEL, the thermionic cathode will be implemented.

A thermionic cathode uses the thermal energy imparted to an electron in a conduction band to give it enough energy to overcome the surface work function of the

material and become unbound and enter the vacuum. Thermionic cathodes have several benefits including long lifetimes and the ability to supply high current. A couple of disadvantages of thermionic cathodes are that they generally have lower beam quality and cannot be modulated as easily as other types [24].

b. Accelerating Cavity

Space charge, the inter-electron Coulomb repulsion, can cause the newly created beam to rapidly spread out in space as well as energy. If left unchecked, this can destroy the beam quality. However, as the electron beam approaches the speed of light ($\beta \approx 1$), space charge effects are significantly reduced due to relativistic effects. Thus, the newly generated electron beam should be quickly accelerated to relativistic energies to maintain good beam quality. This acceleration is done using either a radio frequency (RF) or direct current (DC) electric field at the cathode. This combination of cathode and accelerating cavity makes up the injector.

A DC injector uses a static potential between the cathode and an anode to accelerate the electron beam. A major problem with DC injectors is that the constant, high potential gradients can cause electrical breakdowns to occur. To mitigate this problem, an RF cavity is often utilized to achieve the high gradients needed. The RF cavity is a metal chamber of a certain shape that permits particular RF modes to exist inside of it by matching necessary boundary conditions. However, RF cavities come with their own limiting issues that must be addressed. Ohmic heating in the cavity walls caused by the oscillating electric current increases the amount of power that must be pumped into the system to accelerate the free electron bunch and could require that cooling be incorporated into the structure to remove this heat. Smaller cavities can lead to smaller / cheaper accelerators, but as the cavity size shrinks, the resonant frequency of the cavity increases. This increased frequency increases the power density on the walls causing more heating from ohmic losses. To counteract this, superconducting RF (SCRF) cavities have been developed to decrease the ohmic losses to nearly zero.

A superconducting material has a resistance that goes to zero for DC current and very close to zero for oscillating currents when its temperature drops below a critical

temperature. These SCRF cavities increase the complexity of the system as they need to be contained inside of dual layer dewers (cryomodules) to keep them below this critical temperature, where they become superconducting. A cryomodule contains two major layers: the inner vessel contains liquid helium in direct contact with the outside of the cavity, cooling the cavity to the necessary 2 K to 4 K temperatures, and an outer vessel contains a liquid nitrogen bath in contact with the liquid helium dewer that prevents excessive boil off of the liquid helium. A cryoplant may also be required to replace the liquid gases that have evaporated, which adds an extra component to the system and increases complexity.

For the Niowave THz FEL, a base frequency of ~350 MHz is being used in a normal conducting copper cavity of the injector. This base frequency will be gated to 43.75 MHz to increase the charge per micropulse, or separated group of electrons.

2. Linear Accelerator

After the electron bunches are initially accelerated by the injector they are not up to the desired energy for the FEL interaction; therefore, a linac is formed from a group of RF cavities to further accelerate the beam. The number and size of the accelerating cavities depend on the final energy and the RF frequency being used; the cavities can also be either normal conducting or superconducting. Designs for linacs generally follow a series of elliptical or cylindrical cavities placed end-to-end. An example can be seen in Figure 3.

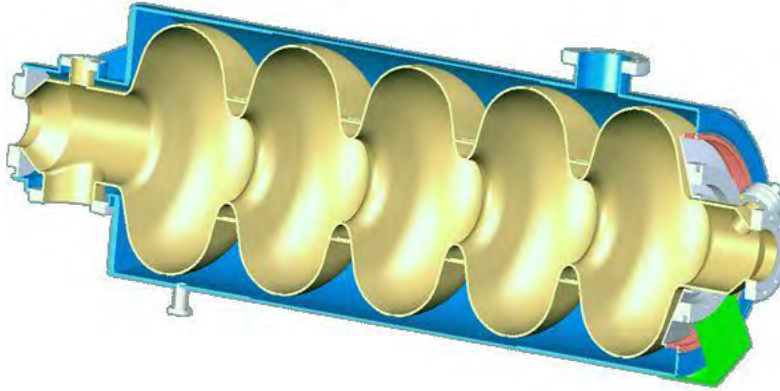


Figure 3. Cross section of five cell superconducting elliptical cavity accelerator, from [25].

While these are widely used shapes for both normal conducting and superconducting RF accelerators, they are not the only ones available. Another option is a “spoke cavity” configuration to accelerate the electron beam. This geometry contains a similar cavity shape with a “spoke” in the middle. This spoke has an axial hole in it that acts as a drift tube where the electron bunch is shielded from the RF fields when they are in the wrong phase (as seen in Figure 4).

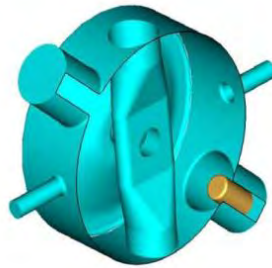


Figure 4. Schematic of single spoke cavity, from [26].

Just as in elliptical cavity linacs, several of these spoke structures can be placed in series to provide additional acceleration. One main benefit of this geometry is that for the same sustained RF frequency, the radius of a spoke cavity is approximately one half that of an elliptical cavity [27], so a lower base RF value can be used without increasing the dimensions of the cavity. Lower RF values are desirable since they decrease ohmic

losses, possibly allowing for 4 K level refrigeration to be used instead of a larger, more complex 2 K cryoplant. This shape also allows fewer mechanical vibrational modes to couple to the EM field than the equivalent elliptical cavity [28]. These properties make a spoke cavity design desirable for possible shipboard applications. A superconducting three-spoke cavity linac is chosen for the Niowave THz FEL to produce the final 8 MeV electron beam energy.

3. Undulator

An undulator is needed to transfer energy from the relativistic electron beam to the light pulse. An undulator consists of two rows of permanent magnets, each with alternating pole faces, on either side of the beam pipe. This creates a transverse periodic magnetic field causes the electron beam to wiggle. The Lorentz force causes transverse oscillations in the electron bunch, which couples the electron motion to the optical field generated by the previous electron bunches, and allows the net energy transfer to occur. A diagram of a permanent magnet undulator is seen in Figure 5.

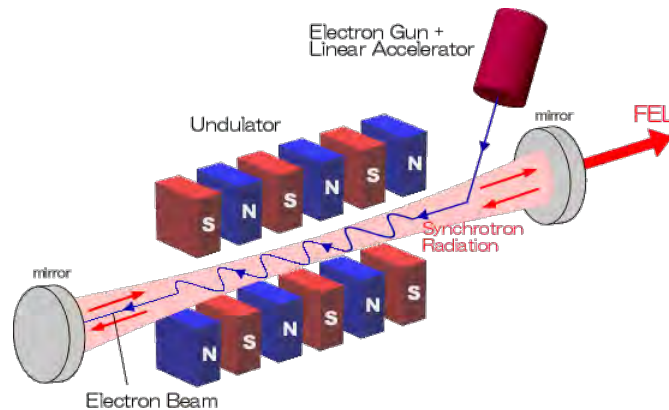


Figure 5. Permanent magnetic undulator schematic with electron beam, from [29].

An in-depth analysis of this interaction will be discussed in a later chapter.

4. Electron Beam Control

The electron beam is contained in vacuum from the cathode surface to the beam dump to prevent interaction by air molecules. The electron beam needs to be controlled

from when it is created at the injector, through the accelerating sections of the linac, directed into the undulator, and then finally disposed of in a beam dump. This steering is done with static magnetic fields. The two main necessities for electron beam control are the ability to focus the electron beam and to bend the beam to stay within the geometry of the beam line. A set of two or three quadrupoles can be used to supply focusing in both transverse directions. A dipole magnet is used to supply a magnetic field across the electron beam's path to alter its trajectory. Design of these magnets will be discussed in more depth in a later chapter.

5. Optical Cavity

The optical cavity surrounding the undulator allows the optical field to build up over multiple passes through the electron/light interaction region in the undulator. However, the mirror material selected can decrease the ability to tune the FEL, as the mirrors must reflect all radiation in the tunable range. For the Niowave THz FEL, a gold coated mirror has been chosen due to its high reflectivity in the THz frequency band. Further design considerations will be discussed in a later chapter.

One common method uses a partially transmissive mirror to allow a small percentage of the radiation power through. This is often a preferable method as it does not clip or distort the wavefront of the optical pulse, but it can only be utilized for certain wavelength ranges and power levels due to its dependency on the optical characteristics of the mirror material at the desired wavelength. Another method is a hole-outcoupling technique where the mirror has a small hole allowing a small percentage of the radiation to escape. The choice of hole outcoupling for the Niowave THz optical cavity will be discussed in a later chapter.

B. FEL THEORY

The generation of coherent radiation stems from the electron bunches' interaction with the magnetic field of the undulator and the EM fields of the light.

1. Electron Equations of Motion

The relativistic Lorentz force between an electron and both the electromagnetic fields of the undulator and the optical pulse is (in cgs units)

$$\vec{F} = m \frac{d(\gamma \vec{\beta} c)}{dt} = -e[\vec{E} + (\vec{\beta} \times \vec{B})] \quad \text{Eq. 2.1}$$

which leads to an acceleration

$$\frac{d(\gamma \vec{\beta})}{dt} = -\frac{e}{mc} (\vec{E} + \vec{\beta} \times \vec{B}), \quad \text{Eq. 2.2}$$

where m is the electron mass, e is the electron charge magnitude, $\vec{\beta} = \vec{v}/c$ is the dimensionless electron velocity, \vec{B} is the magnetic field, \vec{E} is the total electric field, and $\gamma = 1/\sqrt{1 - |\vec{\beta}|^2}$ is the relativistic Lorentz factor. The energy equation for the electrons is the fourth component of the relativistic Lorentz force equation,

$$\frac{d\gamma}{dt} = \dot{\gamma} = -\frac{e}{mc} \vec{\beta} \cdot \vec{E}, \quad \text{Eq. 2.3}$$

which describes the change in energy of the electron subject to an electric field. In order for energy exchange to occur, the electron must have a component of the velocity $\vec{\beta}$ in the transverse direction to couple to the periodic transverse electric field of the light.

2. Electron Motion in the Undulator Field

The relativistic electron experiences the largest net force from the periodic magnetic field of the undulator. For simplicity now, it is assumed that the transverse motion of the electron in the undulator is primarily due to the undulator field, and so that the electron's energy remains approximately constant throughout the interaction. A helical undulator has a magnetic field that spirals along the length of the undulator according to

$$\vec{B}_u = B_o [\cos(k_o z) \hat{i} + \sin(k_o z) \hat{j}], \quad \text{Eq. 2.4}$$

where $k_o = 2\pi/\lambda_o$, λ_o is the undulator period, and B_o is the undulator field strength. Substituting this equation into the Lorentz force equation (Eq. 2.2) and separating $\vec{\beta}$ into its constituent parts leads to

$$\frac{d\vec{\beta}_\perp}{dt} = \frac{eB_o\beta_z}{m\gamma c} [-\sin(k_o z)\hat{i} + \cos(k_o z)\hat{j}], \quad \text{Eq. 2.5}$$

where $\vec{\beta}_\perp$ is the transverse velocity of the electron. Integrating Eq. 2.5 into perfect helical orbits leads to

$$\vec{\beta}_\perp = -\frac{K}{\gamma} [\cos(k_o z)\hat{i} + \sin(k_o z)\hat{j}], \quad \text{Eq. 2.6}$$

where $K = \frac{eB\lambda_o}{2\pi mc^2}$ is the dimensionless undulator parameter, and the constants of integration are set to zero.

To evaluate a small energy change from equation (Eq. 2.3), the electric field of the light must be considered. In a helical undulator, the light will be helically polarized, with an electric field of the form $\vec{E} = E[\cos(\psi)\hat{i} - \sin(\psi)\hat{j}]$, where $\psi = kz - \omega t + \varphi$, $k = 2\pi/\lambda$, λ is the optical wavelength, $\omega = 2\pi f = 2\pi c/\lambda$ is the angular frequency, and φ is the optical phase. Inserting the electric field into Eq. 2.3 leads to

$$\dot{\gamma} = -\frac{eE}{m_e c} (\beta_x \cos(\psi) - \beta_y \sin(\psi)). \quad \text{Eq. 2.7}$$

Substituting β_x and β_y from Eq. 2.6 into Eq. 2.7 leads to

$$\dot{\gamma} = \frac{eKE}{\gamma mc} \cos(k_o z + kz - \omega t + \varphi) = \frac{eKE}{\gamma mc} \cos(\zeta + \varphi), \quad \text{Eq. 2.8}$$

where $\zeta = (k_o + k)z - \omega t$ is the electron phase, which describes the position of the electron on the scale of an optical wavelength.

3. Resonance Condition

To transfer energy from an electron to optical field, the relation $\dot{\gamma} < 0$ must be met. From Eq. 2.11, $\dot{\gamma} \propto \cos(\zeta + \varphi)$, loss of the electron energy occurs near $\zeta + \varphi = (k_o + k)\beta_z ct - \omega t + \varphi \approx \pi$. To ensure that the electrons persistently lose energy, $\dot{\gamma} < 0$ and $\zeta + \varphi \approx \pi$ always, the electron phase must not change significantly, so that

$$\dot{\zeta} = (k_o + k)\beta_z c - \omega \approx 0. \quad \text{Eq. 2.9}$$

Making the substitutions that $\omega = kc$, $k_o = 2\pi/\lambda_o$, and $k = 2\pi/\lambda$ leads to

$$\lambda \approx \frac{\lambda_o(1-\beta_z)}{\beta_z}, \quad \text{Eq. 2.10}$$

which describes the wavelength of light that has the maximum energy transfer from an electron traveling along the undulator axis with speed $c\beta_z$. To put this into a more useful form, a few simple substitutions can be made. The definition of the relativistic Lorentz factor, $\gamma^{-2} = 1 - |\vec{\beta}|^2 = 1 - \beta_x^2 - \beta_y^2 - \beta_z^2$, combined with Eq. 2.6, leads to

$$\gamma^{-2} = 1 - \left(\frac{K}{\gamma}\right)^2 [\cos(k_o z)^2 + \sin(k_o z)^2] - \beta_z^2. \quad \text{Eq. 2.11}$$

Since the portion inside the square brackets of Eq. 2.11 is identically equal to one,

$$\beta_z = \sqrt{1 - \frac{(1+K^2)}{\gamma^2}}. \quad \text{Eq. 2.12}$$

Expanding the square root as a Taylor series, and for relativistic electrons $(1+K^2)/\gamma^2 \ll 1$, leads to

$$\lambda \approx \frac{\lambda_o(1+K^2)}{2\gamma^2}. \quad \text{Eq. 2.13}$$

This gives the approximate wavelength of light the FEL emit at for a particular undulator configuration and electron beam energy. It clearly shows that FELs can be designed and tuned to operate at any wavelength, depending on the electron beam and undulator parameters.

4. FEL Pendulum Equation

It is essential to describe the FEL interaction by looking at how the electron's phase evolves as the electron travels through the undulator. To aid in this approach, a new dimensionless unit of time is introduced, $\tau = \frac{c}{L}t$, where $L=N\lambda_o$ is the undulator length. As the electron traverses the undulator, the dimensionless time changes from $\tau=0 \rightarrow 1$. This leads to $d\tau = \frac{c}{L}dt$, and a shorthand notation is defined as $\dot{(_)} = d(_)/d\tau$. Taking the derivative of the electron phase with respect to τ leads to the electron phase velocity

$$v \equiv \frac{d\zeta}{d\tau} = \frac{L}{c} \frac{d}{dt} [(k_o + k)z - \omega t] = L[(k_o + k)\beta_z - k]. \quad \text{Eq. 2.14}$$

To find the rate of change of the electron phase velocity, v is differentiated again with respect to τ ,

$$\dot{\nu} = \frac{L}{c} \frac{d\nu}{dt} = \frac{L^2}{c} (k_o + k) \dot{\beta}_z \approx \frac{L^2}{c} k \dot{\beta}_z, \quad \text{Eq. 2.15}$$

making the approximation that $k \gg k_o$, equivalent to assuming $\gamma \gg 1$ near resonance. Taking the expansion of Eq. 2.12,

$$b_z \gg 1 - \frac{(1+K^2)}{2g^2} \quad \text{Eq. 2.16}$$

and then taking the derivative with respect to time,

$$\dot{\beta}_z \approx (1+K^2) \frac{\dot{\gamma}}{\gamma^3}, \quad \text{Eq. 2.17}$$

leads to an expression involving the change in electron energy (Eq. 2.8). Recall the definition of the optical wave number, which at resonance (Eq. 2.13) has a value of

$$k \approx 2\pi \left[\frac{2\gamma^2}{\lambda_o(1+K^2)} \right]. \quad \text{Eq. 2.18}$$

Substituting Eq. 2.18 and Eq. 2.17 into Eq. 2.15 leads to

$$\dot{\nu} = \frac{L}{c} 4\pi N \frac{\dot{\gamma}}{\gamma}, \quad \text{Eq. 2.19}$$

where $N=L/\lambda_o$ is the number of undulator periods. Inserting Eq. 2.8 into Eq. 2.19 then gives

$$\dot{\nu} = |a| \cos(\zeta + \varphi), \quad \text{Eq. 2.20}$$

where $|a| = 4\pi NeKL|E|/\gamma^2 mc^2$ is the dimensionless optical field amplitude ($|E|$ is the optical electric field amplitude in cgs units). Eq. 2.20 is the same form of the differential equation that describes the evolution of a simple pendulum, $\ddot{\theta} = -\alpha \sin(\theta)$. This allows the FEL physics to be described using much the same terminology and concepts as the simple pendulum, which helps gain insight into the interaction between the electrons and the light. Studying the phase space evolution of an electron during the FEL interaction allows an intuitive view of how the electron energies are evolving in time as they traverse the undulator. Figure 6 shows the phase space diagram for a simple pendulum.

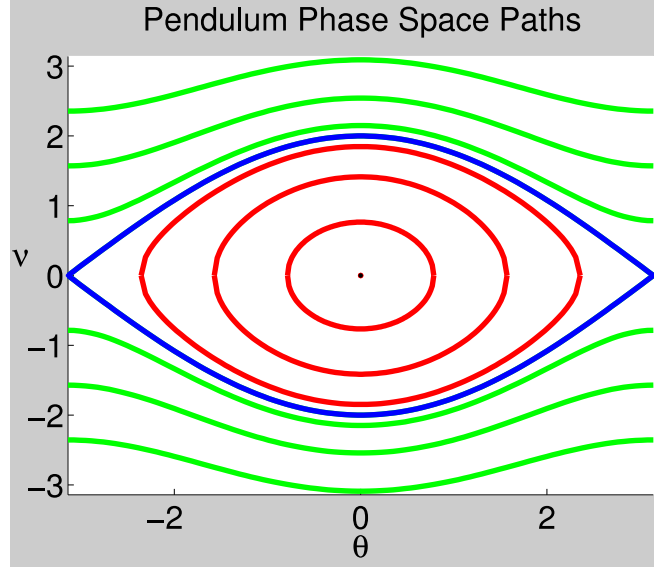


Figure 6. Pendulum phase space plot.

The blue line denotes the “separatrix” which follows the phase space path of a pendulum that has just enough energy to get to the top, $\theta=\pi$, but not go over. All orbits inside of this line are “closed orbits” corresponding to pendula swinging back and forth with amplitude $\theta_{max}<\pi$. The orbits outside of the separatrix are “open orbits” where the pendula have enough kinetic energy to overcome the gravitational potential energy and continually swing over the top, moving in the same angular direction. The pendulum’s orbit is determined by its initial conditions. The phase space trajectories describe the transfer of energy between the potential and kinetic energy of the pendulum and gives insight into the FEL interaction.

Translating these ideas over to the physics of an FEL interaction involves thinking about the electron beam as a whole. As was stated, the electron phase ζ measures the position on the scale of a wavelength of light; a typical electron bunch is ~ 1000 optical wavelengths long, and has $\sim 10^6$ electrons in each optical wavelength λ . This indicates that the electrons are initially spread randomly over each optical wavelength. The phase velocities v of the electrons are determined by the electron’s energies. Figure 7 shows snapshots of the electron beam phase space as it evolves through the undulator from $\tau=0 \rightarrow 1$ of a typical FEL on resonance with low gain. The blue dots represent samples

electrons while the separatrix (red line) is given by $n^2 = 2|a|[1 + \sin(Z + j)]$, with a height of $2|a|^{1/2}$.

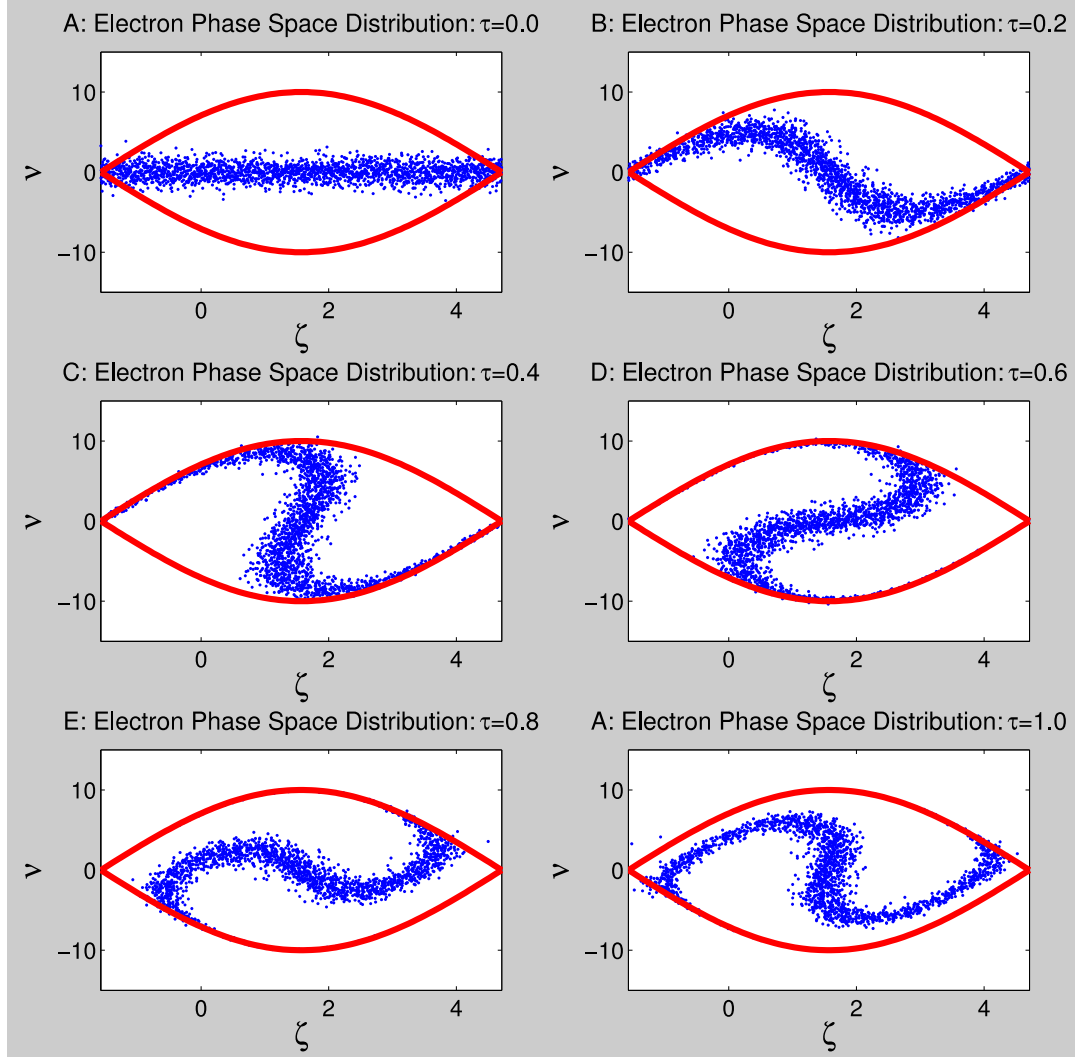


Figure 7. The phase space procession of the electrons during the FEL interaction about $v_o=0$.

Figure 7 A in the upper left shows the initial phase space distribution of the electrons at $\tau=0$ with a phase velocity spread about $v_o=0$, corresponding to resonance. For the sake of this example an initial field amplitude of $a_o=25$ was used. As the FEL interaction progresses (B, C, D, E, F) the electrons follow phase space trajectories that are described by the FEL pendulum equation. Electrons at an initial phase $\zeta > \pi/2$ lose energy

(ν decreases), while electrons at an initial phase $\zeta < \pi/2$ gain energy (ν increases). By conservation of energy the only place for the energy to go from the electrons is into the optical field. In this example, about half the electrons gain energy and half lose energy, so very little net energy is transferred into the optical field. Figure 8 shows how to make the FEL “work” by operating off resonance.

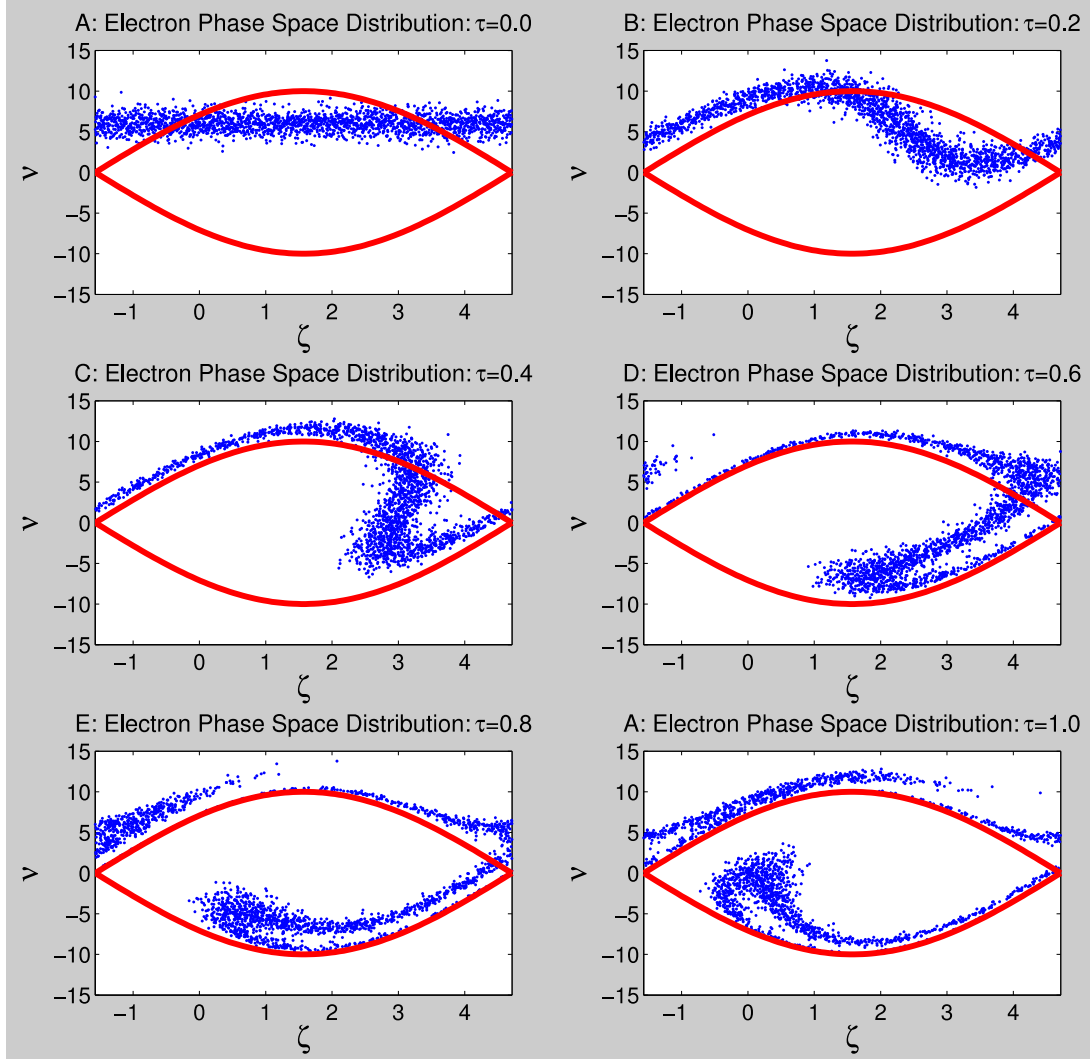


Figure 8. The phase space procession of the electrons during the FEL interaction about $\nu_o=6$.

As in Figure 7, Figure 8 shows the progression of the phase space trajectories for an electron beam as it undergoes the FEL process. In this case, the initial electron phase

velocity is centered off resonance around $\nu_o=6$. This leads to the majority of electrons who start inside the separatrix to lose energy as $\tau=0 \rightarrow 1$. This net energy transfer leads to an increase in the optical field.

5. Optical Field Evolution

For the FEL process to be understood self-consistently, it is necessary to study the optical field evolution.

a. *Spontaneous Emission*

Light is initially created by spontaneous emission from the transverse acceleration of the relativistic electron beam. This radiation is projected in a forward cone with an angle width of $\sim 1/\gamma$. The spontaneous emission will have a spectral width of $\sim 1/N$ centered on the resonant wavelength of the FEL.

b. *Weak Field Gain*

For the FEL process to work, net energy must be transferred from the electron beam to the optical pulse. From the average electron phase velocity change of the electron beam, $\langle \Delta \nu \rangle$, one can determine the average loss of energy by the bunch, $\langle \Delta \gamma m c^2 \rangle$, from Eq. 2.22, and thus the energy gained by the optical field. As the FEL turns on, the optical fields produced by spontaneous emission are very small, $|a| \ll \pi$. In weak fields with low gain, $|a| \approx a_o$. Using perturbation theory, one can solve the pendulum equation in powers of a_o . To 0th order in a_o , the solution is trivial: with no optical field there is no energy change. To 1st order in a_o , when the solution is averaged over the whole electron beam spread over an optical period the resultant energy change is, again, identically zero. One must go out to 2nd order in a_o before finding a non-zero solution [30],

$$\langle \Delta \nu \rangle = \frac{|a_o|^2}{\nu_o^3} [\cos(\nu_o \tau) - 1 + \nu_o \tau \sin(\nu_o \tau)/2] . \quad \text{Eq. 2.21}$$

To find the total energy change of the electron beam, ΔU , one must substitute Eq. 2.21 into Eq. 2.19 and multiply by the total number of electrons in the beam, $n_e = \rho V_e$, where ρ is the electron beam density and V_e is the volume of the electron bunch

The FEL gain is defined as the change in energy of the optical pulse with respect to the initial energy in the optical pulse. The energy in the optical field is given by $U_{opt} = E^2 V_{opt} / 4\pi$, where E is the electric field amplitude and V_{opt} is the volume of the optical pulse (cgs units). Taking all of this into account leads to an equation for the weak field gain, G ,

$$G = \frac{(\gamma mc^2)}{N} \left[\frac{\langle \Delta v \rangle \rho V_e}{E_0^2 V_{opt}} \right], \quad \text{Eq. 2.22}$$

and using Eq. 2.21,

$$G = \frac{jF}{v_o^3} [2 - 2 \cos(v_o \tau) - v_o \tau \sin(v_o \tau)], \quad \text{Eq. 2.23}$$

where $j = 8 \pi^2 N e^2 K^2 L^2 \rho / \gamma^3 m c^2$ is the dimensionless current density, and $F = V_e / V_{opt} = A_e / A_{opt}$ is the filling factor, which denotes how well the electron beam with area A_e and the optical mode with area A_{opt} overlap. This solution is valid for weak fields ($a \ll \pi$) and for low gain ($j \ll 1$). Round trip gain must be higher than the round trip losses in the optical cavity for the FEL process to work. The amount of gain per pass is dependent on many factors, including the strength of the optical field, the initial electron phase velocity, and the current density. Figure 9 shows the weak field gain as a function of v_o .

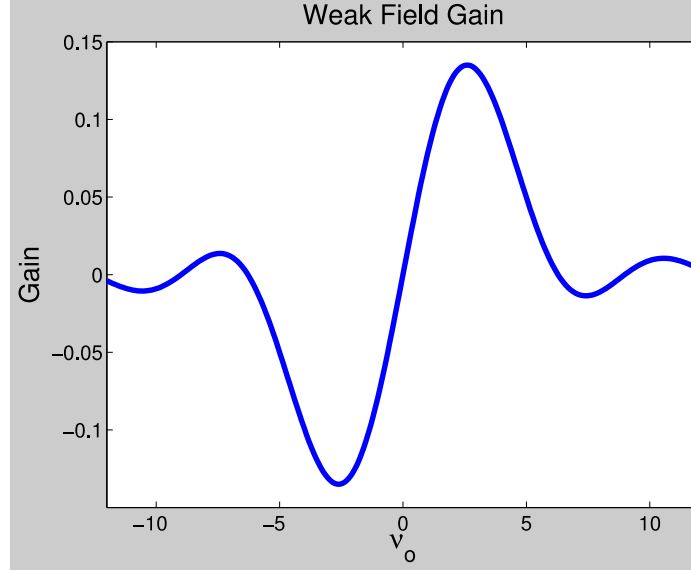


Figure 9. Weak field gain as a function of v_o .

The gain curve is approximately anti-symmetric about $v_o=0$ with the peak gain at an initial electron phase velocity $v_o \approx 2.6$. If $v_o \approx -2.6$, then the gain is negative and at a minimum, meaning that the electron bunch will take the maximum amount of energy from the optical pulse. At $v_o=0$ the gain is zero, meaning that overall the electron bunch neither gains nor loses energy to the optical pulse, which recreates the same result that is achieved from the analysis of the phase space evolution shown in Figure 7. The gain spectrum is approximately anti-symmetric with a gain bandwidth of $\Delta v_o \approx 4\pi$. From Eq. 2.19 the gain bandwidth in energy is approximately $1/N$.

c. *Coherence Development*

Like other lasers, FELs can have a relatively narrow spectrum. The light created from spontaneous emission is relatively broadband, corresponding to a wide range of initial electron phase velocities centered on resonance ($v_o=0$). As the FEL process continues, energy is preferentially transferred from the electron beam to the optical field at wavelengths near the peak of the gain curve ($v_o \approx 2.6$). As the optical pulse bounces back and forth in the cavity, gaining energy from each subsequent electron bunch, the optical spectrum becomes narrower and narrower (see Figure 10), eventually becoming transform limited.

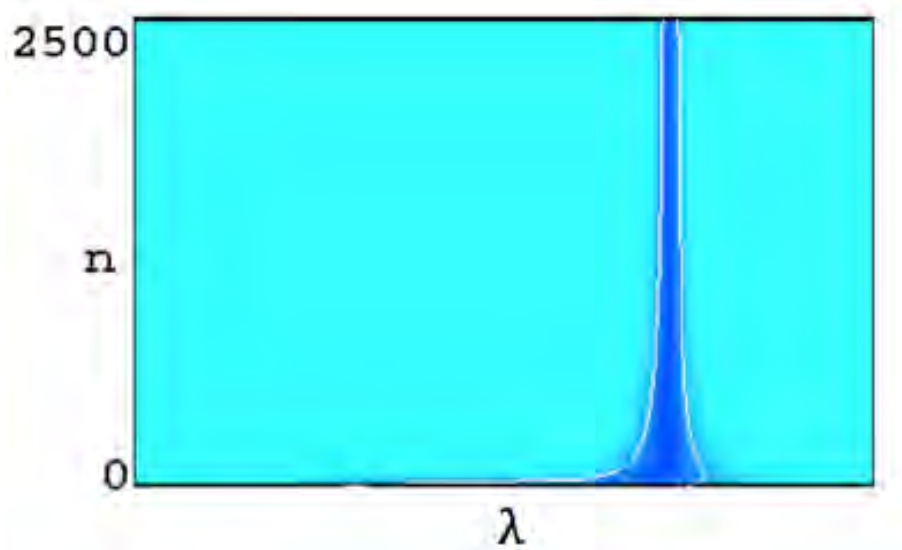


Figure 10. Coherence development over 2500 passes, from [31].

Figure 10 depicts the power spectrum of the optical pulse in an FEL over 2500 passes. As the number of passes (n) increases the width of the spectrum narrows as the gain spectrum preferentially amplifies wavelengths near peak gain.

d. Wave Equation

While the pendulum equation describes how the electrons evolve during the FEL process, the wave equation is needed to describe how the light field evolves through the undulator. To simplify the wave equation, the “slowly-varying envelope approximation” (SVEA) is used, which states that the phase and amplitude of light do not change much over one oscillation of the electromagnetic wave. This is a reasonable approximation for most lasers and is commonly used. With this framework, the wave equation can be written in terms of the vector potential, $\vec{A}(\vec{x}, t)$, and the transverse current density, $\vec{J}_\perp(\vec{x}, t)$,

$$\left(\nabla^2 - \frac{1}{c^2} \frac{\partial^2}{\partial t^2} \right) \vec{A}(\vec{x}, t) = -\frac{4\pi}{c} \vec{J}_\perp(\vec{x}, t) . \quad \text{Eq. 2.24}$$

A solution of the form

$$\vec{A}(\vec{x}, t) = \frac{E(\vec{x}, t)}{k} e^{i(kz - \omega t)} (-i\hat{t} + \hat{j}) \quad \text{Eq. 2.25}$$

can be assumed, which corresponds to a helically-polarized plane wave produced by a helical undulator. Breaking this equation into its spatial and temporal components leads to a simpler solution. Assuming no transverse dependence on the spatial component (a plane wave where $E=E(z,t)$) leaves only a longitudinal component ($\partial^2/\partial z^2$) in the Laplacian. This is a good approximation for a beam with little diffraction during evolution through the undulator. This leads to

$$\frac{\partial^2 \vec{A}}{\partial z^2} \approx \left(2ik \frac{\partial E}{\partial z} - k^2 E \right) \frac{e^{i(kz-\omega t)}}{k} (-i\hat{t} + \hat{j}), \quad \text{Eq. 2.26}$$

where the second derivative of E is ignored due to the SVEA. The temporal term can be written in much the same manner:

$$\frac{\partial^2 \vec{A}}{\partial t^2} \approx \left(-2i\omega \frac{\partial E}{\partial t} - \omega^2 E \right) \frac{e^{i(kz-\omega t)}}{k} (-i\hat{t} + \hat{j}). \quad \text{Eq. 2.27}$$

Plugging Eq. 2.27 and Eq. 2.26 into Eq. 2.24 and multiplying by the complex conjugate of the unit vector leads to

$$ik \left(\frac{\partial}{\partial z} + \frac{1}{c} \frac{\partial}{\partial t} \right) E = -\frac{\pi k}{c} \left(\vec{J}_\perp \cdot (i\hat{t} + \hat{j}) \right) e^{-i(kz-\omega t)}. \quad \text{Eq. 2.28}$$

A further development is to follow a slice of the electric field as the light travels through the undulator at speed c . This has the benefit of removing the z dependence on the left hand side of Eq. 2.28. The current density is a sum of individual electron trajectories and can be written out as $\vec{J}_\perp = -ec \sum_i \vec{\beta}_\perp \delta^{(3)}(\vec{x} - \vec{r}_i)$, where \vec{r}_i is the position of the i^{th} electron. The electrons follow the helical trajectories derived in Eq. 2.9, so the current can be written out as

$$\vec{J}_\perp = ecK \text{Re}[i(-i\hat{t} + \hat{j}) \sum_i \frac{e^{-ik_0 z_i}}{\gamma_i} \delta^{(3)}(\vec{x} - \vec{r}_i)] \quad \text{Eq. 2.29}$$

$$\vec{J}_\perp \approx ecK\rho \text{Re}[i(-i\hat{t} + \hat{j}) \left\langle \frac{e^{-ik_0 z}}{\gamma} \right\rangle], \quad \text{Eq. 2.30}$$

where the average over the electrons in the beam, $\langle \dots \rangle$, has been taken, and ρ is the electron beam density. Combining Eq. 2.30 with Eq. 2.28 then leads to the equation

$$\frac{\partial E}{\partial t} = -2\pi ecK\rho \left\langle \frac{e^{-i[(k_0+k)z-\omega t]}}{\gamma} \right\rangle. \quad \text{Eq. 2.31}$$

This describes how the optical field evolves through the undulator during the FEL process. Transforming this into dimensionless units and assuming that all the electrons in

the bunch have approximately the same energy, $\gamma \approx \gamma_o$, leads to the dimensionless FEL wave equation,

$$\dot{a} = -jF \langle e^{-i\zeta} \rangle, \quad \text{Eq. 2.32}$$

where a and j are the dimensionless optical field and the dimensionless current density as previously defined. The bracketed term is known as the “bunching” term and denotes how much the electrons have bunched on the order of a wavelength of light. If the electrons are equally spaced out over the wavelength of light then

$$\langle e^{-i\zeta_o} \rangle = \frac{1}{2\pi} \int_0^{2\pi} e^{-i\zeta_o} d\zeta_o = 0, \quad \text{Eq. 2.33}$$

so there is no change to the optical field. It is only after some transit time through the undulator where some electrons have lost energy and some have gained energy that they start to bunch on the scale of the wavelength of light. It is this bunching at a certain optical phase which leads to energy transfer to the optical field.

e. Short Pulse Effects

Until now the electron bunch length has not played a role. In real life, the electron bunch is of finite length (often \sim ps), which must be taken into consideration.

(1) Optical Lethargy

As was previously discussed, the electrons must be bunched on the scale of a wavelength of light in order to have net energy transfer between the electron bunch and the optical field. It takes some time for this bunching to develop as the electrons interact with the optical field and the undulator magnetic field, so energy transfer does not happen at the very beginning of the undulator but rather toward the end. A depiction of this can be seen in Figure 11.

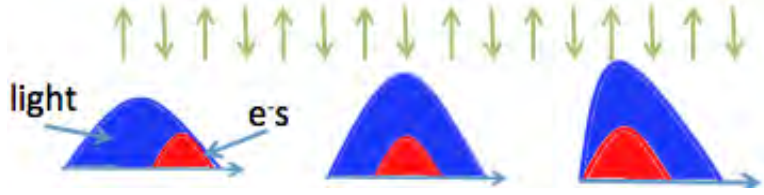


Figure 11. Depiction of optical lethargy of the light pulse transiting the undulator.

In Figure 11, the electron bunch (red) and the optical pulse (blue) are co-propagating through the undulator (green arrows) from left to right. At the beginning of the undulator the electron bunch is slightly ahead of the optical pulse. Although the electrons are highly relativistic, they still are not traveling at the speed of light, so the optical pulse overtakes it during transit. Halfway through the undulator the electrons are becoming bunched so more energy is transferred to the optical field and its amplitude begins to grow. By the end of the undulator (right), the electrons are well bunched and transfer the most energy to the optical pulse. This has the effect of amplifying the rear of the optical pulse more than the front, causing the centroid of the optical pulse to travel less than the speed of light. This effect must be taken into consideration when designing the FEL oscillator cavity.

(2) Desynchronism

The cavity length of the oscillator must be properly chosen so that the optical pulse is synchronized with each subsequent electron bunch. This distance is based on the repetition rate of the electron bunches and the speed of light, but as was previously discussed the centroid of the optical pulse is less than c . In order to counteract this effect, the length of the cavity must be shortened slightly (on the order of microns) to allow proper overlap between the electron bunches and optical pulse over many passes. If this were not taken into account then the tail of the pulse will continue to grow more than the front of the pulse and eventually would evolve away from the electron beam and the FEL would not work. Optimal values to shorten the oscillator cavity to account for desynchronism are typically between zero and $0.25 N\lambda$.

f. Electron Beam Quality

An FEL's performance is affected by the quality of the electron beam. A key metric of electron beam quality is the emittance, which is defined as the amount of volume the electron bunch takes up in phase-space. There are two types of emittance; transverse emittance denotes how the electron beam's transverse size and angular spread are correlated and is given by $\varepsilon_r = \sigma_r \sigma_\theta$, where σ_r is the rms radius of the beam and σ_θ is the rms spread in angles. Longitudinal emittance is related to the energy spread (ΔE) and the pulse length of the electron bunch (Δt_{rms}) and is given by $\varepsilon_l = \Delta E \cdot \Delta t_{rms}$. The ideal electron beam for the FEL interaction would be monoenergetic and perfectly collimated so that all the electrons could match the resonance condition, but this is not feasible. There is a trade off with electron beam generation between beam quality and the amount of current that can be achieved from an electron accelerator that must be balanced depending on the needs of the FEL.

Poor electron beam quality degrades the FEL performance by decreasing the amount of bunching that can occur. As energy is directly related to the electron phase velocity, an energy spread can be visualized as a spread in v_o (see Figure 12).

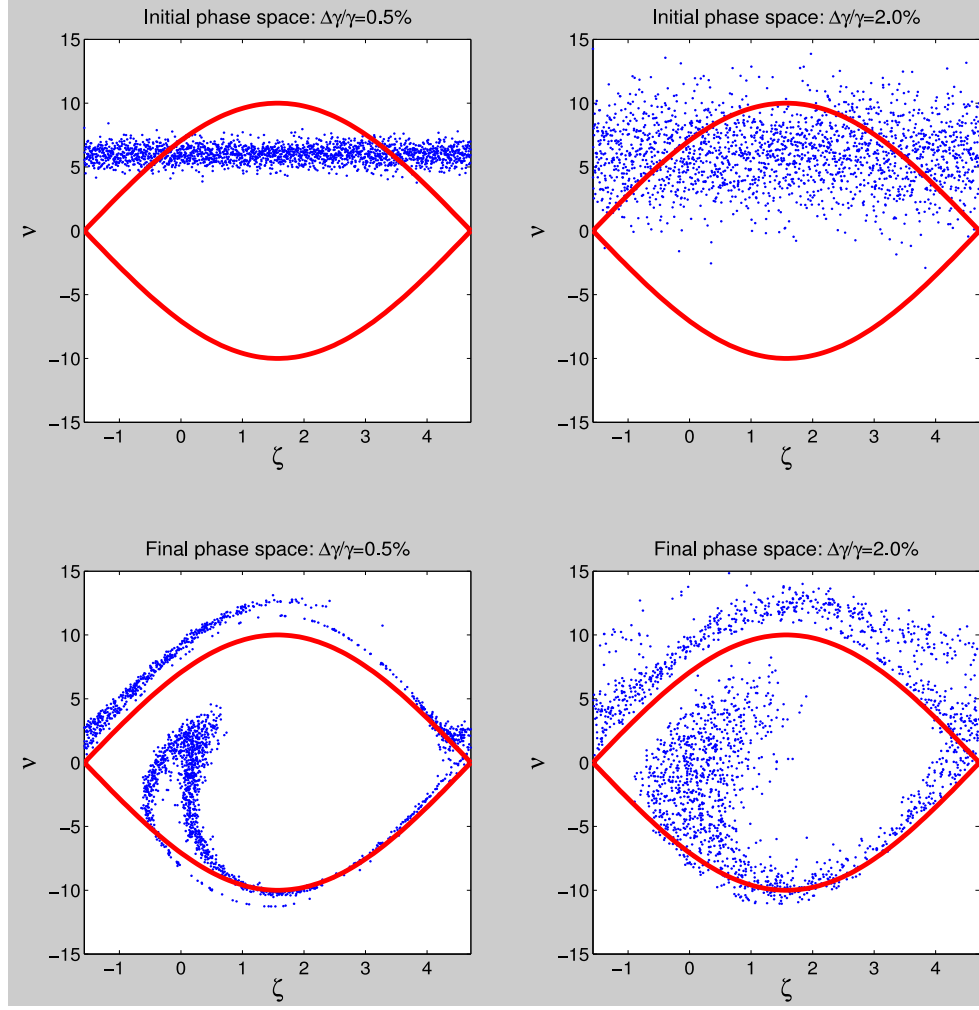


Figure 12. Comparison of energy spread of initial electron bunches, strong fields.

Figure 12 depicts simulations of an electron bunch with an initial optical field of $a_o = 25$, $j=30$ with two different energy spreads. The initial electron phase-space diagrams of a good electron bunch with a fairly minimal energy spread of 0.5 percent (left) as well as one with a larger two percent energy spread (right) can be seen on the top row. The lower two plots show the phase space diagrams at the end of the undulator after the FEL interaction. The quality of the bunching is lower with higher energy spread, which decreases the gain of the FEL. The effect can be greater in the weak field gain regime where electrons with a large phase velocity distribution are not well trapped by the weak fields. An example of this can be seen in Figure 13.

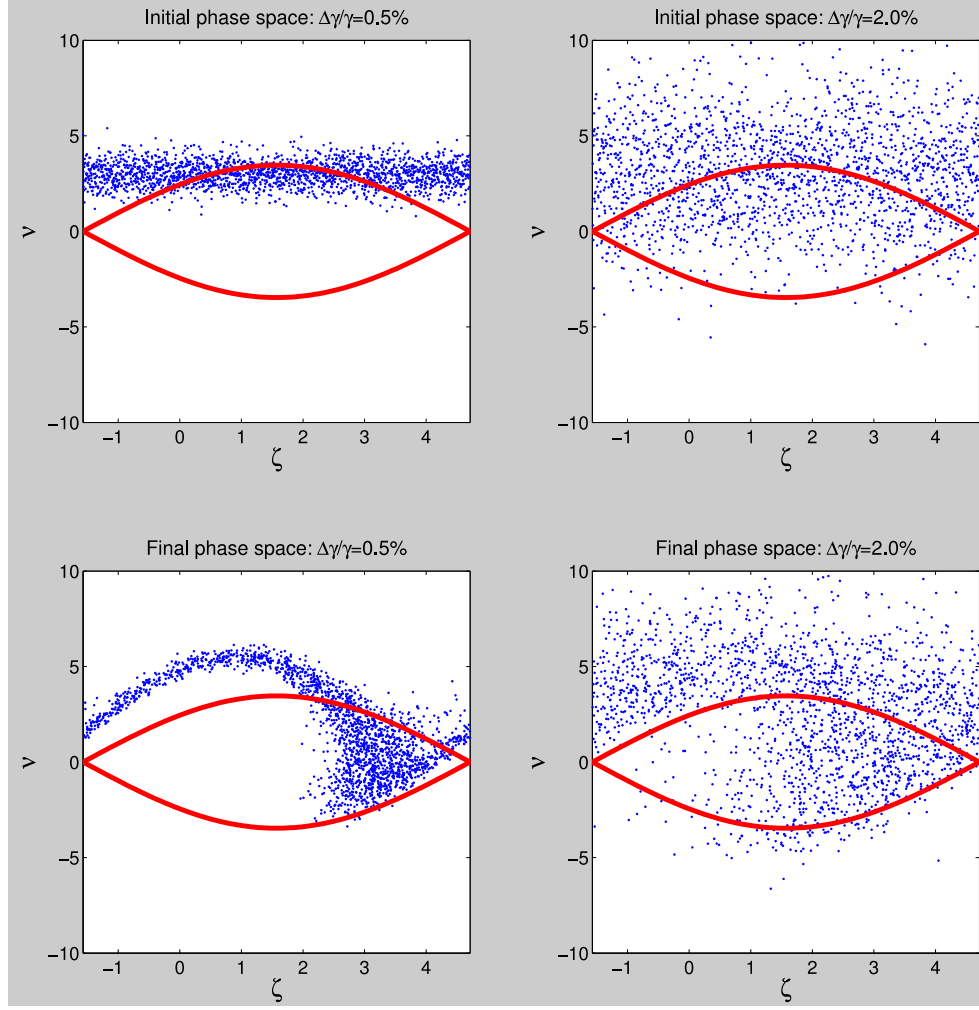


Figure 13. Comparison of energy spread of initial electron bunches, weak fields.

In the weak field regime with a small initial field ($a_0=3$ in Figure 13), the large two percent energy spread does not allow bunching to occur and reduces the weak field gain. This is a key reason to reduce the energy spread of the electron beam.

The transverse emittance has the same effect of increasing the spread in initial phase velocities. A spread in angles is equivalent to a spread in longitudinal velocities. Since v_o is proportional to β_z , this induces a spread in phase velocities in addition to the initial energy spread, which again decreases the bunching and hence the output power. Likewise, a larger beam radius will lead to stronger betatron focusing, thus again increasing the phase velocity spread and decreasing bunching and extraction.

THIS PAGE INTENTIONALLY LEFT BLANK

III. FEL SIMULATIONS

A. NOMINAL FEL PARAMETERS

The nominal parameters simulated for the Niowave FEL are listed in Tables 2–4. The electron beam energy is 8 MeV, the bunch charge is 0.2 nC, and the beam radius at waist is 0.45 mm (rms). The assumed pulse shape was parabolic with a 5 ps full width with an 8.75 mA average current. It has a normalized emittance of 28 mm-mrad, an energy spread of 1.66%, and a repetition rate of 43.75 MHz.

Beam kinetic energy	8 MeV
Bunch charge	0.2 nC
Beam radius at waist, rms	0.45 mm
Longitudinal pulse shape	Parabolic
Pulse duration, full width	5 ps
Average current	8.75 mA
Normalized emittance, rms	28 mm-mrad
Energy spread ($\Delta\gamma/\gamma$)	1.66%
Repetition rate	43.75 MHz

Table 2. Electron beam parameters being simulated.

To increase the peak current to 60 A, the injector will be gated to the eighth sub-harmonic of the base 350 MHz frequency or 43.75 MHz [32].

Undulator period (λ_o)	3.3 cm
Number of periods (N)	10
Undulator parameter (K), rms	0.72
Undulator length (L)	33 cm

Table 3. Undulator parameters being simulated.

The undulator has $N=10$ periods of $\lambda_o=3.3$ cm leading to a 33 cm length and a variable gap that can be adjusted to supply a magnetic field corresponding to an undulator parameter range of $0.72 < K < 1.42$. This has a direct effect on the resonant radiation wavelength and thus the optical cavity parameters. The resonant wavelength and the optical beam waist radius determine the geometry for the optical cavity. The mirrors' radius of curvature (~ 1.7 m), the cavity length (~ 3.42 m), the nominal radiation wavelength (93 μm) determine the Rayleigh length $z_o=11$ cm for the cavity leading to a mode waist radius of $W_o=1.82$ mm. The mirror radius is eight centimeters. The round trip loss was assumed to be 6% due to output coupling and mirror losses. These parameters are listed in Table 4.

Cavity length (S)	3.428 m
Rayleigh length (z_o)	11 cm
Resonant wavelength (λ)	93 μm
Mode waist radius ($1/e$)	1.82 mm
Mirror radius of curvature	~ 1.7 m
Mirror radius	8 cm
Round trip losses	6%

Table 4. Optical cavity parameters being simulated.

B. CODE DESCRIPTIONS

Computer codes have been developed that model the FEL interaction and are based on the theory first described in the 1970s [33]. Three different FEL codes are discussed and used in this dissertation: the first is *GINGER*, a widely used code created by scientists at Lawrence Berkeley National Laboratory [34]; the second is *4DPULSEN* developed by the Naval Postgraduate School; the last is a code was written by the author of this dissertation.

1. GINGER

GINGER is a transverse multidimensional (including r - t components in the fields and x - y - t in the electrons) and polychromatic FEL simulation. For this study the code was run in a monochromatic mode, which ignores longitudinal pulse shape effects but does take into account optical beam diffraction. One benefit of *GINGER* is its ability to input electron beam parameters from external particle tracking codes relatively easily.

2. 4DPULSEN

Researchers at the Naval Postgraduate School have created a suite of FEL codes that model the interactions in a number of ways. One of the newest is a 4D pulse code that models the electron beam and the optical field in x, y, z , and t , and includes pulse slippage, desynchronism, and diffraction effects. The code can model an FEL oscillator and is used to study stability criteria by shifting and tilting the mirrors. The code is parallelized and runs on a cluster computer; with ~ 100 nodes the simulation takes ~ 3 seconds per pass, and may run over thousands of passes.

3. 1D FEL Code

An FEL code was written by the author of this dissertation to calculate gain and extraction (percentage of electron beam power transferred to the optical pulse). This is a 1D code that tracks the electrons' phase space evolution as they traverse the undulator using the FEL pendulum and wave equations discussed in Chapter 2. It utilizes the Euler-Cromer method to iteratively step through the coupled partial differential equations. In each time step Δt , the change in each electron's phase velocity is calculated using $\Delta v = (a_r \cos(\zeta) - a_i \sin(\zeta))\Delta t$, where a_r and a_i are the real and imaginary parts of the dimensionless optical field. Next the new electron phase velocity, $v(t + \Delta t) = v(t) + \Delta v$, is used to update the electron phase, $\zeta(t + \Delta t) = \zeta(t) + v(t + \Delta t)\Delta t$. This is done for each individual electron. At the end of the time step, the changes in the optical field is calculated using the expanded version of Eq. 2.34, leading to

$$\Delta a_r = -jF\langle \cos(\zeta) \rangle \cdot \Delta t, \quad \text{Eq. 3.1}$$

and

$$\Delta a_i = jF\langle \sin(\zeta) \rangle \cdot \Delta t, \quad \text{Eq. 3.2}$$

where $\langle \dots \rangle$ represents an average over the sample electrons and j is the dimensionless current density and F is the filling factor. This new optical field is then used to calculate the electron phase velocity change Δv of the next time step. In updating the electron phases, periodic boundary conditions are used to maintain $-\pi/2 < \zeta < 3\pi/2$ for each electron. The initial optical power, $a_o^2 = a_{ro}^2 + a_{io}^2$, is calculated at the beginning of the undulator from the initial components a_{ro} and a_{io} . The real and imaginary components at the end of the undulator (a_{rf} and a_{if} respectively) are used to calculate the final power, $a_f^2 = a_{rf}^2 + a_{if}^2$. The gain is calculated from the fractional change in the optical power over the initial optical power,

$$G = \frac{a_f^2 - a_o^2}{a_o^2}. \quad \text{Eq. 3.3}$$

Key inputs into the code include the initial dimensionless field components a_{ro} and a_{io} , the dimensionless current density j , the filling factor F , and the energy spread of the electron beam. This code is useful for its ability to show trends in the performance of the FEL by being able to do a large number of simulations quickly and on a machine with minimal processing power.

C. GAIN SPECTRUM

The weak field gain (G) of the FEL describes how the optical pulse gains energy over each pass before the onset of saturation. The gain is dependent on the initial electron phase velocity (amongst other things). Figure 14 compares the 1D simulation results to the analytic solution (Eq. 2.26).

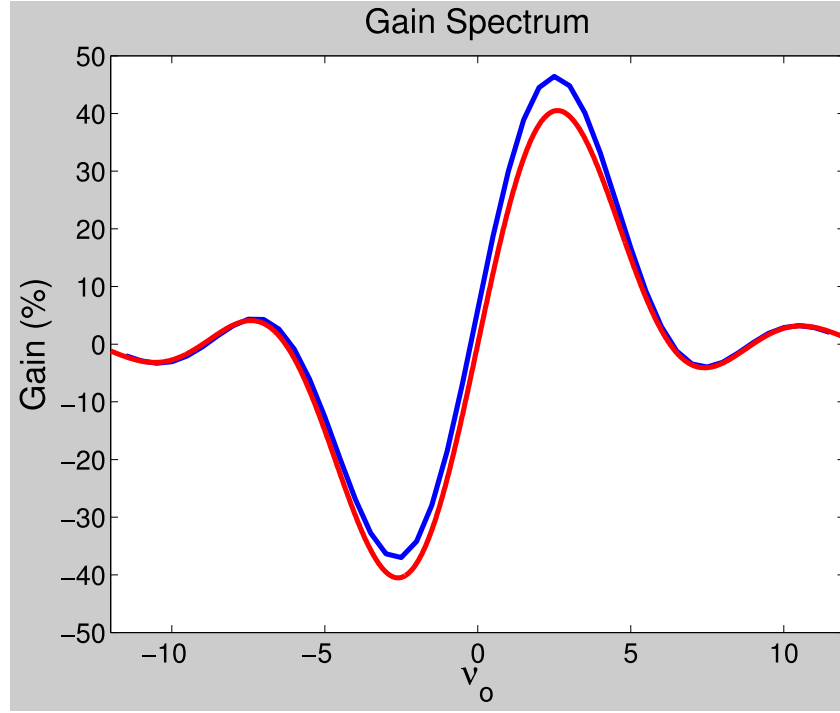


Figure 14. 1D simulation results (blue) and analytic solution (red) of gain spectrum of Niowave THz FEL for 0% energy spread.

The analytic solution does not take into account energy spread, so the spread was set to zero for this simulation; all other parameters are the nominal parameters in Tables 2–4 corresponding to a dimensionless current density $j \approx 3$. The 1D simulation (blue) obtains a maximum $G \approx 46\%$ at $v_o \approx 2.5$, similar to the analytic solution (red). The self-consistent update of the radiation field in the simulation (blue) causes the asymmetry of slightly smaller loss compared to the analytic solution where the field is held constant. However, care must be taken when analyzing these results. Diffraction and longitudinal pulse effects of the FEL will cause a decrease in the gain. The slippage length ($N\lambda \approx 1$ mm) is on the order of the pulse length (5 ps \rightarrow ~ 1 mm), which will decrease the overlap of the electron beam with the optical pulse.

The 1D code can also be used for non-monoenergetic beams. An energy spread corresponds to a spread in phase velocities, which will cause different electrons to be spread into different portions of the gain spectrum. A depiction of this can be seen in Figure 15.

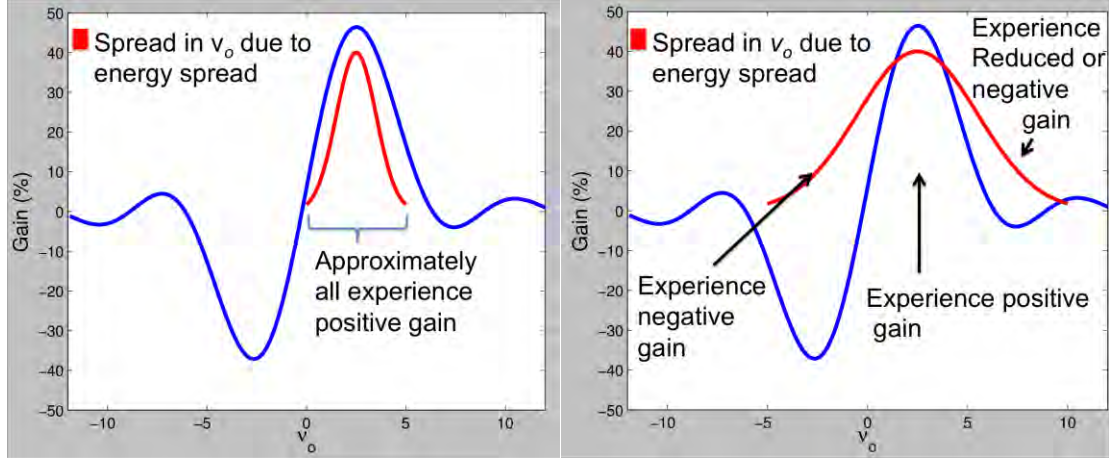


Figure 15. Gain spectrum (blue) with energy spread overlay (red).

The graphs in Figure 15 show the same nominal gain spectrum (blue) that was simulated in Figure 14 with an overlay of a nominal energy spread in the electron beam (red). The left graph shows a small energy spread where approximately all electrons still contribute to positive gain causing the peak gain to still occur at $v_o \approx 2.6$. In the right graph of Figure 15, the energy spread is much larger resulting in some electrons experiencing reduced or even negative gain. Some of the electrons on the left side of the distribution experience negative gain, taking energy out of the optical pulse. The middle portion still experience positive gain while those to the right of the peak have reduced gain. The net effect causes the value of v_o giving the best gain to shift to the right. Applying this code to the realistic electron beam of the Niowave THz FEL with an energy spread of $\Delta\gamma/\gamma \approx 1.66\%$ leads to the resultant gain spectrum in Figure 16.

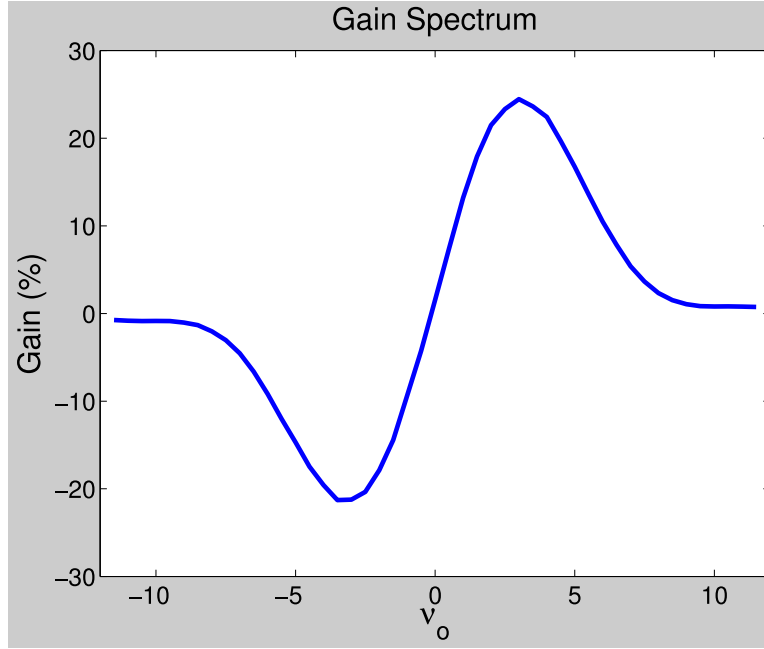


Figure 16. Gain spectrum of Niowave THz FEL: $\Delta\gamma/\gamma=1.66\%$.

The gain spectrum has the same approximate anti-symmetry as the nominal mono-energetic beam case but some new key features are that the peak gain is reduced from $\sim 46\%$ to $\sim 24\%$, the position of the peak is shifted slightly, from $v_o \approx 2.6$ to $v_o \approx 3$ for the reasons discussed above, and the side peaks of local maxima have disappeared. Recall that a shift in v_o corresponds to a shift in wavelength, so this modified gain spectrum alters the wavelength that is preferentially amplified on each pass through the undulator.

Using the parameters in Tables 2–4, *GINGER* can be used to take into account energy spread and diffraction effects of the optical pulse. The resulting gain spectrum is shown Figure 17.

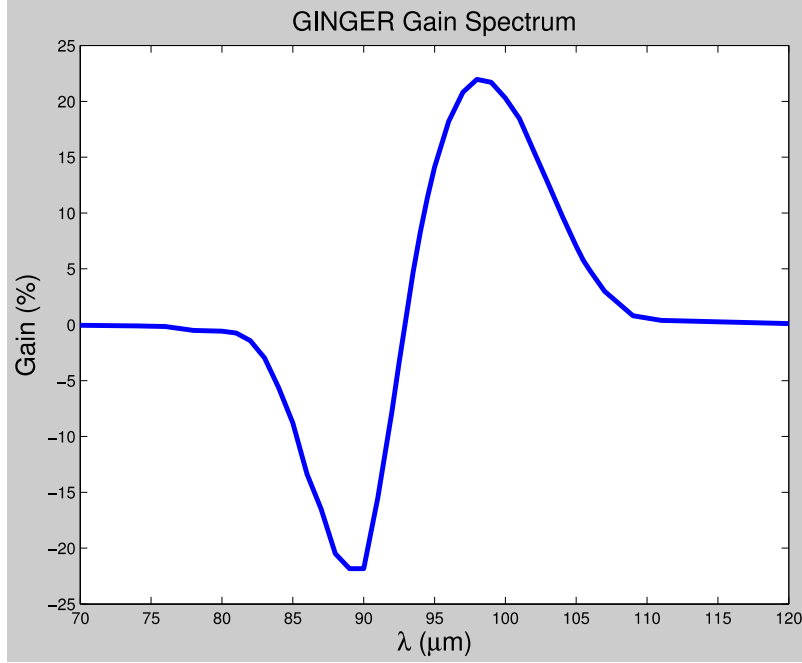


Figure 17. Scan of weak field gain vs. wavelength using *GINGER* FEL code for the Niowave FEL parameters.

The shape shows good agreement with Figure 16 including the approximate anti-symmetric shape of the gain spectrum and the flattening of the side lobes due to the energy spread, and approximately the same peak gain of $G \approx 22\%$.

D. WEAK FIELD GAIN VS. ENERGY SPREAD

The gain was studied as a function of energy spread in the electron beam using the three codes. Simulations were done varying the energy spread from zero percent, the ideal case, up to 3.25 percent, an extreme case. For all simulations, a Gaussian energy spread shape was assumed. The results from the 1D code can be seen in Figure 18.

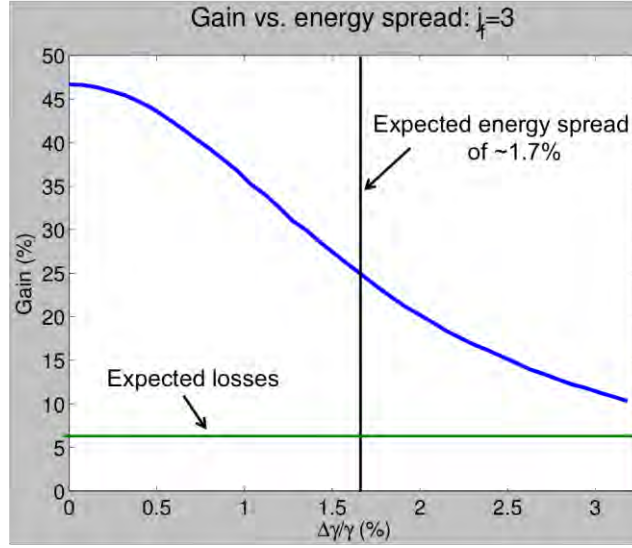


Figure 18. Gain degradation from energy spread using 1D code.

With no energy spread the 1D simulations show the FEL would have $G \approx 46$ and in the worst-case scenario, a 3.25 percent energy spread leads to $G \approx 10\%$. For the Niowave THz FEL, an energy spread of $\Delta\gamma/\gamma \approx 1.7\%$ is expected from the linac from preliminary measurements and simulations corresponding to a $G \approx 25\%$ in Figure 18. The green line denotes the expected six percent round trip losses of the cavity. While this is a relatively high gain and allows for a large amount of loss, this simple 1D code does not take into account diffraction or longitudinal pulse effects.

To analyze the effects of diffraction and short pulses on the expected performance, *GINGER* and *4DPULSEN* can be used to scan through the energy spread. These results are seen in Figure 19.

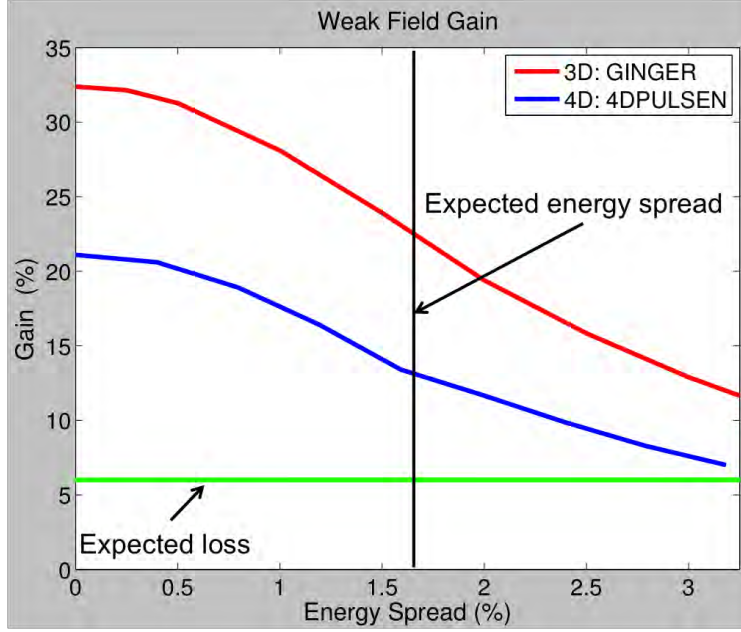


Figure 19. *GINGER* (red) and *4DPULSEN* (blue) code results of gain against initial electron energy spread for the Niowave THz FEL.

The results for *GINGER* (red line), which takes into account diffraction, show a reduced gain of $G \approx 32\%$ for the ideal case and a value of $G \approx 22\%$ at the expected energy spread. As was stated, in the monochromatic mode that was used, *GINGER* does not take into account the longitudinal pulse profile of the electron beam and is therefore optimistic. Short pulse effects will cause the FEL gain to decrease due to poor overlap between the radiation pulse and electron pulse during the interaction, as can be seen by the reduced gain the *4DPULSEN* code predicts (blue). This code predicts only a $G \approx 22\%$ for the monoenergetic beam case and $G \approx 13\%$ for the expected energy spread. For each data point of the 4D code the amount of desynchronism was altered to maximize the gain. A few results of the desynchronism scan can be seen in Figure 20.

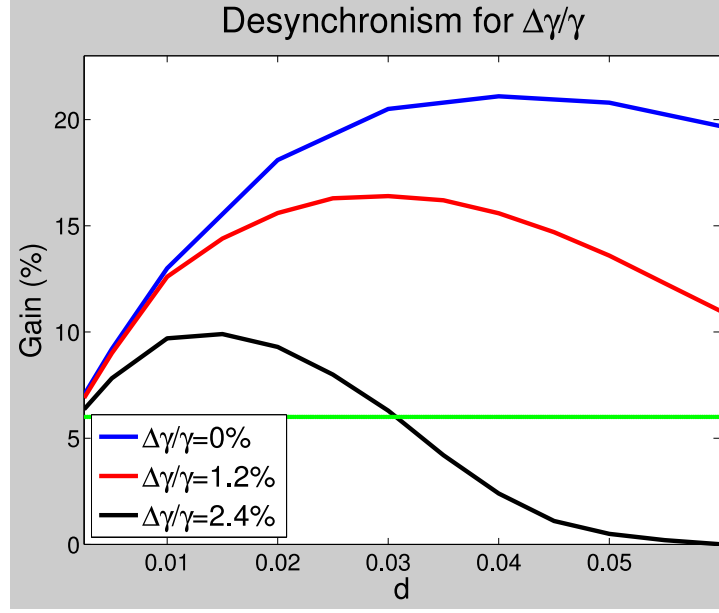


Figure 20. *4DPULSEN* results showing gain vs. dimensionless desynchronism (d) for an energy spread of 0% (blue), 1.2%, (red), and 2.4% (black).

The optimum desynchronism decreases as the energy spread increases. This shift of the optimum desynchronism d corresponds to decrease in the cavity length of $\sim 13 \mu\text{m}$. The *4DPULSEN* code results of only $G \approx 13\%$ for the expected energy spread in Figure 19 will be the assumed value for the experiment will be built around to ensure that the round trip losses are less than the gain.

E. VARYING UNDULATOR GAP HEIGHT

Adjusting the transverse gap height of the undulator changes the peak magnetic field, which alters the FEL resonant wavelength (all other things being equal). This change to longer wavelengths causes the optical mode to expand at a different rate due to diffraction. This diffraction needs to be taken into consideration when designing the optical cavity and beam line, as extensive clipping will cause the round trip losses to be greater than the gain. As the undulator gap width is decreased, the peak magnetic field gets stronger, increasing K , causing the resonance wavelength to increase. In terms of the cavity design this is detrimental for two reasons: as the gap width is decreased, the clipping on the beam pipe inside the undulator increases, and a narrower gap corresponds

to longer wavelength, which leads to more diffraction. A quantitative depiction of this is seen in Figure 21.

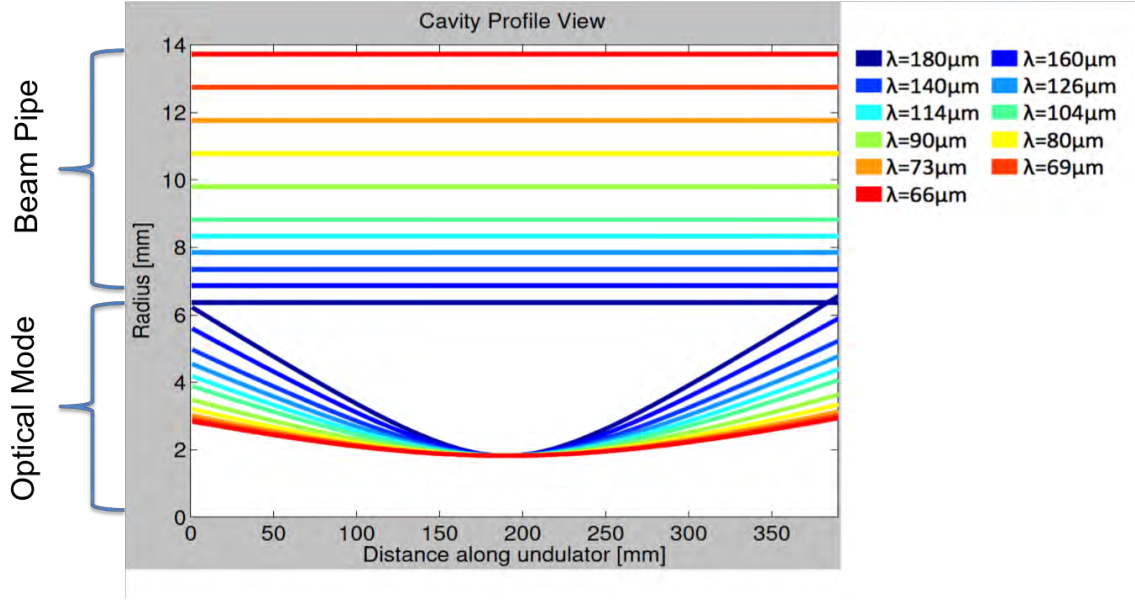


Figure 21. Diffraction of the optical mode compared with undulator gap width.

The straight lines in the top half of Figure 21 depict eleven different values of the beam pipe radius (assumed to be approximately the same as the undulator gap). For each undulator gap, the color scale on the right indicates the corresponding wavelength. The corresponding optical mode for each wavelength is depicted by the curved lines in the lower half of Figure 21, showing the 1/e radius of the Gaussian optical field that is stored inside a concentric optical cavity. The maximum distance along the horizontal axis ~ 390 mm, which is the approximate length of the beam pipe that will be inside of the undulator. In each case, the 1.8 mm optical mode waist radius in the middle of the undulator was held constant, meaning that the radius of curvature of the mirrors would change for each case. Power loss was determined by calculating the power clipped from the Gaussian mode by the inside of the beam pipe at the ends of the undulator. As can be seen, the wide 28 mm gap (red line) gives a short wavelength (66 μm) and aids in keeping the beam pipe far from the optical mode to cause negligible power loss due to clipping. Likewise the narrow gap (purple, 13 mm) results in a longer wavelength (180

μm), which leads to a nearly 24 percent round trip loss in the cavity solely due to clipping on the undulator beam pipe. This does not take into account other possible areas of clipping in the cavity that may also degrade the performance. To maintain a round trip loss of less than one percent on this portion of the beam pipe, the longest wavelength that can be achieved is $\sim 126 \mu\text{m}$ corresponding to a 16 mm gap. As the gap is widened, the losses decrease, but so does the gain, since the decrease in transverse motion of the electrons also lowers the coupling between the electrons and the light. This leads to a total effective range of $\sim 60 \mu\text{m} \rightarrow 126 \mu\text{m}$ when just considering clipping from the undulator beam pipe [35].

F. ELECTRON BEAM RADIUS

To maximize energy transfer, the electron beam and optical mode transverse profiles must properly overlap during the full transit of the undulator. For optimal bunching, gain, and extraction, the electron beam should be well inside of the optical mode. Several examples using *GINGER* are considered in Figure 22.

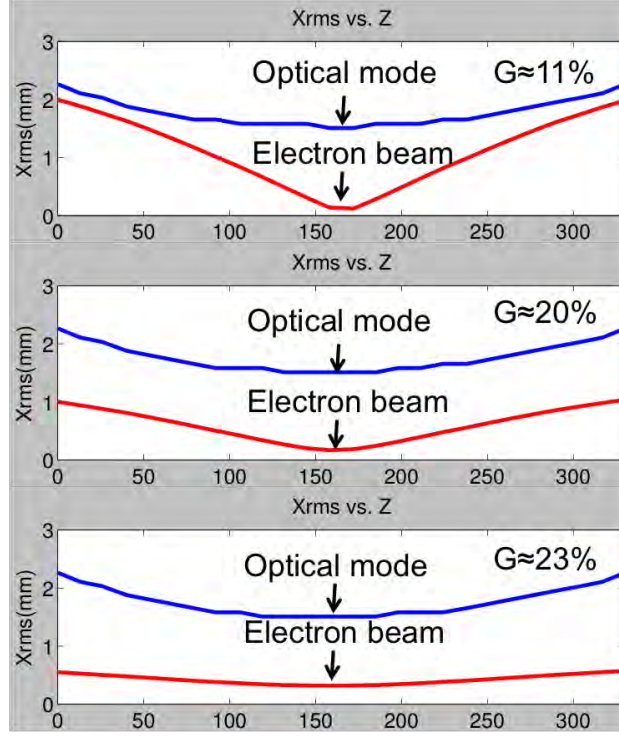


Figure 22. *GINGER* simulations of electron beam (blue) and optical mode (red) transverse profiles for 2 mm, 1 mm, and 0.55 mm initial electron beam radius. The horizontal axis is the distance z along the undulator, the vertical axis is the transverse rms dimension.

Three different initial electron beam radii were simulated to show the effect of electron beam focusing on FEL performance. While focusing the beam aids in maintaining proper overlap inside the optical mode, over focusing can be detrimental. A wider initial electron beam results in many electrons interacting with a portion of the optical field with lower intensities, reducing bunching. Also, a wider initial electron beam requires more focusing which causes a large spread in β_z , thereby inducing a larger spread in initial phase velocities, thus inhibiting the bunching mechanism. In the top graph in Figure 22, the electron beam's initial radius (blue) is 2 mm and produces a weak field gain of $G \approx 11\%$. In the middle graph the electron beam's initial radius is 1 mm, which leads to an increased $G \approx 20\%$. The bottom graph is the nominal case that is being discussed in this thesis with an initial electron beam radius of 0.55 mm at the beginning of the undulator, which leads to $G \approx 22\%$.

As the electron beam decreases in radius, it overlaps the portion of the optical mode with higher peak fields. This increases the FEL interaction and the bunching mechanism, thereby improving the performance. Figure 23 shows simulation results for the gain for an initial 2 mm radius (first case in Figure 22) using *GINGER*. The simulation was started with an initial field that roughly corresponds to spontaneous emission. For the first few hundred passes the simulation shows a noisy result for the gain but settles down to $\sim 10\%$ gain for the next few hundred passes. After ~ 500 passes, the gain decreases due to saturation at high power. When the gain is equal to the round trip losses in the cavity the FEL has reached steady-state saturation.

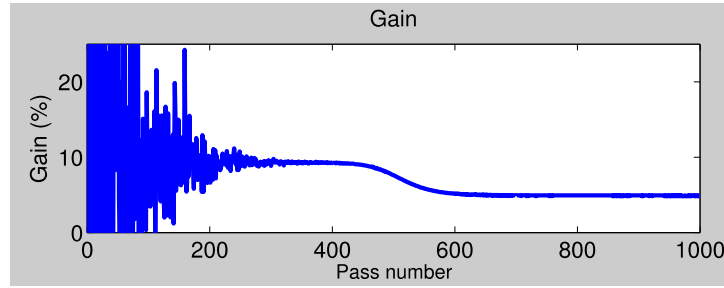


Figure 23. *GINGER* gain as a function of pass number for 2 mm initial electron beam radius.

Figure 24 shows simulation results for the gain for an initial 1 mm radius corresponding to the second case in Figure 22.

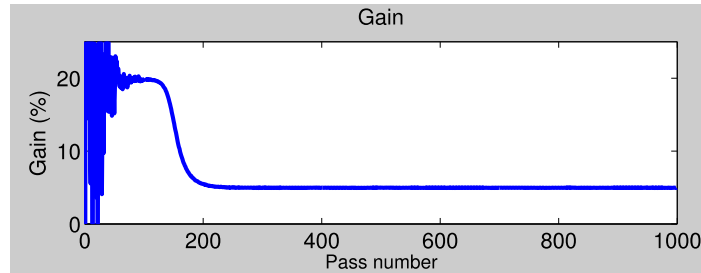


Figure 24. *GINGER* gain as a function of pass number for 1 mm initial electron beam radius.

For the 1 mm initial radius case, saturation is reached at ~ 200 passes due to the larger $\sim 20\%$ weak field gain caused by the better overlap between the electron beam and the optical mode. The 0.55 mm initial radius case has even higher gain and therefore reaches saturation after only 100 passes. This is the expected result in the experiment.

G. OPTICAL MODE SHAPE

The hole out-coupling technique that is designed for the optical cavity of the Niowave FEL can have a negative effect of distorting the transverse shape of the optical mode. Transferring energy away from the fundamental mode can decrease the coupling between the optical mode and the electron beam, reducing the FEL gain. The size of the hole needs to be small enough so the round-trip losses do not exceed the weak field gain and the wavefronts are not distorted so much that the FEL efficiency decreases significantly. However, smaller holes produce larger diffraction when the light exits the cavity, which must also be considered. Figure 25 shows the transverse electric field profiles at the undulator entrance for a range of hole out-coupling radii from 0 mm to 4 mm in the center of the outcoupling mirror.

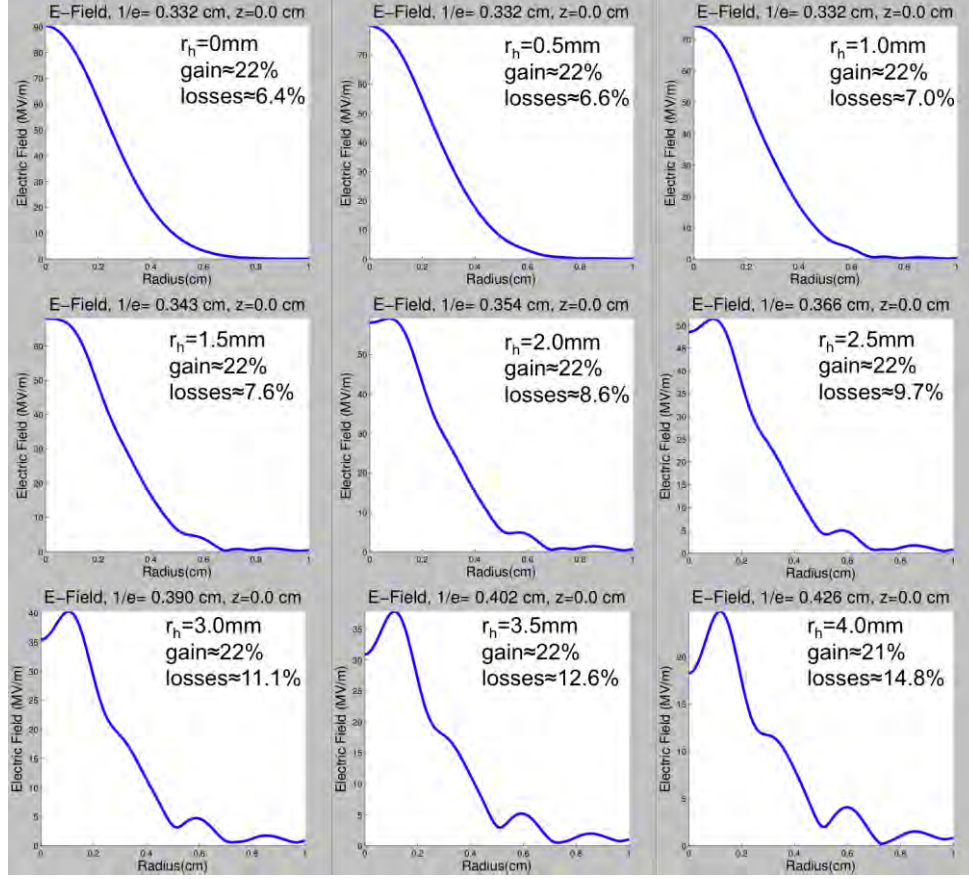


Figure 25. *GINGER* simulation results for transverse electric field at undulator exit for increasing hole radii.

Figure 25 depicts the transverse electric field at the undulator entrance for a range of output coupler hole sizes. The side lobes at larger radii (lower right in Figure 25) are due to the energy that is transferred to the higher order modes. Losses and gain are calculated in the weak field regime. The wavelength that was simulated was the nominal $\sim 100 \mu\text{m}$ for this FEL leading to a radius of $\sim 27 \text{ mm}$ ($1/e$ in the field) on the mirror. The amount of gain degradation due to the enlarged hole size is nearly negligible as the gain only drops $\sim 1\%$ at the largest radius, but the cavity losses are large ($\sim 15\%$). Reiterating, *GINGER* simulations do not include pulse effect so the actual gain will be lower and could be below this loss for the large hole radii. For this design a hold radius of 0.5 mm will be initially used because it maintains low losses. After initial operation, the hole radius can be enlarged to increase THz output.

H. AVERAGE OUTPUT POWER

At saturation, the amount of power that is lost by the electron beam is equal to the output power of the FEL. The extraction, which is the fraction of the electron beam power converted to light, can be estimated by $1/2N \sim 5\%$ for $N=10$ [30]. Because of the slippage of the short optical and electron pulses, this should be considered an overestimate. All the codes used have shown an extraction of $\sim 3\text{-}4\%$, which corresponds to an ~ 2 kW average output power.

I. OPTICAL CAVITY ALIGNMENT TOLERANCES

Ideally the optical cavity is aligned sufficiently collinear with both the axis of the undulator and the trajectory of the electron beam. In this section, the tolerance on the optical cavity alignment will be determined by simulating the FEL interaction with either a transverse shift or angular tilt of one mirror. Either of these will cause a misalignment of the electron beam and the optical mode, leading to decreased interaction length between the electrons and the optical mode, thus lowering the gain. *GINGER* was not utilized for these simulations because it presumes an axisymmetric radiation field. Rather, simulations were done using *4DPULSEN* to discern the effect of both the transverse shift and angular tilt offsets (see Figures 26 and 27).

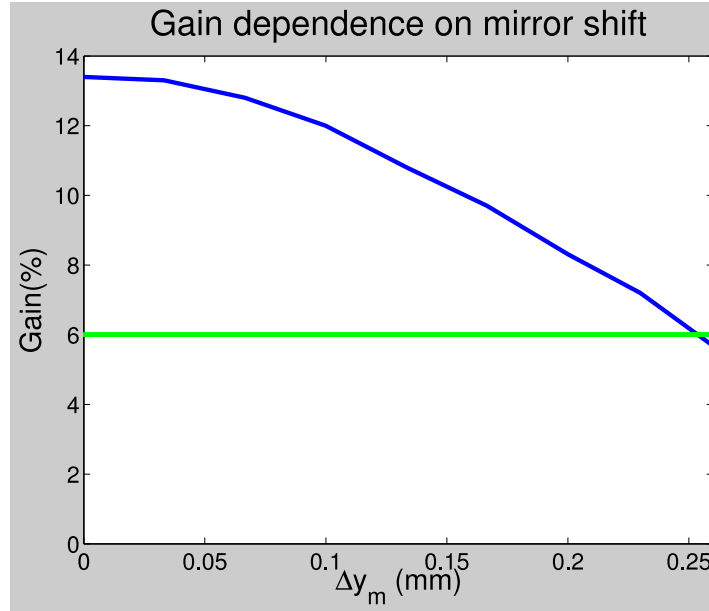


Figure 26. *4DPULSEN* simulation results for weak field gain as a function of shift of one of the cavity mirrors.

Figure 26 shows the gain plotted against the transverse mirror offset, where the green line indicates the minimum gain threshold of six percent round trip loss in the cavity. As the mirror shift increases, the gain degrades until, at ~ 0.25 mm offset, the gain is below threshold and the FEL will not work.

This same analysis is done for the angular tilt and can be seen in Figure 27.



Figure 27. *4DPULSEN* simulations of weak field gain as a function of tilt of one of the cavity mirrors.

As the mirror is misaligned by an angle of $0 \rightarrow 0.15$ mrad, the gain decreases from its maximum value of $\sim 13\%$ to approximately threshold. This gives a value of initial alignment that must be met by the alignment technique.

As before, for each of the data points in the Figure 27 and 26, the amount of desynchronism has been optimized to maximize the gain. The change in desynchronism as a function of misalignment can be seen in Figure 28.

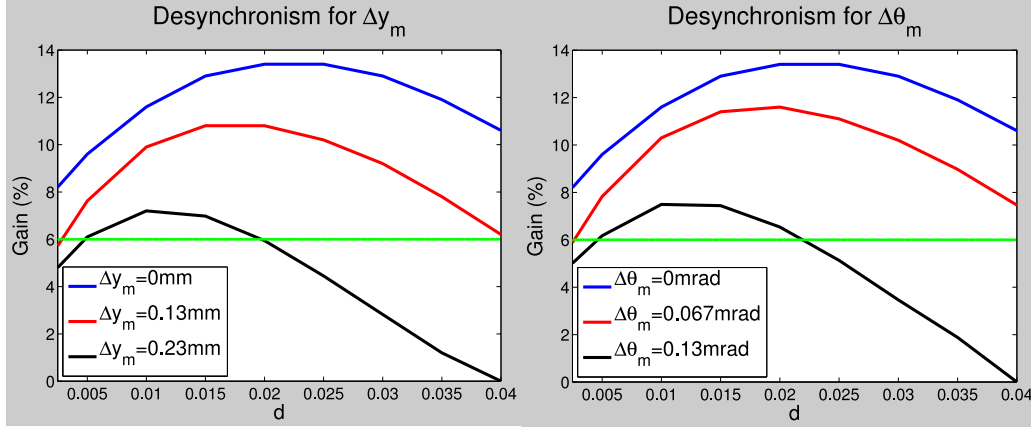


Figure 28. The desynchronism curves for different mirror shifts (on left) and mirror tilts (on right).

As the cavity mirror is misaligned, the maximum gain decreases and occurs at a smaller desynchronism. For no mirror shift (left in Figure 28) $\Delta y_m = 0.0$ mm (blue), the peak gain occurs at $d = 0.02$ whereas for $\Delta y_m = 0.23$ mm (black) the peak is at $d = 0.01$. For no mirror tilt (right in Figure 28), $\Delta \theta_m = 0.0$ mrad (blue), the maximum gain is at $d = 0.02$, whereas for the $\Delta \theta_m = 0.13$ mrad the peak occurs at $d = 0.01$. This change in d (from 0.01 to 0.02) corresponds to a $4.5 \mu\text{m}$ shift in the cavity length. Knowing the mirror shift and tilt tolerances enables the engineering design of an alignment procedure, which will be described in a later chapter.

THIS PAGE INTENTIONALLY LEFT BLANK

IV. ELECTRON BEAM PHYSICS

A. ELECTRON BEAM QUALITY

The electron beam is made up microbunches of free electrons that are co-propagating with each other. Each electron has a position \vec{r} and a velocity $\dot{\vec{r}}$ with respect to the beam centroid, which describes its position and momentum. In the lab reference frame, the values of $\dot{\vec{r}}$ are seen as a distribution of angles with respect to the propagation vector of the beam centroid.

1. Transverse Emittance

Emittance is defined as the area of the electron beam in phase space and is given by $\varepsilon = \sigma_r \sigma_\theta$, where σ_r is the rms transverse spread in positions and σ_θ is the rms spread in angles from the propagation direction. Rather than looking at the particles in position space (where there 3 dimensional location is considered), it is often better to analyze the beam in phase space, or where a particles momentum and position are compared. A typical phase space diagram can be seen in Figure 29.

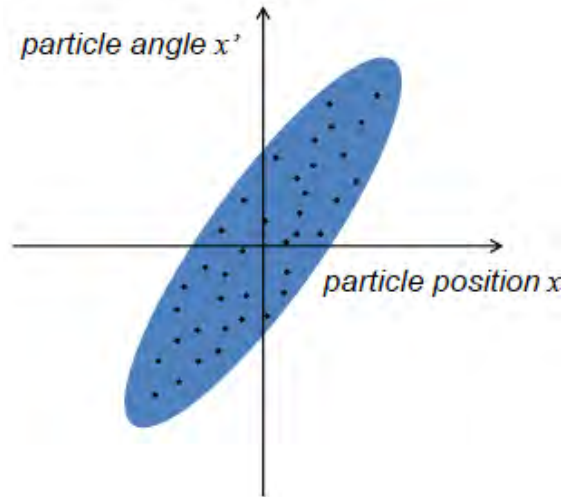


Figure 29. Typical phase space diagram of electron bunch where x is the particles transverse position x' is the particles momentum in that direction, from [36].

In Figure 29 the electron bunch has a spread in both angles and positions (in the x - x' plane). By Liouville's theorem, the volume in phase space is constant in the bunch frame. Emittance is often measured at low energies, but at the undulator entrance (where the necessary beam quality is usually defined), the electron beam is at a much higher energy. Due to relativistic effects, the emittance is dependent on the speed of the electrons. The normalized emittance, $\varepsilon_n = \beta\gamma\sigma_r\sigma_\theta$, removes the dependence on the velocity and supplies a measure of beam quality that is constant throughout a whole beam line (as long as the number of particles lost is inconsequential).

The phase space volume remains constant as an electron bunch transits a beam line but may change shape. A typical beam line component is a magnet to supply focusing to the electron beam. Figure 30 depicts the evolution of the phase space as a beam is focused (in the x transverse plane) through a waist.

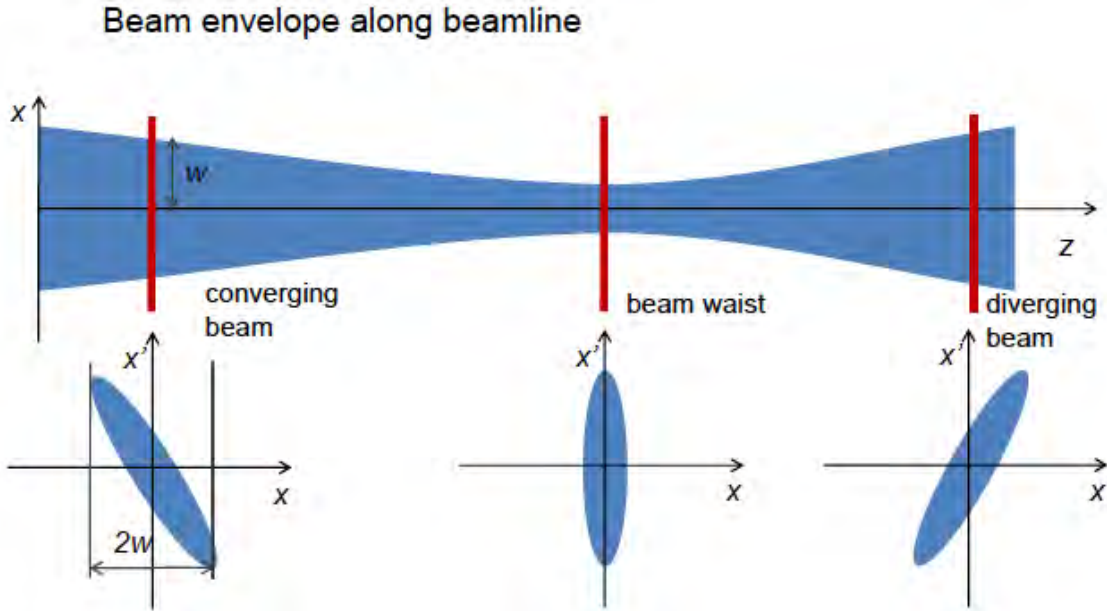


Figure 30. Electron beam phase space evolution as it passes through a beam waist, from [36].

In the left side of Figure 30, the beam is converging towards the waist. This can be seen in the phase space diagram in the lower left, where electrons with negative positions ($x < 0$) have positive angles ($x' > 0$) and the electrons with positive positions have negative

angles. As the beam propagates to the waist, angular spread remains constant while the maximum radius decreases; this induces an effective shear on the phase space area. At the waist, the radius is at a minimum, as can be seen by the reduced transverse extent of the phase space diagram in the center of the figure. But, the beam has both positive and negative angles. As the beam expands beyond the waist, the electrons with positive positions ($x > 0$) now have positive angles ($x' > 0$), and those with negative positions have negative angles, increasing the transverse size of the electron beam. By Liouville's theorem the area remains constant. A large emittance, or large area in phase space, inhibits the ability to focus the beam to a small radius.

For the FEL to work optimally, the electron beam should be well inside the optical mode along the length of the undulator. This places geometrical constraints on the electron beam waist radius and angular spread, and therefore the emittance. Applying these concepts leads to a characteristic emittance $\varepsilon_c \approx \gamma\lambda/4\pi$ above which weak field gain is diminished [37]. For the Niowave FEL parameters, $\varepsilon_c \approx 135$ mm-mrad and is several times larger than the nominal 28 mm-mrad used in the simulations. The simulation code *4DPULSEN* confirms that an emittance $\varepsilon_n = 100$ mm-mrad decreases weak field gain from approximately 14 percent down to approximately 10 percent and the FEL fails to operate when emittance is increased to approximately 200 mm-mrad.

2. Energy Spread

During the generation and acceleration of the electron beam, different electrons will gain different amounts of kinetic energy due to entering the accelerating structures at slightly different RF phases. In addition to affecting FEL performance (as was previously described in Chapter III), this energy spread can cause problems with beam transport. As magnetic fields along the beam line are used to bend and focus the electrons, a spread in energy leads to individual electrons being affected differently, since the magnetic force depends on their energy. These effects and their mitigation will be discussed in later sections.

3. Desired Electron Beam Quality

The electron beam quality requirements for the Niowave THz FEL are relatively lax due to the long wavelength of the FEL and the short undulator. The longer wavelength allows for a larger energy spread as bunching on the order of a wavelength of light is easier. A shorter undulator increases the gain spectrum bandwidth, $\sim 1/N$, so the FEL has less sensitivity to energy spread from the accelerator. Also, with such a short undulator, a beam with a large emittance can still be focused properly through it without scraping on the beam pipe. The electron beam delivered to the undulator must be matched to fit inside the optical mode to supply proper overlap along the undulator, as was described in the Chapter III. Simulation results indicate that the Niowave FEL can tolerate a large transverse emittance of ~ 100 mm-mrad with up to $\sim 1.7\%$ energy spread. For the nominal emittance value of 28 mm-mrad, an energy spread up to three percent is tolerable.

B. FOCUSING: QUADRUPOLE MAGNETS

In order to focus the electron beam, quadrupole magnet is formed by four hyperbolic pole face electromagnets arranged symmetrically around the beam pipe with alternating polarity magnets. A depiction of the arrangement can be seen in Figure 31.

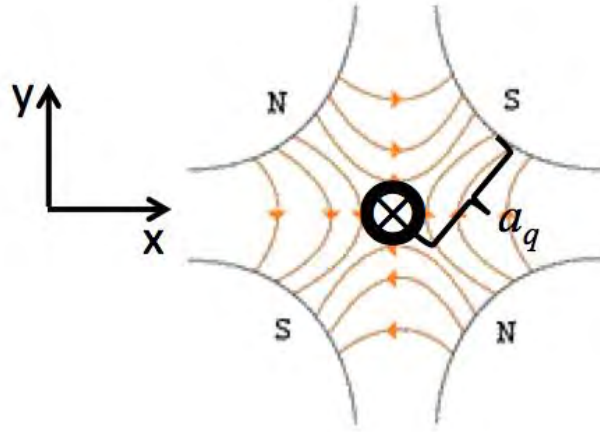


Figure 31. Depiction of magnetic field of quadrupole magnet, after [38].

The magnets are placed axially around the beam line creating a magnetic field at the site of the quadrupole of the form

$$B_x = B_q \frac{y}{a_q}, \quad \text{Eq. 4.1}$$

$$B_y = B_q \frac{x}{a_q}, \quad \text{Eq. 4.2}$$

where B_q is the peak magnetic field next to the pole face, and (x,y) are measured from the axis, and a_q is the distance from the center axis to the magnet face. The strength of the focusing is controlled by the combination of the interaction length of the quadrupole as well as the peak magnetic field. In Figure 31, the electron beam is going into the page, so this magnet would supply focusing in the y direction and defocusing in the x direction. Due to the focusing / defocusing nature of quadrupole magnets, they are commonly placed in groupings of two or three magnets to supply the necessary focusing in both planes. One example of a quadrupole “triplet” can be seen in Figure 32.



Figure 32. Quadrupole triplet for transverse beam focusing, from [23].

The strength of the magnets and the size of the drift space between quadrupoles must be optimized to supply the necessary focusing for the beam at the designed focal point later in the beam line. With each quadrupole acting as a lens with focal lengths f_1, f_2, f_3 , respectively, it can easily be shown that the focal length of three quadrupoles in series is

$$f_t = \frac{f_1 f_2 f_3}{f_3(f_2 + f_1 - s_1) + f_1 f_2 + s_2 f_2 + s_2 f_1 - s_1 s_2}, \quad \text{Eq. 4.3}$$

where s_1 and s_2 are the drift spaces between subsequent quadrupoles [39]. These quadrupoles will be used to help focus the electron beam into the undulator of the FEL to create the correct overlap between the optical mode and the electron beam and create the minimum radius needed.

C. BENDING: DIPOLE MAGNET DESIGN

A dipole magnet supplies a constant magnetic field across the beam path to bend the electron beam.

1. Dipole Design

One design of a dipole magnet consists of an iron yoke wrapped with coils of wire; when current is applied through the coils it produces an approximate uniform magnetic field across a gap. The size and shape of the iron yoke controls the length, width, and gap size of the dipole. The current through the wire controls the magnetic field strength and polarity. The magnetic field is enhanced by the permeability of the iron yoke [40].

A cross section of two typical electromagnetic dipoles can be seen in Figure 33.

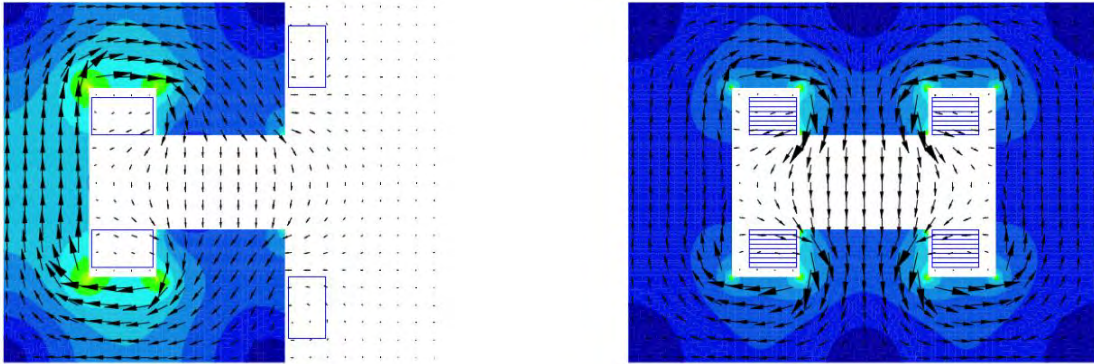


Figure 33. Cross-sectional view of dipole magnets, from [41].

On the left is a “C-core” magnet that has one open side of iron; on the right is a “H-type” yoke, which is symmetrical about the center axis. The coils of wire are denoted by the boxes surrounding the solid yokes and the magnetic field directions and magnitudes are given by the direction and size of the arrows. Inside the yokes, the color denotes the magnetic field strength.

2. Simple Dipole Physics

The geometry of the interaction between an electron and a uniform magnetic field can be seen in Figure 34.

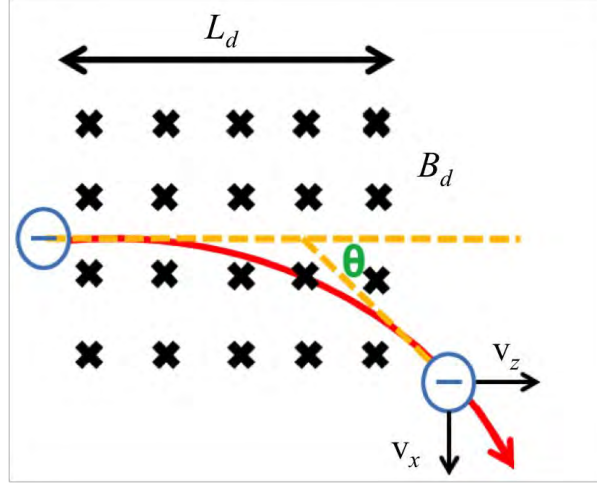


Figure 34. Depiction of electrons motion through a uniform magnetic field, after [42].

The electron enters from the left where it begins to interact with a uniform magnetic field of magnitude B_d (into the page) for a length L_d . The relativistic Lorentz force alter the electron's trajectory by an angle θ . The relativistic Lorentz force is

$$\frac{d}{dt}(\gamma m \vec{v}) = -e \vec{v} \times \vec{B}_d, \quad \text{Eq. 4.4}$$

leading to

$$\frac{dv_x}{dt} \hat{x} + \frac{dv_z}{dt} \hat{z} = \frac{eB_d}{\gamma m} (v_z \hat{x} - v_x \hat{z}). \quad \text{Eq. 4.5}$$

Differentiating again with respect to time gives

$$\frac{d^2 v_x}{dt^2} \hat{x} + \frac{d^2 v_z}{dt^2} \hat{z} = -\left(\frac{eB_d}{\gamma m}\right)^2 (v_x \hat{x} - v_z \hat{z}), \quad \text{Eq. 4.6}$$

which can be separated into two differential equations, each in the form of a simple harmonic oscillator with frequency $\omega_d = eB_d/\gamma m$. The solution can thus be written

$$v_x = -\beta c \sin(\omega_d t), \quad \text{Eq. 4.7}$$

$$v_z = \beta c \cos(\omega_d t), \quad \text{Eq. 4.8}$$

where the initial conditions are $v_{zo} = \beta c$, $v_{xo} = 0$. The deflection angle is given by $\tan(\theta) = v_x/v_y = \tan(\omega_d t)$, leading to

$$\theta = \omega_d t = \frac{eB_d}{\gamma m} t. \quad \text{Eq. 4.9}$$

The deflection angle depends on the strength of the magnetic field (B_d), the electron's kinetic energy (γ) and the time (t) spent in the field (i.e., the length of the dipole). While the energy of the electron is set by the design of the particle accelerator, the length of the dipole and the strength of the magnetic field must be controlled to induce the proper change in trajectory.

3. Fringe Fields

The entire derivation leading to Eq. 4.9 is based on an idealistic uniform rectangular magnetic field with “hard edges.” Realistically, dipoles have fringe fields that extend past the edges of the magnets into the surrounding area. These can be seen in Figure 33 on both types of magnets. This effectively increases the dipole length resulting in an increased deflection angle. This effect must be taken into account when designing the strength of the magnet.

4. Energy Spread

A realistic beam is comprised of billions of electrons with spreads in position, angle, and energy. An electron's position and angle with respect to the beam centroid will be translated through the dipole without affecting the beam's properties, but the energy spread in the electron beam will cause an enlarged spread in angles after the dipole since the energy of an electron affects its deflection angle according to Eq. 4.9. An example of this spread can be seen in Figure 35.

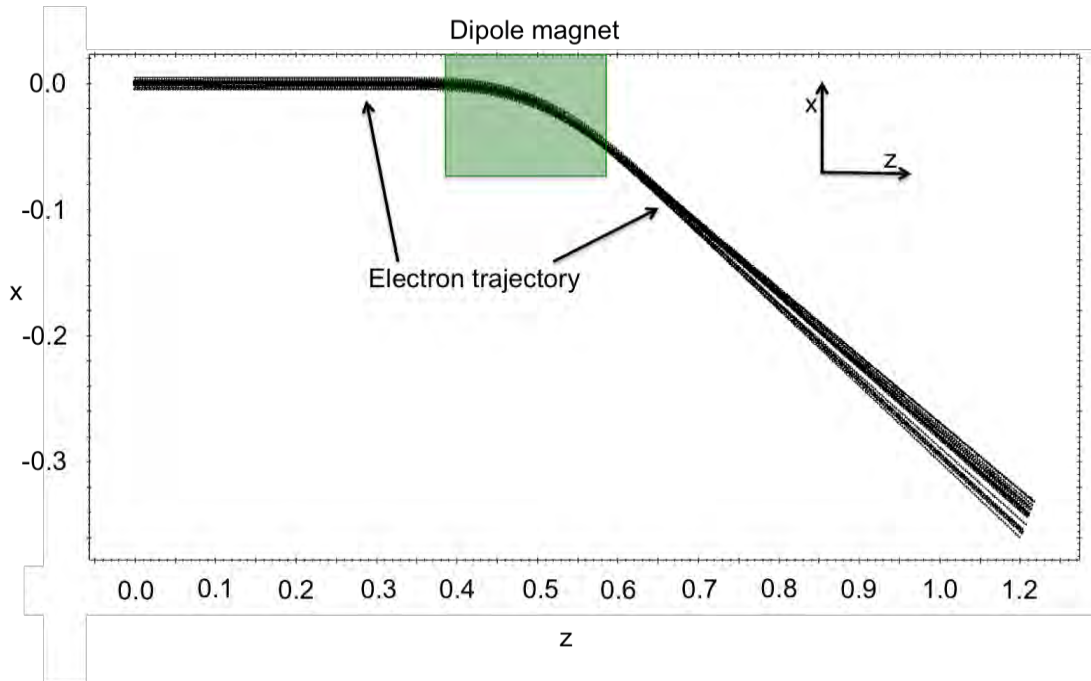


Figure 35. Electron beam dispersion from a dipole magnet due to energy spread.

Figure 35 depicts a 2 mm radius, 8 MeV electron beam with a $\sim 1.7\%$ percent energy spread entering the dipole (green) from the left. After the dipole the electron trajectories are altered, but due to the enlarged spread in angles the transverse size of the beam grows. This can be a problem when trying to focus the electron beam inside the undulator.

D. COMBINED FUNCTION MAGNETS

Some magnets can combine multiple functions (i.e., focusing and bending) by virtue of their shape. In the case of the Niowave THz FEL, a single magnet can be used to bend the electron beam while controlling the dispersion caused by the energy spread. Two techniques can be used to control the angular deflection of electrons as they pass through a magnet: either the time the electron interacts with the magnetic field can be preferentially changed, or the strength of the magnetic field can be altered in such a manner that different energy electrons will interact with different magnitude magnetic fields.

1. Tilted End Faces

To alter the interaction length the individual electrons have with the magnetic field, the shape of the magnetic field region needs to be adjusted from the simple rectangular area that was previously considered (see Figure 36).

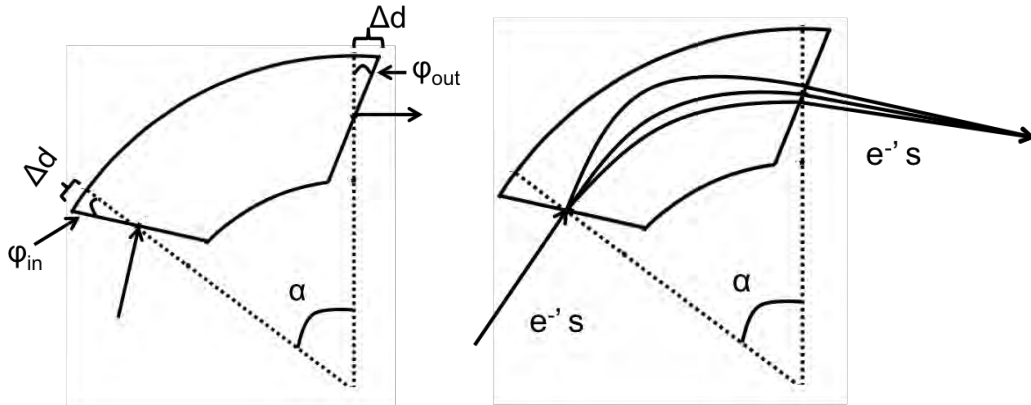


Figure 36. Dipole magnet with rotated pole faces.

For example, Figure 36 depicts a top view of a dipole magnet designed to alter the trajectory of an electron beam by an angle α . In this geometry the nominal end face directions (dotted line) are orthogonal to the propagation direction of the electron beam. In both the left and right diagram the entrance and exit faces of the magnet are tilted from this nominal end face by an amount ϕ_{in} and ϕ_{out} , respectively. When an electron beam enters the dipole, the higher energy electrons will be less affected by the magnetic field and will tend to go towards the outside of the curve. To compensate for this, the end faces are tilted in such a manner so that the higher energy electrons will interact with the dipole longer than the lower energy electrons. This supplies a transverse focusing ability to the dipole and will both bend the electron beam as well as focusing it in the plane of the turn, counteracting the dispersion.

2. Canted Pole Faces

Another method to preferentially control the angular deflection of the individual electrons is to cant the transverse pole faces. This involves turning the pole faces of the

magnets, which are normally parallel to each other, thus adding a transverse dependence to the strength of the magnetic field, as seen in Figure 37.

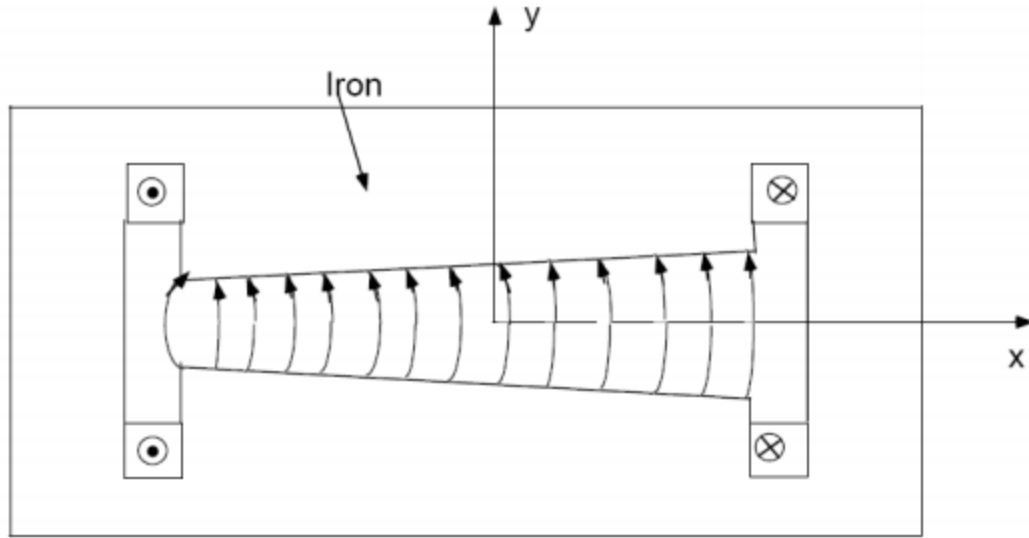


Figure 37. End view of canted dipole, from [43].

The end view of a canted dipole in Figure 37 shows the angle of the pole faces with respect to the direction of travel. Much like the tilted end face design, this magnet preferentially induces more, or less, force on an electron depending on its energy. Rather than altering the amount of time the electron travels through the dipole based on its energy, this magnet alters the strength of the magnetic field to adjust the output angle accordingly.

E. NIOWAVE BEAMLINE GEOMETRY

The electron beam needs to be transported from the final accelerating structure of the linac to the undulator and must be focused in the correct manner necessary for the FEL to work. The geometry of the Niowave beamline after the linac can be seen in Figure 38.

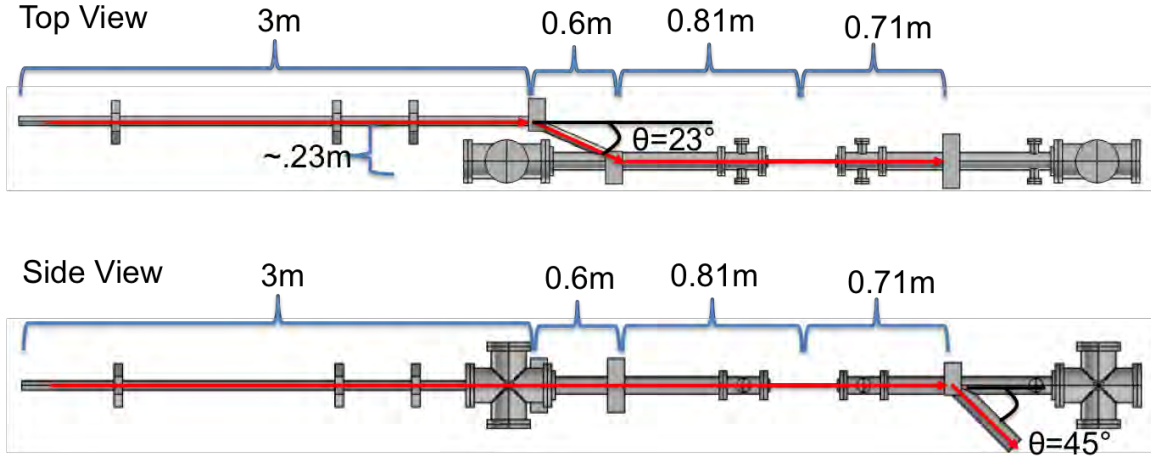


Figure 38. Side and top profile view of Niowave beamline.

The electron beam enters from the left and transits three meters of beam pipes before turning through two horizontal 23° bends (one $+23^\circ$ and the other -23°) to be injected into the undulator. After transiting through the undulator, it then goes through a vertical 45° bend downward towards the ground, where the electrons are sent into a beam dump. In the middle of the undulator, the electron beam must be focused to a nominal 0.45mm waist radius ($y_{\text{rms}} \approx x_{\text{rms}} \approx 0.32 \text{ mm}$). To accomplish this, both quadrupole and dipole magnets will be utilized.

F. BEAMLINE MODELING: GENERAL PARTICLE TRACER

A beamline model can be used to design the necessary components to deliver an electron beam to the undulator with the proper qualities.

1. Code Description

A commercial particle tracking code is used to design the beamline and quantify the parameters of the beamline components. General Particle Tracer is a complete software package produced by Pulsar Physics to study charged particle dynamics in electromagnetic fields [44]. An input file describes the beamline components' positions and strengths, the electron beam's initial properties (energy spread, position spread, emittance, etc...), as well as the diagnostic locations along the beamline (and what

information is to be outputted). It maps out the entire three-dimensional electromagnetic field and then, using a fifth order Runge-Kutta method, calculates the individual particle trajectories through the beam line.

2. Optimization with Only Quadrupoles

To supply the necessary focusing to the electron beam, a set of three quadrupole magnets are utilized. As seen in Figure 38, the distance from the start of the simulation at the linac exit ($z=0$) to the middle of the undulator is ~ 4.4 m. The quadrupole triplet will be placed before the first dipole. GPT contains built in functions to optimize parameters to focus both transverse directions to the necessary spot size and location by comparing various quadrupole strengths and positions. The electron beam parameters that were simulated are listed in Table 5.

Beam kinetic energy	8 MeV
Initial electron beam radius ($x_{\text{rms}}, y_{\text{rms}}$)	2 mm
Normalized emittance, rms	28 mm-mrad
Energy spread ($\Delta\gamma/\gamma$)	1.66%

Table 5. GPT simulation parameters.

This resultant profile from optimizing the quadrupole parameters to focus in the middle of the undulator can be seen in Figure 39.

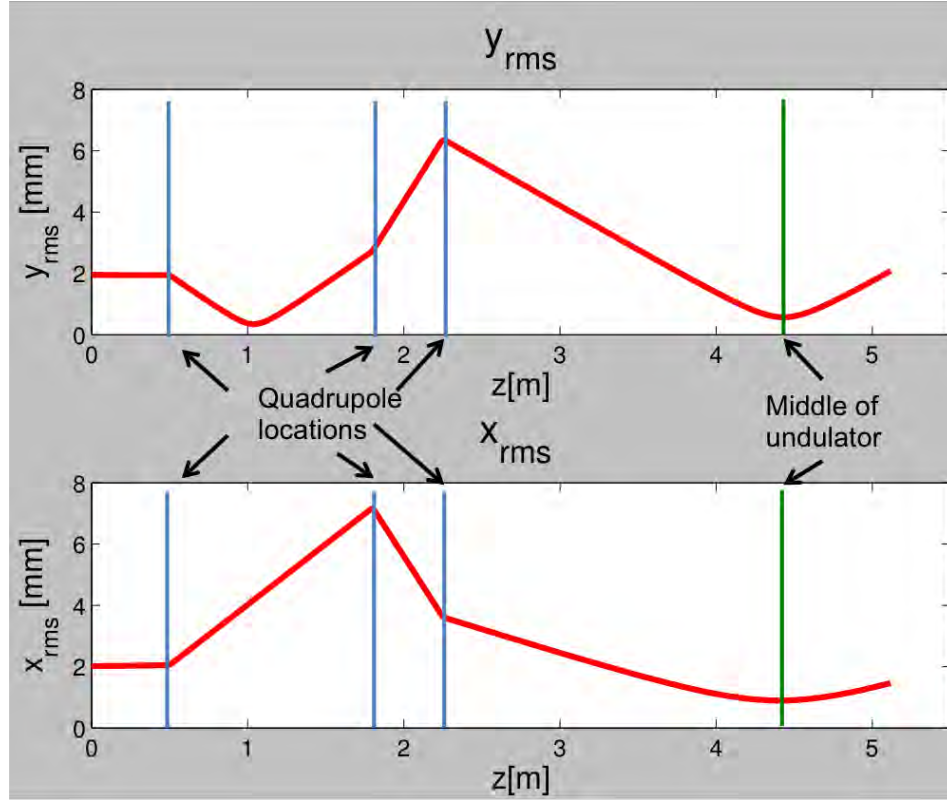


Figure 39. Electron beam radius (rms) through beamline.

A reasonable assumption for the electron beam's initial radius after the linac is taken to be 2 mm. For this simulation GPT was tasked with minimizing the beam radius in both transverse directions at $z \approx 4.4$ m by adjusting quadrupole parameters. The quadrupole parameters that produced this result are listed in Table 6.

1 st quadrupole location	0.5 m
1 st quadrupole peak magnetic field gradient	1.72 T/m
2 nd quadrupole location	1.8 m
2 nd quadrupole peak magnetic field gradient	-1.57 T/m
3 rd quadrupole location	2.25 m
3 rd quadrupole peak magnetic field gradient	1.64 T/m

Table 6. Optimized quadrupole parameters with the distances measured from the end of the linac.

These parameters lead to a beam size of 0.88 mm and 0.57 mm in the x and y direction respectively at 4.4 m. Both are larger than the ~ 0.32 mm mentioned previously but are smaller than the 1.3 mm optical mode (components). As long as the electron beam is well inside the optical mode, the FEL interaction works as desired. The quadrupoles were assumed to have a length of 3 cm, which is a reasonable assumption [45]. GPT does not include fringe field effects in the quadrupole magnets so the actual peak magnetic field would be slightly less than listed in Table 6.

3. Combining Quadrupoles and Rectangular Dipole Magnets

Adding the two dipoles, which are needed to bend the electron beam around the cavity mirrors, will cause a decrease in focusing in the x-plane due to dispersion. The two dipoles are separated by ~ 54 cm and the magnetic fields will need to be equal strength but opposite polarity to supply the ~ 0.23 m offset without altering the final propagation direction into the undulator. The dipoles were assumed to be 20 cm long which is a reasonable design given the low energy of the electrons. Without the addition of fringe field effects the necessary magnetic field strength can be calculated from Eq. 4.7 and is equal to ~ 0.056 Tesla. Adding the two dipoles leads to the beam path seen in Figure 40 from GPT.

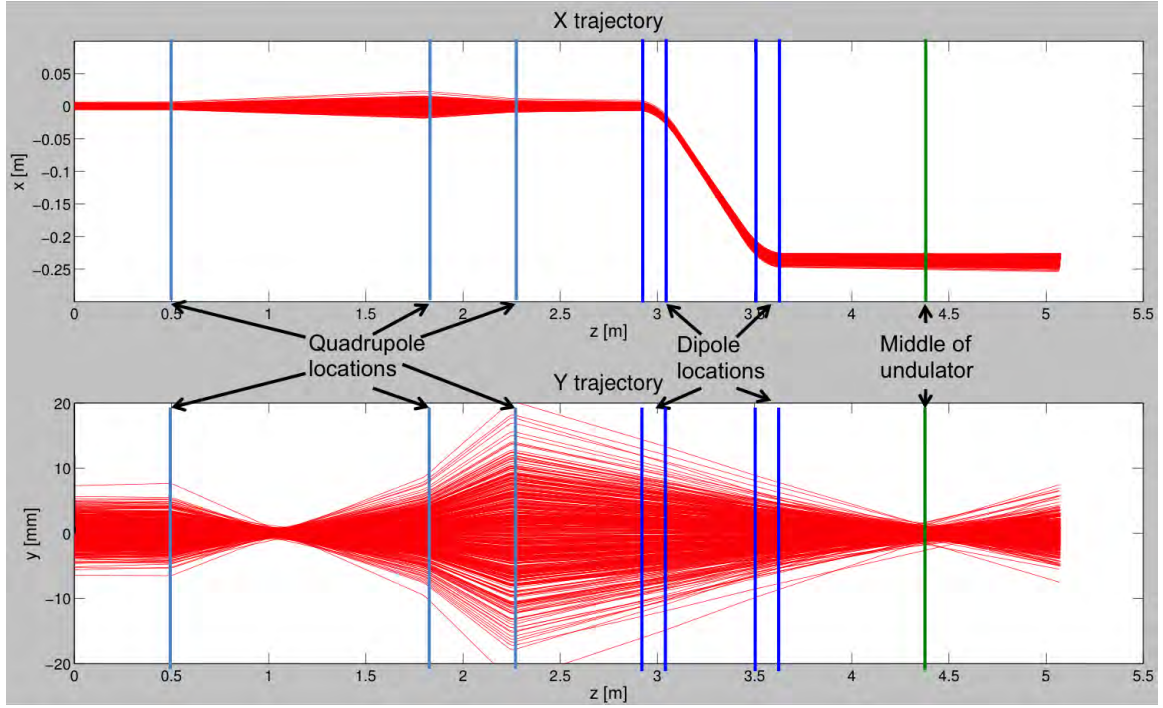


Figure 40. Electron beam trajectory in x (top) and y (bottom) plane.

This dipole chicane supplies the required translational offset but the dispersion leads to a beam size of ~ 4 mm by ~ 0.55 mm in the x and y directions respectively. Note that the transverse size in y is not altered by the dipoles, as expected. This would cause approximately half of the electron beam to be outside the optical mode inside the undulator, which would severely degrade FEL performance. The effect the dipole has can be seen in a graph of the electron beam's radius in the x direction in Figure 41.

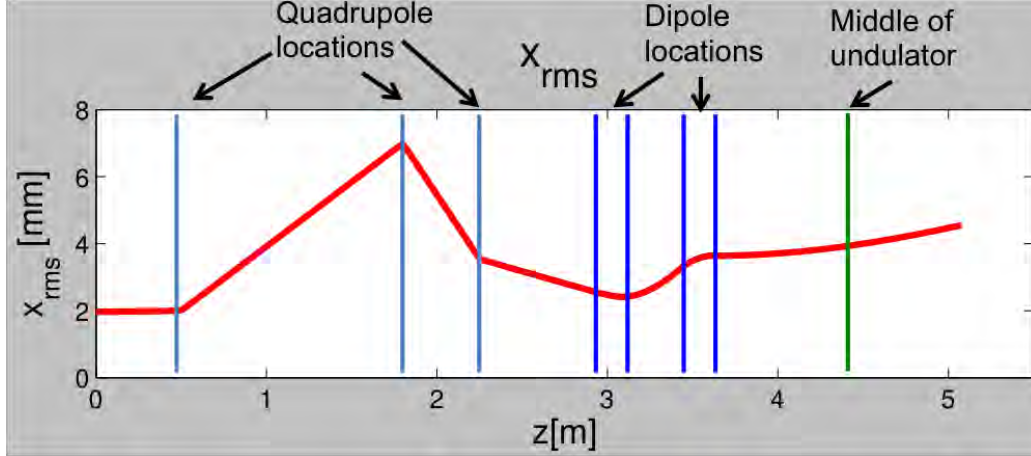


Figure 41. Transverse electron beam size along beam path.

The electron beam size follows the same trend as seen in Figure 39 until the third meter, where the radius starts to increase due to the dipole dispersion. As the beam transits the second dipole, the opposite polarity field induces another spread in deflection angles, but this one is equal and opposite of the first cancelling out the spread in angles. It is in the drift space between the two dipoles that the electron beam's transverse size is increased. Due to this, the distance was minimized for the given angle and geometry.

4. Quadrupoles and Combination Magnets

As was described in section D.2, the use of combination magnets can be used to counteract the dispersion created by the dipole. For this type of magnet, the nominal length of the dipole and the necessary bending angle describes the radius of curvature. GPT contains a built in model of this type of magnet; the geometry can be seen in Figure 42.

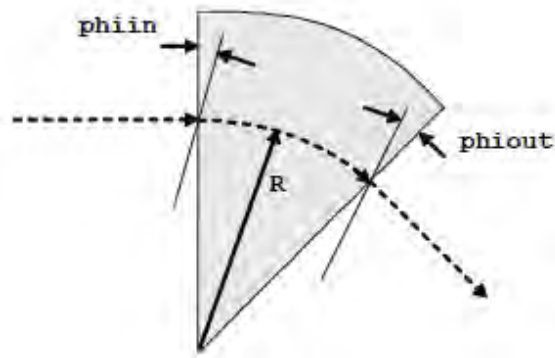


Figure 42. Geometry of combination magnet, from [44].

In Figure 42, the electron beam enters from the left, interacts with the magnetic field and is turned through a circle of radius R before exiting to the right. Nominally the pole faces are orthogonal to the incident electron beam direction and the exiting electron beam direction. To supply the necessary focusing these pole faces can be rotated to alter the path length for different energy electrons undergo. By altering this angle while keeping the dipole placement the same as before leads to a properly focused beam through the undulator. The resulting particle trajectories can be seen in Figure 43.

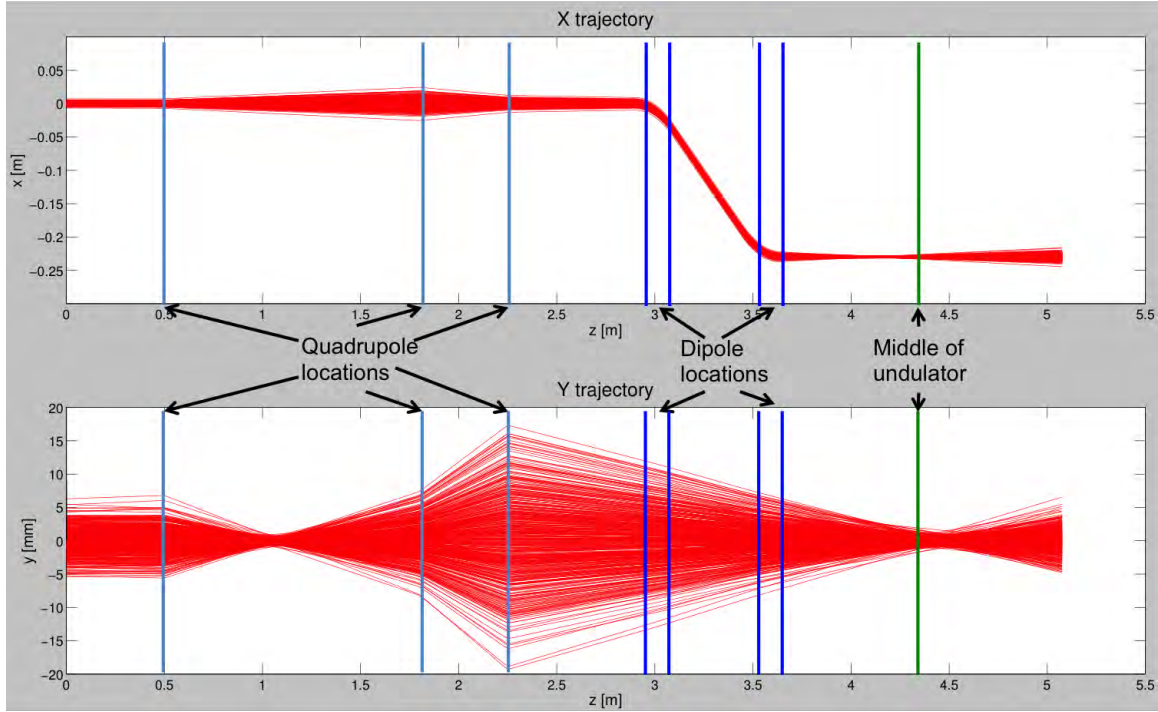


Figure 43. Electron beam trajectories in x (top) and y (bottom) plane using combination magnets.

The addition of the combination magnets allows the electron to be focused in the x-plane into the undulator. To minimize the electron beam radius in the middle of the undulator in this case required that both end faces of the first dipole be turned 15° and the end faces of the second dipole rotated -10° (as described in Figure 42). The nominal length of the dipole is still 20 cm leading to the same magnetic field strength of ~ 0.056 Tesla that was calculated for the rectangular dipole magnets. Fringe fields were not considered in this case so a slightly reduced magnetic field would be needed to produce the necessary bending angle. With this combination a beam size of ~ 1 mm and ~ 0.55 mm in both x and y directions is achieved in the middle of the undulator. While this is greater than the initial design goal, it is well inside the 1.8 mm optical mode radius that is designed for the optical cavity, and the FEL interaction will work as designed.

After the FEL interaction, the electron beam will have a drastically increased induced energy spread due to the relatively high extraction in the FEL. This induced energy spread causes the beam to be difficult to control in a precise manner as the

previous chromatic dispersion problems are drastically worsened for the dipole magnet bending the beam towards the beam dump. The results from a GPT simulation of the electron beam after the undulator with the large induced energy spread can be seen in Figure 44.

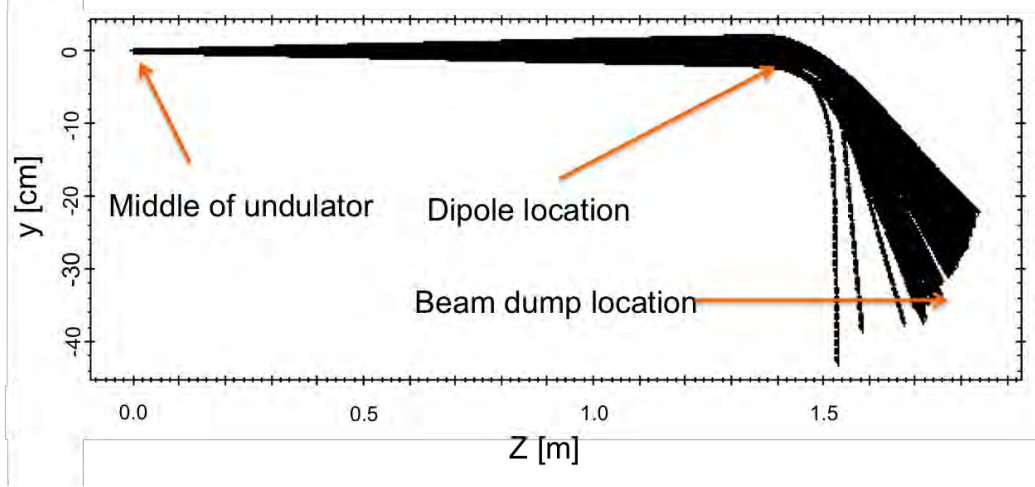


Figure 44. Trajectories of electrons from middle of undulator through last dipole.

The simulation shows the electron trajectories in the vertical plane as the electrons would be removed from the optical cavity. At this point the electron beam needs to be discarded into a beam dump. Combination magnets can be used to attempt to mitigate the dispersion but the simplest solution, and the one that is recommended for this case, is to place the beam dump as close as possible after the last dipole. If the beam dump is placed 20 cm after the last dipole the electrons beam transverse diameter will be only ~ 6 cm by ~ 1.6 cm, which is well inside the four inch diameter beam pipe that is being used already for the beam pipe. The beam spread can be useful to prevent damage to the beam dump from the focused high power of the beam.

a. GINGER Results

The electron beam parameters from the GPT simulations can be used as input into *GINGER* to estimate the performance of the FEL with the preceding beam line. This

involved calculating the electron beam's size and angular characteristics at the beginning of the undulator in GPT and transferring those parameters into *GINGER*. The emittance of a beam can be described by a relation with the emittance, $\varepsilon = \gamma_T x^2 + 2\alpha_T x x' + \beta_T x'^2$, where α_T , β_T , γ_T are the Twiss parameters [36]. With $\gamma_T = (1 + \alpha_T^2)/\beta_T$, the twiss parameters at the undulator entrance created by the beamline components from GPT are listed in Table 7.

$x(rms)$	$y(rms)$	α_{Tx}	α_{Ty}	β_{Tx}	β_{Ty}
0.81 mm	0.87 mm	1.27	1.5	0.26 m	0.47 m

Table 7. GPT derived Twiss parameters of electron beam at undulator entrance.

The simulation results of the electron beam and optical mode profiles that *GINGER* produces can be seen in Figure 45.

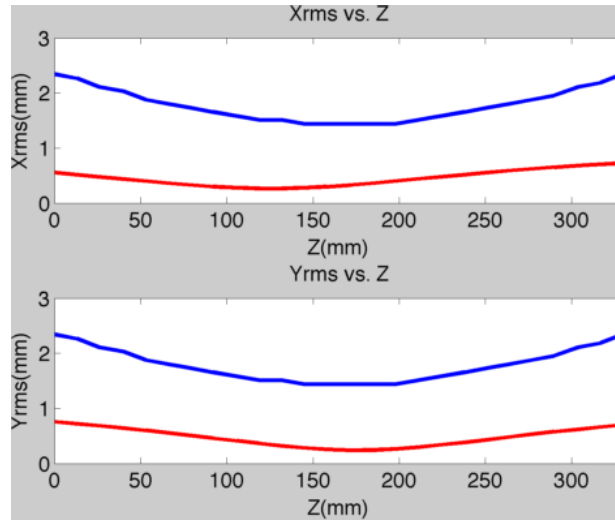


Figure 45. Electron beam (red) and optical mode (blue) transverse profiles for *GINGER* simulations using the electron beam parameters from GPT.

The non-symmetric nature of the electron beam (blue) focusing in both planes is shown but the beam is still well within the optical field (red). *GINGER* includes betatron focusing from the undulator, which decreases the electron beam waist size slightly [46].

This provides an rms waist size of ~ 0.24 mm and 0.27 mm in the x and y direction respectively. The resulting FEL performance can be seen in Figure 46.

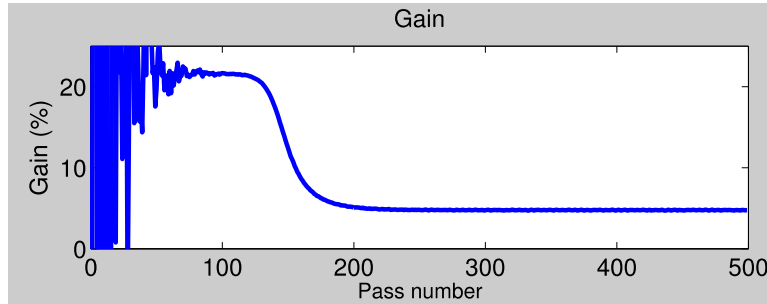


Figure 46. Ginger simulations for gain for the Niowave THz FEL using electron beam properties from GPT.

These electron beam focusing parameters closely match the nominal results shown in Figure 46 and supply a weak field gain of $\sim 22\%$ in approximately the same number of passes as the nominal case.

THIS PAGE INTENTIONALLY LEFT BLANK

V. HARDWARE DESIGN

A. LINAC COMPONENTS

Niowave Inc. has designed and built linacs for various U.S. Navy projects in the past. One project has incorporated a normal conducting copper cavity injector using a thermionic cathode and a superconducting spoke cavity for the accelerating structure, such as the one designed for the Niowave THz FEL, depicted in Figure 47.

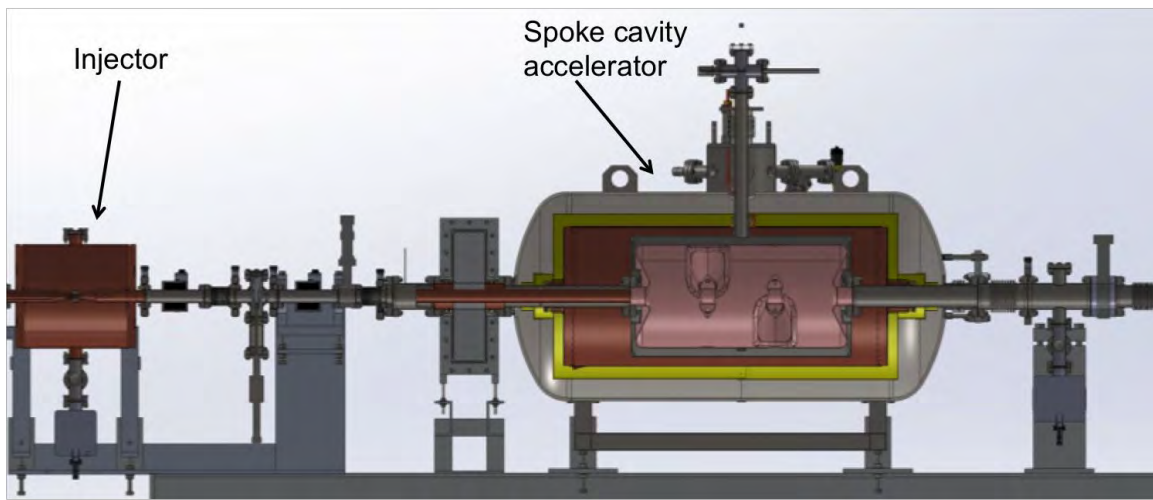


Figure 47. CAD drawing of linac for Niowave THz FEL.

The electron beam is generated in the copper injector (left) before entering the superconducting spoke cavity accelerator (middle). The cutaway shows the dewers that surround the cavity to hold the outer tank of liquid nitrogen and the inner tank of helium to maintain the proper temperature of the niobium. The electron beam exits to the right after being accelerated to the desired 8 MeV energy. It is after this point that the geometry and beamline components are designed in previous sections to transport the electron beam in a controlled way to the undulator.

B. TRANSPORT BEAMLINE COMPONENTS

The electron beam must be transported from the linac to the undulator under vacuum, bending around the cavity mirrors. The beam must also be focused into the undulator to properly overlap the optical pulse. A design of the transport beamline for the Niowave THz FEL can be seen in Figure 48.

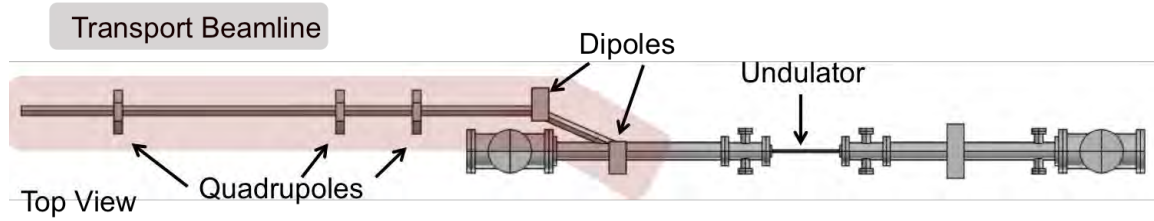


Figure 48. Niowave THz FEL transfer beamline highlighted in red.

The transport beamline consists of three quadrupoles that supply focusing and two combination dipole magnets to supply bending and additional focusing into the undulator.

1. Beam Pipes

The beam pipes that transport the electron beam from the linac to the optical cavity must be large enough to avoid losses of the beam current due to scraping, while not being unreasonably wide as to increase the cost of the beamline magnetic components. A larger beam pipe requires a stronger magnet due to the larger separation distances involved. As can be seen in Figure 41, the largest root-mean-square (rms) radius the electron bunch achieves in either transverse direction during the transport to the undulator is only ~ 7 mm. To allow for a margin of error, a beam pipe diameter of ~ 38 mm will be utilized so that the inside pipe wall is approximately five e-foldings away from the beam. It is estimated that only $\sim 0.1\%$ of the beam will be lost in this section of the beamline. The beam pipe will need to be custom made to supply the necessary $\sim 14^\circ$ bend while also connecting with the optical cavity beam pipe. An example of the type of custom beam pipe that will be necessary is shown in Figure 49.

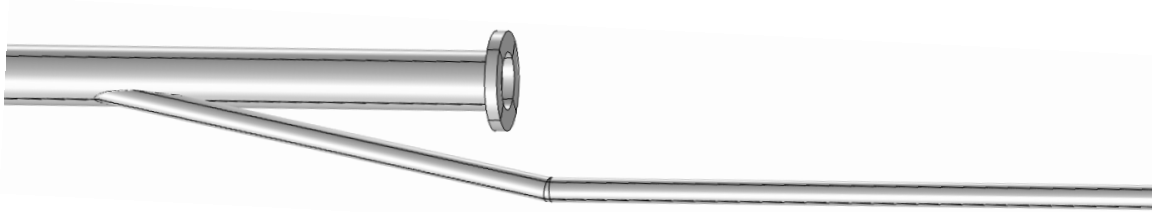


Figure 49. Diagram of necessary custom beam pipe with 14 degree bends.

The two bends along with the transition from the transfer beam pipe diameter to the optical cavity beam pipe diameter may need to be custom fabricated. The cost of beampipes is on the order of a few thousand dollars.

2. Quadrupoles

The quadrupoles were designed to supply the focusing in the y direction while aiding the dipoles in focusing in the x direction. The three quadrupoles were each assumed to be 3 cm long with peak magnetic field gradients of 1.68 T/m, -1.57 T/m, and 1.61 T/m respectively. For permanent magnet quadrupoles, a pole tip field of 1 T is achievable, which in conjunction with the 38mm diameter beam pipe can supply a magnetic field gradient that far exceeds what is needed. Permanent magnet quadrupoles can still have adjustable strengths depending on their design [47]. The total cost for the three quadrupoles with the properties listed in Table 6 would be ~\$40,000 [48]. This estimate includes the engineer design, the assembly, testing, and shipping.

3. Dipoles

The dipoles were designed to supply the transverse offset to the electron beam to allow it to be bent around the mirror housing and also to supply focusing to counteract the dispersion due to the energy spread. They were designed to have a nominal 20 cm arc length leading to a magnetic field strength of ~0.056 Tesla. For the first dipole, a rotation of each end face by 15° is needed to supply focusing. For the second dipole a rotation of each end face by -10° is needed to focus the electron beam into the undulator. The total

cost estimate for the two dipoles is ~\$40,000 with the engineer design, the assembly, testing, and shipping [48].

C. OPTICAL CAVITY BEAMLINE

The optical cavity beamline and adjacent vacuum components must accommodate not only the electron beam but also the optical mode. The design of this portion of the beamline is highlighted in Figure 50.

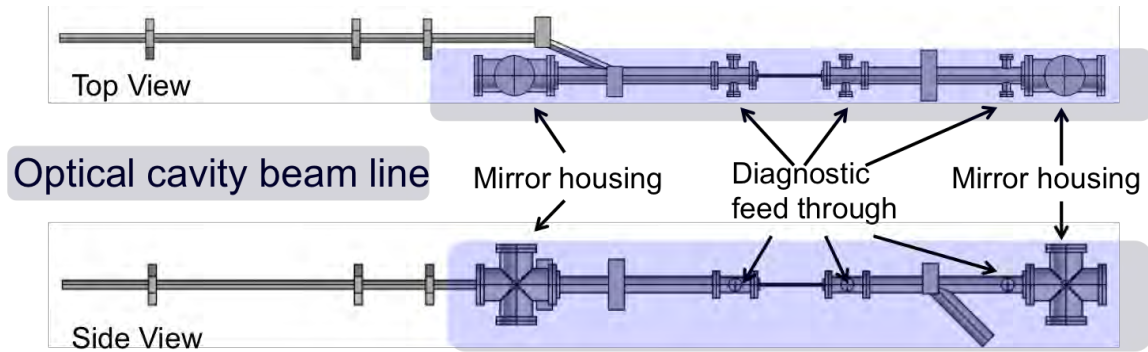


Figure 50. Optical cavity beamline highlighted in blue.

The optical cavity beamline has several main components. On the two ends of the cavity there are two large mirror-housing vessels that hold mirror mount assemblies. These assemblies control the longitudinal / transverse positions and the tip / tilt of the mirrors to allow for proper alignment. Directly on either side of the undulator and adjacent to the downstream mirror housing assembly are three crosses that allow for mechanical feedthroughs to aid in diagnostics and alignment. The length of the chamber must be such that the mirrors can have proper spacing to match the optical pulse bounce time to the electron pulse repetition frequency of 43.75 MHz as well as being wide enough to not cause clipping of the optical mode in the transverse direction.

1. Transverse Cavity Dimensions

The transverse size of the components will need to be studied to guarantee that the round trip losses stay below the weak field gain.

a. Mirror Size

The beam pipes surrounding the optical cavity and the mirrors that make up the resonator must be large enough to produce negligible clipping of the optical mode. The large diffraction angle that occurs due to the long wavelengths of this FEL design determines the mirror size suitable for the Niowave THz FEL. Table 8 shows the results of an analysis of the amount of clipping that different wavelengths will undergo.

Mirror Diameter	λ (μm)							
	126	114	104	90	80	73	69	66
12.7cm	~0.8%	~0%	~0%	~0%	~0%	~0%	~0%	~0%
10.2 cm	~5%	~2.5%	~1%	~0.2%	~0%	~0%	~0%	~0%
7.62 cm	~25%	~16%	~10%	~3.8%	~1.3%	~0.5%	~0.2	~0%

Table 8. Calculated round trip power loss due to clipping for each considered mirror size and wavelength.

The clipping was calculated for three different mirror sizes that were considered along with a range of wavelengths that fall into the Niowave THz FEL's tunable regime. For this analysis, an acceptable round trip loss due to clipping on the mirrors was assumed to be ~2%, as this would allow a margin for other areas of loss. The table entry is denoted green if the round trip loss with the specific wavelength and optic diameter is below that ~2% threshold and red if it is not. A 12.7 cm (five inch) diameter mirror allows tuning over the entire considered spectrum (~66 μm \rightarrow 126 μm) with less than two percent round trip losses from clipping on the mirrors. A 10.2 cm (4") diameter mirror size induces significant clipping of the longer wavelengths, therefore limiting the maximum wavelength to about 104 μm . A 7.62 cm (three inch) diameter mirror size reduces this the maximum wavelength even further to about 80 μm . While the 12.7 cm diameter option allows for a full tunable range of the FEL, the necessary optomechanical components are not as common and go up in price considerably. For this reason, as well as for space saving measures, a 10.2 cm diameter mirror size is recommended for the project.

b. Beam Pipe Sizes

The beam pipe diameter inside the undulator depends on the necessary gap to achieve a given wavelength; this analysis was discussed in Chapter III. A beam pipe with an outer diameter of ~16 mm and wall thickness of 1 mm allows for wavelengths ~100 μm and shorter. The beam pipe that encompasses the optical cavity between the undulator and the mirror housing must be wide enough to transmit the diffracting optical mode but should not be larger than the mirrors as that would not give any advantage. For this reason the beam pipe will be 10.2 cm in diameter, the same as the chosen mirror size.

2. Mirror Mount Assemblies

The mirrors will need to be properly aligned and adjusted to optimize the FEL performance.

a. Mirror Mount Housing Chamber

To hold the mirror mount setup on either side of the cavity, a large vacuum vessel is needed that supplies enough space for the mirror mount assembly, to allow a method for the light to escape, and to allow for electrical feedthroughs to control the actuators. To meet these criteria, a large 4-way cross will be utilized, as shown in Figure 51.

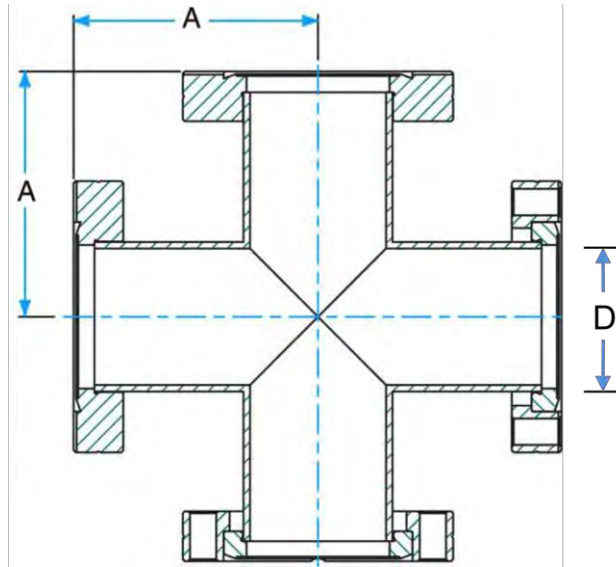


Figure 51. Mirror mount housing chamber, from [49].

The size chosen has a wall outer diameter of 8" and a centerline length (A in Figure 51) of 7.5". They meet the requirements in the following ways: they are relatively inexpensive, they have a flat mounting surface on the bottom for the mirror mount assembly, they can easily be attached to the cavity beam pipes with matching flange styles, they have an opening in-line with the cavity and the output coupler for a window to transmit the THz radiation, and they have an opening to allow the electrical feedthroughs for the actuator controls. Conflat style flanges that use two knife-edges and copper gaskets to provide great seals that can achieve ultra-high vacuum (UHV), typically greater than 10^{-9} Torr. The pricing information is listed in Table 9.

Product	Mirror housing chamber
Company	Kurt J. Lesker Company
Model	C-1000
Cost/unit	\$2050
Quantity	2
Total	\$4100

Table 9. Mirror housing chamber pricing information.

b. Mirrors

Due to the lack of easily available high reflective dielectric coatings for the THz regime, a metal mirror is recommended. The THz frequency reflects well off of metals with a reflectance up to ~99% (in power) for gold [50]. Because of this, a gold-coated mirror is recommended with the substrate made out of a cheaper material such as aluminum. The final design will be a ~5 cm radius (four inch diameter) gold coated concave mirror with a radius of curvature of ~1.72 m. The middle of one of the mirrors will have a 1 mm diameter hole for output coupling. The mirror pricing information is listed in Table 10.

Product	Gold Plated Mirror
Company	Laser Beam Products
Model	Custom 4" diameter mirror, 0.5mm radius hole
Cost/unit	\$680
Quantity	2 (one without hole)
Total	\$1360

Table 10. Gold mirror pricing information.

c. Mirror Mount Assembly

To support the mirror and supply the necessary angular and translational adjustments the 4" optic must be held in an optic mount assembly. This will consist of a mirror mount to control the angular alignment and a translation stage to supply transverse, longitudinal, and vertical position adjustments. The components chosen must be vacuum compatible to avoid excessive outgassing and ensure that the vacuum requirements are met for the whole system ($\sim 10^{-9}$ Torr). The stage must be large enough to supply the necessary length of movement while not being too large to unnecessarily increase the size of the vacuum chamber. To control the mirror mount and translation stage under vacuum, motorized actuators are used. Twelve actuators will be needed (three per mirror mount and three per translation stage). Controllers will be used to translate the

orders from the computer software to the proper voltages to move the piezomotor actuators. The parts price information is listed in Tables 11–14.

Product	Vacuum rated 4" mirror mount
Company	Newport Corporation
Model	Custom version: U400-AC3K
Cost/unit	\$2500–\$3000
Quantity	2
Total	\$5000–\$6000

Table 11. Mirror mount pricing information.

Product	Vacuum rated translation stage (12.7 mm travel)
Company	Newport Corporation
Model	9066-XYZ-L-V
Cost/unit	\$1976
Quantity	2
Total	\$3952

Table 12. Translation stage pricing information.

Product	Vacuum rated piezomotor actuator (12.7 mm travel)
Company	Newport Corporation
Model	8301-UHV-Kap
Cost/unit	\$1185
Quantity	12
Total	\$14220

Table 13. Piezomotor actuator pricing information.

Product	Picomotor actuator controller
Company	Newport Corporation
Model	8742-12-kit
Cost/unit	\$2940
Quantity	1
Total	\$2940

Table 14. Picomotor actuator controller pricing information.

d. Output Window

The output window material must transmit the THz radiation with minimum absorption and be mounted on a flange to be vacuum compatible. A crystalline quartz window will be utilized as it has minimum absorption in the THz spectrum and is also transparent to visible radiation, which will aid in alignment. A transmission spectrum of crystalline quartz can be seen in Figure 52.

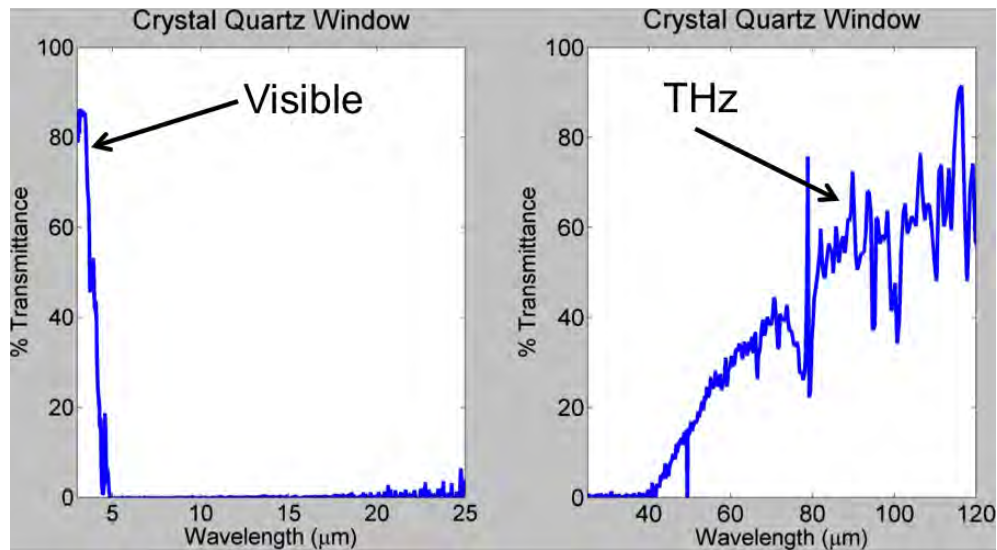


Figure 52. Measured transmittance spectrum for crystal quartz window, from [51].

This has a transmittance range of ~35% to 50% in the wavelength range that the Niowave THz FEL will be operating. The noise in at longer wavelengths measurement is due to the limitations of the spectrometer being utilized. A one inch diameter window mounted on a conflat flange will be used. The pricing information of the window is listed in Table 15.

Product	Crystalline quartz output window
Company	MPF
Model	A4977-1-CF
Cost/unit	\$2350
Quantity	1
Total	\$2350

Table 15. Crystalline quartz window pricing information.

A scale depiction of the final design for the mirror housing can be seen in Figure 53.

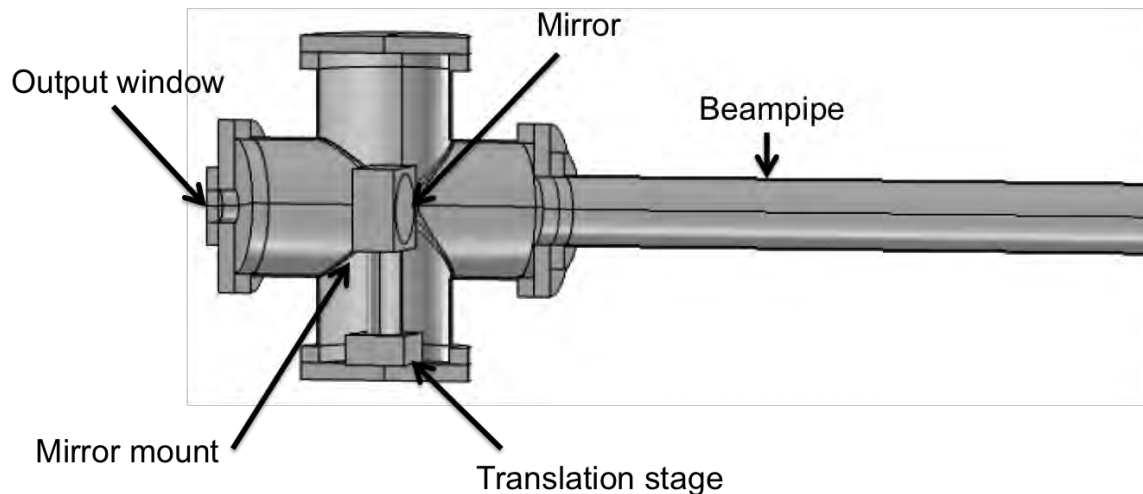


Figure 53. Final design for mirror housing and control assembly.

Each element in the mock-up is of the correct dimensions as the component that will be used. This shows that the 8" diameter mirror-housing chamber is large enough for the transverse footprint of the translation stage. In Figure 53, the optical field will enter the

chamber from the right before reflecting off of the mirror. Not visible is the output coupling hole, which will allow the radiation to transfer through and exit the output window behind.

e. Miscellaneous

To transport the electrical signal from the actuator controllers to the actuators, a vacuum electrical feedthrough is needed. A 15-pin feedthrough will be used because each mirror mount assembly will need 12 pins (2 per actuator) to control the necessary voltages. Such a flange and its necessary connector are seen in Figure 54.



Figure 54. Example of conflat flange mounted electrical feed through (left) and necessary connection (right), from [52] and [53].

These will allow the movement of the actuators to control the mirror alignment. The pricing information for these parts is listed in Tables 16–17.

Product	Electrical feedthrough
Company	MDC
Model	9132017
Cost/unit	\$376
Quantity	2
Total	\$752

Table 16. Electrical feedthrough pricing information.

Product	Electrical feedthrough connection
Company	MDC
Model	9924069
Cost/unit	\$172
Quantity	2
Total	\$344

Table 17. Electrical feed-through connection pricing information.

To aid in the alignment of the optical cavity three diagnostic ports will be placed in the optical cavity beamline. They will allow for three actuators to be able to intercept the cavity. The actuators will need precise control as they must be able to align targets on the $\sim 100\ \mu\text{m}$ scale with the cavity axis. The option suggested for the linear actuator is listed in Table 18.

Product	Mechanical linear feed through
Company	MDC
Model	60004-01
Cost/unit	\$1252
Quantity	3
Total	\$3756

Table 18. Mechanical linear feedthrough pricing information.

D. EXIT BEAMLIN

After the FEL interaction in the undulator, the electron beam with its induced energy spread needs to be successfully guided into the beam dump. One exit beamline geometry is highlighted in green in Figure 55.

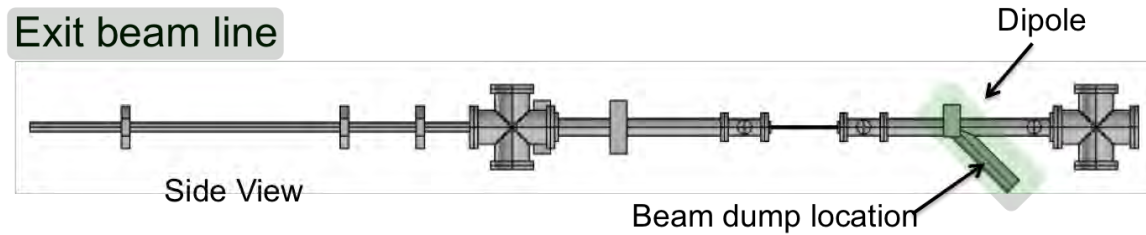


Figure 55. The exit beamline highlighted in green

As was stated earlier, the FEL interaction causes a large energy spread in the electron beam due to the relatively high extraction of energy. This $\sim 20\%$ energy spread causes a large dispersion after the dipole. Using a combination magnet as before but with more extreme edge focusing (larger canting of the end faces) will be used in an attempt to counteract the large dispersion in angles, but it is not very effective given the magnitude of the energy spread. Therefore, the suggested solution is to place the beam dump as close as possible to the last dipole (~ 20 cm), which will keep the beam pipe and beam dump a reasonable size. For this final 45° bend a 20 cm long dipole with no edge focusing a magnetic field of ~ 0.1 Tesla is needed. This will cost on the order of the other dipoles that were quoted at $\sim \$20,000$ [48].

E. ALIGNMENT TECHNIQUES

The alignment of the cavity mirrors, electron beam, and undulator axis must be sufficient enough to get some signal from the FEL. After an initial signal is seen, parameters can be further adjusted to maximize the signal.

1. Transverse and Angular Mirror Alignment

The alignment system consists of two targets on actuators that can be placed into the beam path, two alignment lasers with beam expanders and focusing optics, a pop-in mirror on an actuator to be placed in the beam path, a pop-in mirror outside the cavity in line with the output coupler, and several cameras to view the alignment procedure. The targets consist of triangular wedges with a 1 mm diameter hole drilled through each of them. A schematic of the system is seen in Figure 56.

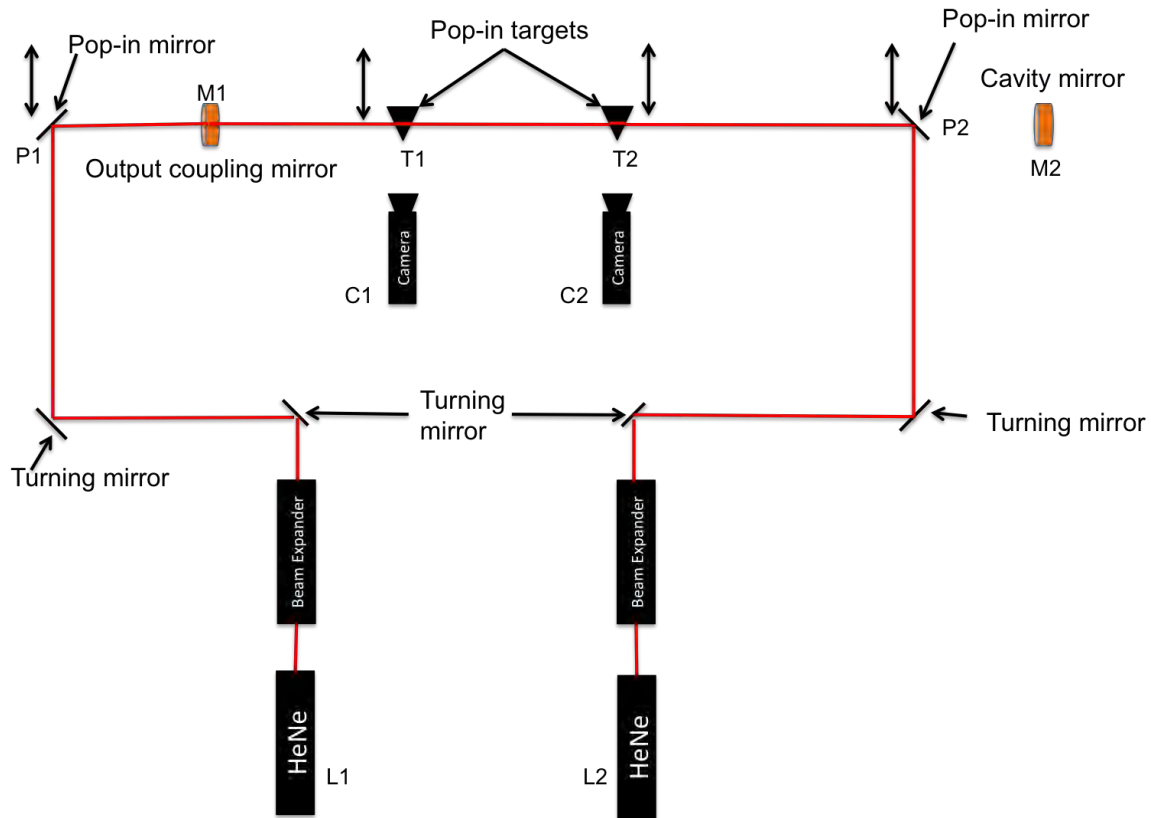


Figure 56. Schematic of optical cavity alignment system for Niowave THz FEL

First, prior to installing the M1 mirror, the undulator axis and the targets are aligned using by the undulator manufacturer, who have mapped its magnetic field. Once the undulator axis and the alignment wedges are properly aligned, they can be used as targets for alignment of the cavity mirrors. The holes allow for an alignment laser to propagate through the targets while the angled sides allow the use of digital cameras to view any misalignments. The beam expander and focusing optics allow for the focus of the alignment laser to be shifted, aiding in alignment. The steps are as follows.

1. Ensure that both the upstream and downstream alignment lasers (L1 and L2) are collinear down the magnetic axis (aligned with the targets T1 and T2) by adjusting the turning mirrors.
2. Install the output coupler mirror (M1 in Figure 56) and align the hole with laser beam.
3. Removing P2, visually align the center of M2 along L1.

4. Put in P2, check alignment of L2 with cavity axis and then remove T1.
5. Using L2, view the reflection from M1 onto T2 and align the center of the reflection on the hole.
6. Remove P2, insert T1, and check alignment of L1 with cavity axis. Remove T2 and P2.
7. Using L1 view the reflection from M2 onto T1 and align the center of the reflection on the hole.

The transverse shift alignment of M2 (step 3) is less stringent than other tolerances as the mirrors' spherical curvature allow for any small transverse misalignments to be corrected with a tilt, which is done in step 7. With this technique, one can achieve alignment to within ~ 0.1 mm of the cavity axis on the target [54]. This leads to a cavity alignment tolerance of ~ 0.1 mrad, which is just inside the necessary ~ 0.15 mrad tolerance and will allow fine-tuning adjustments by maximizing the signal of the FEL while operating. The designed optical cavity beamline has three different diagnostic locations where the two targets and the pop in mirror can be placed.

2. Longitudinal Alignment

The FEL cavity must have the correct length and desynchronism on the order of the slippage length (~ 1 mm) in order for lasing to occur. This is fairly lenient compared to other shorter wavelength FEL oscillators. In practice the oscillator cavity length is adjusted close to the desired length using simple measuring techniques before the cavity length is scanned, searching for lasing operation. This is the method that will be attempted for this FEL as adding other laser range finding or survey methods would add unnecessary complexity. [55].

F. FINAL DESIGN IN 3D

This design of the optical cavity beamline and mirror housing units (see Figure 57) meet the requirements that were necessary for the FEL to operate.

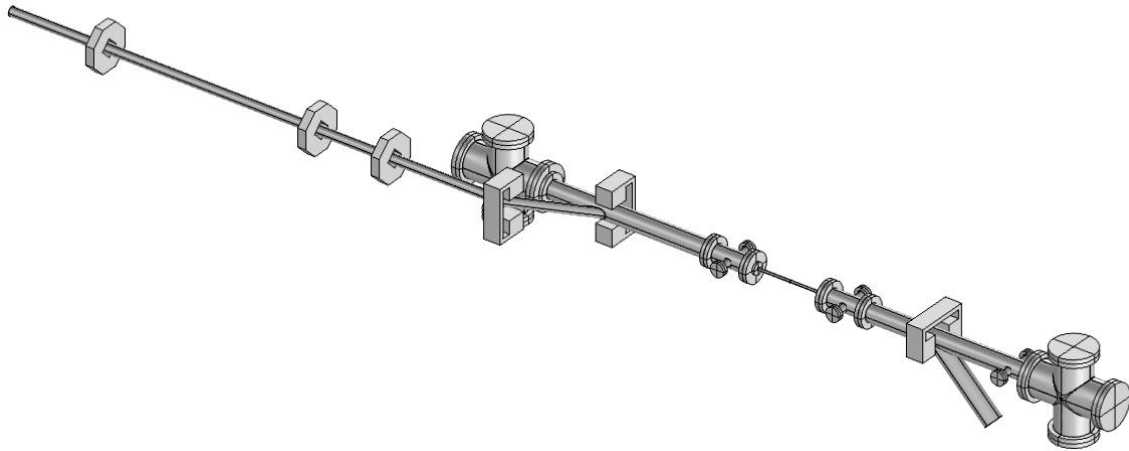


Figure 57. Final design of optical cavity beam vacuum structures

It include a low-loss optical cavity, the required components for initial cavity alignment, and the beam line components to couple the electron beam into the cavity as well as ejecting it into the beam dump.

THIS PAGE INTENTIONALLY LEFT BLANK

VI. CONCLUSION

Free electron lasers are sources of coherent radiation that can be designed and tuned across the electromagnetic spectrum. This ability allows them to operate in portions of the spectrum where there are no coherent, powerful kW-level sources, for example in the THz regime. Due to the nature of the FEL lasing medium (relativistic electrons) it can be scaled to high power. These attributes allow THz FELs to meet a wide range of applications including spectroscopy, pump-probe experiments, and screening for security purposes. THz FELs have been created in the past but are generally large sized, expensive facilities. With the use of a compact linac, a short undulator, and an optical cavity, a relatively inexpensive, kW-level, tunable, THz source can be created. This dissertation presents and studies the design of such a THz FEL.

The FEL was simulated using three different codes to show the effects of various design parameters. These simulations show that an electron beam with an emittance of 28mm-mrad and energy spread of $\Delta\gamma/\gamma \approx 1.7\%$ can be used to create an FEL with moderate weak field gain and high extraction. The optical cavity was designed to operate over the portion of the spectrum from $\sim 60 \mu\text{m} \rightarrow 126 \mu\text{m}$ wavelength.

The electron beam with realistic energy spread and emittance must be transported from the linac into the undulator and must properly align within the optical mode. To control and focus the electrons, a beamline was designed utilizing quadrupoles and combination dipole magnets. The combination dipole magnets with large amounts of edge focusing were designed to overcome the dispersion caused by the electron beam energy spread and to focus the electron beam into the undulator. Ultimately, the beamline components were found to meet the initial nominal requirements of ~ 0.45 mm radius in the center of the undulator set out during the FEL design and simulations.

The hardware for the Niowave THz FEL was designed to control the oscillator cavity mirrors and the electron beam. The optical cavity beamline components allow for the mirror mount assemblies to control the mirrors' angular, transverse, and longitudinal adjustments. Alignment techniques were described, utilizing three different diagnostic

feedthroughs to allow alignment targets as well as pop-in mirrors. Finally, the exit beam line was designed with a short transit into a beam dump to handle the $\sim 20\%$ induced energy spread generated by the high extraction FEL.

While this dissertation covers a large portion of the major design criteria for the FEL, several additional things can also be considered going forward. Fringe field effects must be incorporated into the design of the magnetic field strengths of the dipoles and quadrupoles. To counteract pulse elongation that occurs during the dipole offset, the initial pulse length and the energy spread may need to be decreased by a factor of three or other bunching mechanisms included into the beamline to obtain the ~ 5 ps bunch length at the undulator required by the FEL. Engineering concerns, such as the necessary shielding around the beam dump to ensure protection of the surrounding equipment, will need to be assessed and designed. In terms of the applications for this FEL, the expected spectrum should be adjusted to meet the requirements set out by the application.

This design produces an ~ 2 kW-level, compact, THz FEL for a wide range of applications. The compact size and relatively inexpensive components open up the use of THz radiation to many new users.

LIST OF REFERENCES

- [1] S. Gharavi, H. Babak. *Ultra High-speed CMOS Circuits beyond 100 GHz*. New York, NY: Springer, 2012.
- [2] P. H. Siegel. "Terahertz technology," in *IEEE Transactions on Microwave Theory and Techniques*, vol. 50, no. 3, pp. 910–928, Mar. 2002.
- [3] A. S. Fisher et al. (n.d.). THz pump and x-ray probe development at LCLS. [Online] Available: <http://slac.stanford.edu/pubs/slacpubs/14500/slac-pub-14545.pdf>. Accessed Nov. 22, 2014.
- [4] M. Hoffmann et al., "THz-pump/THz-probe spectroscopy of semiconductors at high field strengths," *J. of Opt. Soc. of Amer. B*, vol. 26, issue 9, pp. A29–A34, Jun. 2009.
- [5] J. F. Federici et al., "THz imaging and sensing for security applications—explosives, weapons and drugs," *Semiconductor Sci. and Technol.*, vol. 20, no. 7, pp. S266–S280, Jun. 2005.
- [6] T. Löffler et al. "Visualization and classification in biomedical terahertz pulsed imaging," *Physics in Medicine and Biology*, vol. 47, no. 21, pp. 3847–3852, Oct. 2002.
- [7] D. Woolard. Terahertz electronic research for defense: novel technology and science. [Online]. Available: <http://www.nrao.edu/meetings/isstt/papers/2000/2000022038.pdf>. Accessed Nov. 20, 2014.
- [8] M. C. Kemp et al., "Security applications of terahertz technology," in *Proc. of SPIE 5070, Terahertz for Military and Security Applications*, pp. 44–52, Aug. 2003.
- [9] F. C. Cruz et al., "Continuous and pulsed THz generation with molecular gas lasers and photoconductive antennas gated by femtosecond pulses," *SBMO/IEEE MTT-S International Microwave & Optoelectronics Conference*, 2007, pp. 446–449.
- [10] B. S. Williams, "Terahertz quantum-cascade lasers," *Nature Photonics*, vol. 1, pp. 517–525, Sep. 2007.
- [11] S. Verghese et al., "Highly tunable fiber coupled photomixers with coherent terahertz output power," *IEEE Transactions on Microwave Theory and Techniques*, vol. 45, no. 8, pp. 1301–1309, Aug. 1997.

- [12] A. Staprans et al., “High-power linear beam tubes,” in *Proc. of the IEEE*, vol. 62, no. 3, pp. 299–330, Mar. 1973.
- [13] H. Jory et al., “Design and operation of 140 GHz gyrotron oscillators for power levels up to 1 MW CW,” *Int. Nucl. Inform. Syst.*, vol. 18, no. 21, Dec. 1986.
- [14] B. A. Knyazev et al., “Novosibirsk terahertz free electron laser: facility development and new experimental results at the user stations,” in *Proc. of Int. Conf. on Infrared, Millimeter and Terahertz Waves*, 2011, pp. 1–2.
- [15] Y. U. Jeong et al., “A compact THz free electron laser at KAERI,” in *Proc. of 14th Int. Conf. on Terahertz Electronics*. 2006, p. 551.
- [16] FELIX specifications. (n.d.). Dutch Institute for Fundamental Energy Research. [Online]. Available: <http://www.differ.nl/research/guthz/felix/specifications>. Accessed Dec. 1, 2014.
- [17] R. Kato et al., “High power terahertz FEL at ISIR, Osaka University,” in *Proc. of Int. Particle Accelerator Conference*, 2010, pp. 2209–2211.
- [18] The main parameters of FELBE, the free-electron laser of the radiation source ELBE. (n.d.). [Online]. Available: <https://www.hzdr.de/db/Cms?pNid=205>. Accessed Dec. 1, 2014.
- [19] Centre Laser Infrarouge d’Orsay: the laser: Main specs. (n.d.). [Online]. Available: http://clio.lcp.u-psud.fr/clio_eng/laser.html. Accessed Dec. 1, 2014.
- [20] W. J. van der Zande et al., “Design of a long wavelength FEL for experiments under high magnetic fields,” in *Proc. of the Free Electron Laser Conference*, 2006, pp. 485–487.
- [21] D. H. Levy et al., eds. *Free Electron Lasers and Other Advanced Sources of Light: Scientific Research Opportunities*. Washington, DC: National Academies Press, 1994, pp. 24–32.
- [22] A. M. Todd et al., “Megawatt-class free electron laser concept for shipboard self-defense,” *Proc. SPIE 2988 Free-Electron Laser Challenges*, 1997, pp. 176–184.
- [23] A. Laney, “The effects of accelerator frequency and electron beam focusing in free electron lasers,” M.S. thesis, Dept. of Physics, Naval Postgraduate School, Monterey, CA, 2012.
- [24] H. P. Bluem et al., “High brightness thermionic electron gun performance,” in *Proc. of ICFA Advanced Beam Dynamics Workshop on Energy Recovery Linacs*, 2011, pp. 30–35.

- [25] Elliptical $\beta=1$ cavities. (2013, Dec. 20). Institute of research into the fundamental laws of the universe. [Online]. Available: http://irfu.cea.fr/en/Phocea/Vie_des_labos/Ast/ast_visu.php?id_ast=2981. Accessed Nov. 22, 2014.
- [26] M. Kelly, “Superconducting spoke cavities,” in *Proc. of ICFA Advanced Beam Dynamics Workshop*, 2006, pp. 337–340.
- [27] J. R. Delayen, “Superconducting spoke cavities for electrons and high velocity proton linacs,” in *Proc. of the Linear Accelerator Conference*, 2012, pp. 758–762.
- [28] T. Grimm. (Sep. 2010). Development of superconducting RF multi-spoke cavities for electron linacs. [Online]. Available: http://science.energy.gov/~media/np/pdf/sbir%20sttr/presentations/grimm_niowa_ve_500_mhz_e_spoke_100909.pdf.
- [29] Illustration of FEL oscillation. (n.d.). Infrared free electron laser research center. [Online]. Available: http://www.rs.noda.tus.ac.jp/fel-tus/English/E-About_FEL.html. Accessed Nov. 22 2014.
- [30] W. B. Colson et al., *Free Electron Laser Handbook*, North-Holland Publishing Company, Amsterdam, Netherlands, 1990.
- [31] “Free electron lasers,” class notes for Free Electron Laser Physics, Dept. of Physics, Naval Postgraduate School, Monterey, CA, winter 2010.
- [32] S. H. Gold et al., “Development of a high average current RF linac thermionic injector,” *Phys. Rev. Special Topics—Accelerators and Beams*, vol. 16, 2013.
- [33] W. B. Colson, “Free electron laser theory,” Ph.D. dissertation, Dept. of Physics, Stanford University, Palo Alto, CA, 1977.
- [34] W. M. Fawley. (n.d.). A user manual for GINGER-H and its post-processor XPLOTGINH. [Online]. Available: <http://www-ssrl.slac.stanford.edu/lcls/technotes/lcls-tn-04-3.pdf>. Accessed: Nov. 3, 2014.
- [35] W. B. Colson, “Weekly report: 2013-07-19 closing the gap,” unpublished.
- [36] H. Braun. (2008, Feb 6). Emittance diagnostics. [Online]. Available: <http://cas.web.cern.ch/cas/France-2008/Lectures/Braun-Emittance.pdf>.
- [37] “Electric ship weapons systems,” class notes for Electric Ship Weapon Systems, Physics Dept., Naval Postgraduate School, Monterey, CA, spring quarter 2011.
- [38] Accelerator details: How synchrotrons work. (n.d.). [Online]. Available: http://nagysandor.eu/AsimovTeka/tevatron_hu/synchrotrons.html. Accessed Nov. 22, 2014.

- [39] K. Wille, *The Physics of Particle Accelerators—An Introduction*, New York, Oxford University Press, 2000.
- [40] J. Tanabe. (2005, Jan. 6). Iron dominated electromagnets design, fabrication, assembly and measurement. [Online]. Available: <http://www.slac.stanford.edu/cgi-wrap/getdoc/slac-r-754.pdf>.
- [41] S. Russenschuck. (n.d.). Design of accelerator magnets. [Online]. Available: <https://cas.web.cern.ch/cas/Loutraki-Proc/PDF-files/D-Russenschuck/CAS-Russenschuck.pdf>. Accessed Nov. 22, 2014.
- [42] N. T. Shen, “Evolution of the electron beam envelope in a free electron laser beamline,” M.S. thesis, Dept. of Physics, Naval Postgraduate School, Monterey, CA, 2013.
- [43] J. Holmes et al. (2009, Jan 1). Magnetic Fields and Magnet Design. [Online]. Available: <http://uspas.fnal.gov/materials/09VU/Lecture2.pdf>.
- [44] S. B. Van der Geer, M.J de Loos, “General particle tracer user manual version 3.03,” unpublished.
- [45] S. Gottschalk, private communication, Jul. 2014.
- [46] V. Gupta et al., “Three frequency undulator radiation in presence of betatron oscillation,” *Romanian J. of Physics*, vol. 57, no. 7–8, pp. 1138–1147.
- [47] S. C. Gottschalk et al., “Permanent magnet systems for free-electron lasers,” *Nuclear Instruments and Methods in Physics Research A*, vol. 507, pp. 181–185, Jul. 2003.
- [48] S. Gottschalk, private communication, Nov. 2014.
- [49] 4-way standard cross. (n.d.). Kurt J. Lesker Company. [Online]. Available: http://www.lesker.com/newweb/flanges/fittings_cf_crosses.cfm?pgid=4waystd. Accessed Nov. 22, 2014.
- [50] G. Sunderland, private communication, May 2014.
- [51] C. M. Pogue, “Super-radiant free electron laser measurement and detection,” M.S. thesis, Physics Dept., Naval Postgraduate School, Monterey, CA, 2013.
- [52] Electrical feed throughs multi pin feed throughs—Type-d subminiature. (n.d.). MDC. [Online]. Available: <http://www.mdcvacuum.com/DisplayProductContent.aspx?d=MDC&p=i.1.5.1.1>. Accessed Nov. 22, 2014.

- [53] 9924048–D-Conn with sockets 25 39. (n.d.). MDC. [Online]. Available: <http://www.mdcvacuum.com/DisplayPart.aspx?d=MDC&p=9924048>. Accessed Nov. 22, 2014.
- [54] D. Oepts. (May 2000). Optical cavity alignment for the ELBE FEL with DESY undulators. [Online]. Available: <http://www.hzdr.de/FWK/MITARB/fwkf/oepts/cav2.html>
- [55] C. J. Curtis. (n.d.). The measurement of the optical cavity length for the infrared free electron laser. [Online]. Available: <http://www.jlab.org/eng/survalign/documents/publ/Ccurt99.pdf>. Accessed Nov. 22, 2014.

THIS PAGE INTENTIONALLY LEFT BLANK

INITIAL DISTRIBUTION LIST

1. Defense Technical Information Center
Ft. Belvoir, Virginia
2. Dudley Knox Library
Naval Postgraduate School
Monterey, California